A multimodal investigation of retrosplenial function

Michal Milczarek

**School of Psychology
School of Biosciences**

**A dissertation submitted as partial fulfilment of the requirements for the award of a doctoral degree in Integrative Neuroscience
September 2017**

Acknowledgements

I would like to first and foremost thank my partner, Jamie, for putting up with me during the PhD process. His wit, positive attitude and continuous encouragement were as much a part of this work as my own contributions.

Next, I would like to thank my family who have been incredibly supportive, including ensuring I had delicious food and blossoming flowers in my garden. Thank you, mum!

This journey also would not have been possible without the troupe of my dear friends, Liad, Tom and Matthieu, with whom I celebrated and commiserated the high and low points of the last four years.

I would also like to thank the members of the BNL and Sengpiel laboratories. Heather and Moira for expert technical advice and sharing the burden of many hours spent in behaviour and histochemistry, James for his companionship and crucial help with surgery and Lisa for putting up with me as her nagging office mate. I am also grateful to Asta for easing me into the intricacies of imaging and for her resourcefulness.

Last but not least, I am grateful to both of my wonderful supervisors, Seralynne and Frank, for believing in me, offering great advice and sometimes putting breaks on the not-so good ideas I had aplenty. I could not have hoped for better mentorship!

Table of contents

Table of figures

Summary

The retrosplenial cortex (RSC) has attracted much attention due to its proposed role in learning and memory. It forms a part of the Papez circuit and is connected with the anterior thalamic nuclei, the hippocampal formation and sensory areas including the visual cortex. Damage to the RSC impairs episodic and spatial memory. Furthermore, dementias such as Alzheimer's Disease have been shown to involve retrosplenial pathology, highlighting the need to better understand the role of this region. The current work explores the contributions of the RSC to visual and spatial processing as well as its vulnerability in a model of amnesia. It is demonstrated here that visual stimulation of anaesthetised mice elicits intrinsic signal responses in the RSC, similar to those seen in the primary visual cortex. Further, it is shown that training on a spatial memory task is paralleled by the gradual formation of a context-specific retrosplenial memory engram, which re-activates upon re-exposure to the task weeks from initial acquisition. Moreover, the overall level of retrosplenial activity and the stability of the engram show a link to the successful expression of spatial memory upon re-exposure to the task. Finally, it is revealed that the disconnection of the mammillary bodies from the anterior thalamus, which is a common feature of diencephalic amnesia, leads to the reduction of the metabolic marker, cytochrome oxidase, in the RSC as well as to widespread microstructural changes revealed by diffusion tensor imaging. Taken together, it is demonstrated here that the RSC is an important integratory hub contributing to the formation of episodic memory and aspects of visual processing and that it displays high sensitivity to the loss of its inputs, which may explain its involvement in a variety of conditions.

1 General Introduction

Foreword

One of the greatest feats of the human mind is its ability to generate a cohesive and fluid representation of the internal and external world. We see not random speckles of colour or a mishmash of jumbled lines but a landscape filled with features and objects, each in relation to another and the observer himself. Similarly, our perception of time is not fragmentary but continuous yet divisible into events and stored as distinct memories. Just how the brain manages to create such a perfect illusion of orderliness out of the seemingly agnostic sensory experience is at the heart of cognitive sciences. Among them, neuroscience seeks a mechanistic explanation. One of its greatest triumphs must be the discovery of place cells by John O'Keefe, which demonstrated, for the first time, the link between the environment and its internal representation. Soon followed many other discoveries strengthening the notion of the brain as a specialised machine dedicated to modelling reality. It is not, however, individual neurons, but the collective effort of multiple hierarchically-organised neuronal networks that can generate such comprehensive representations. And crucially, information arising from the senses undergoes integration and binding within multiple neuronal networks and brain regions. One such region is the retrosplenial cortex.

1.1.1   Why study the retrosplenial cortex?

The past few decades have seen increasing interest in retrosplenial research among the neuroscience community resulting in over 15,000 publications now featured on Google Scholar. Its gradual rise to fame, supported by numerous neuroimaging studies in humans, has firmly placed the retrosplenial cortex in the pantheon of memory-related areas, despite the initial proposal of its involvement in the processing of emotion by Papez (1937). Many other roles have since been ascribed to the retrosplenial cortex (see Figure 1.1.1) consistent with its rich connectivity to a number of other brain sites. Yet, despite many advances, the function of the retrosplenial cortex is still shrouded in mystery. One of the limitations of studies in human subjects is (fortunately!) the scarcity of patients displaying focal damage to the structure. On the other hand, experiments in

animals have provided valuable insights into retrosplenial function by enabling the placement of discrete lesions as well as allowing for direct recording from the retrosplenial cortex. Work presented in this thesis utilises a range of investigative techniques employed in the study of mouse and rat retrosplenial function in health and disease. But before these are reported, it is necessary to first consider the current state of knowledge about the retrosplenial cortex.

Figure 1.1.1. Terms associated with the 'retrosplenial' search term in the PubMed database. The word cloud displays words most commonly appearing in the context of the retrosplenial cortex (with terms such as 'brain' and 'cortex' removed). It is evident that a staggering proportion of studies have been conducted in the rat. The link with memory and hippocampus is also evident.

1.1.2 The anatomy of the retrosplenial cortex

The human retrosplenial cortex encompasses Brodmann areas 26, 29 and 30 and lies within the posterior cingulate gyrus, caudally to the splenium of the corpus callosum. The retrosplenial cortex borders the subiculum and isocortical areas, including area 23. In the macaque brain, the retrosplenial cortex is wrapped around the caudal and posteroventral surfaces of the corpus callosum, while in the rat and mouse brain, it is located dorsally and occupies nearly half

of the length of the medial aspect of the cerebrum (Kobayashi & Amaral, 2000)(Figure 1.1.2, Figure 1.1.3). The retrosplenial cortex differs from the surrounding cortex based on its distinct lamination pattern. The innermost subdivision of the retrosplenial cortex, corresponding to areas 26 and 29 in the human brain, is relatively thin and displays only four distinguishable layers with characteristic round, densely-packed cells in the outermost external granular layer. In contrast to the adjacent area 30, it does, however, contain an internal granular cell layer and is therefore referred to as 'granular' retrosplenial cortex while 'agranular' or 'dysgranular' retrosplenial cortex is the term used to describe area 30. The dysgranular retrosplenial cortex is also a poorly-laminated region, clearly less well-developed than the bordering isocortical area 23 (corresponding to the posterior parietal cortex region). In the rodent brain, the retrosplenial cortex has likewise been divided into the granular and dysgranular regions. The granular retrosplenial cortex in mouse and rat is often subdivided into further two-to-three regions: granular a, b (and c), each showing distinct Nissl staining patterns and, importantly, different connectivity (Vogt, 1985; Vogt, et al. 1995; Vogt & Paxinos, 2014) (Figure 1.1.3**,** Figure 1.1.4).

■ dysgranular retrosplenial cortex (BA30)

■ granular retrosplenial cortex (BA26,29)
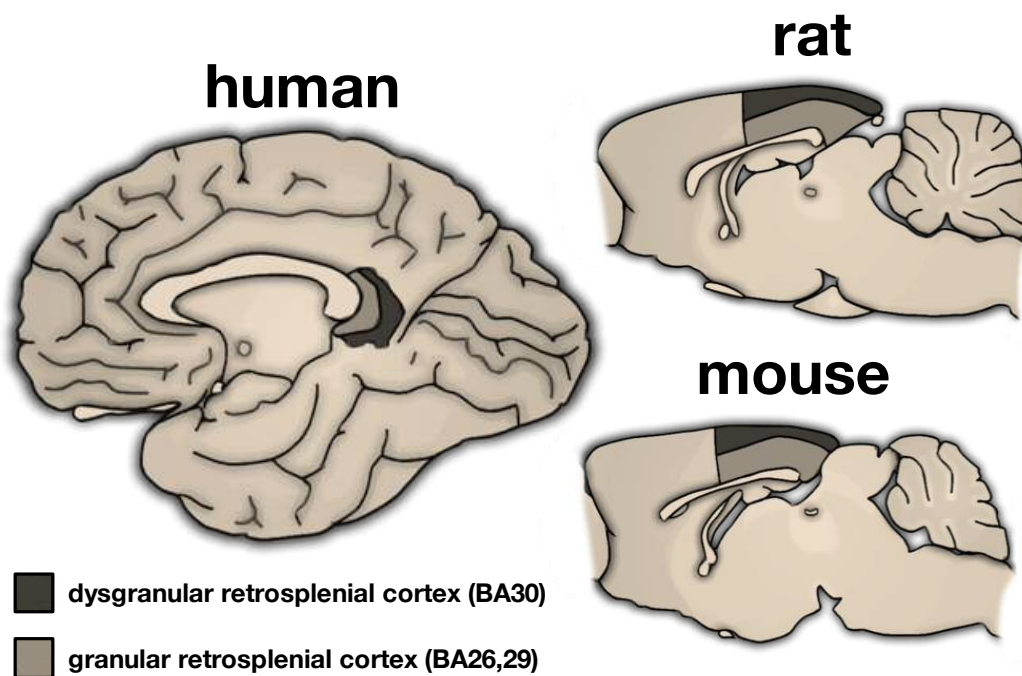
Figure 1.1.2. The location of the retrosplenial cortex in the human and rodent brains. The diagrams display sagittal sections revealing the position of the two main subdivisions of the retrosplenial cortex. Images are not so scale.

1.1.3 The connectivity of the retrosplenial cortex

The retrosplenial cortex is a heavily interconnected brain region and is thought to integrate converging inputs from multiple functional networks. Studies in the macaque identified the presence of strong reciprocal connections between the retrosplenial cortex and many sites vital for memory, such as the hippocampal formation (most notably the subicular cortex), parahippocampal areas (entorhinal cortex and areas TH and TF) and certain thalamic nuclei (anterior and laterodorsal) (Insausti, Amaral & Cowan, 1987; Kobayashi & Amaral, 2000, 2003, 2007; Mufson & Pandya, 1984). Moreover, the retrosplenial cortex also exhibits reciprocal connections with prefrontal cortices (dorsolateral, medial and frontopolar prefrontal cortex; orbitofrontal cortex)(Morris, Pandya & Petrides, 1999), the visual cortex (area V4; see **Chapter 2** for a more extensive account of retrosplenial-visual connectivity) and other cingulate areas (posterior cingulate Brodmann areas 23 and 24).
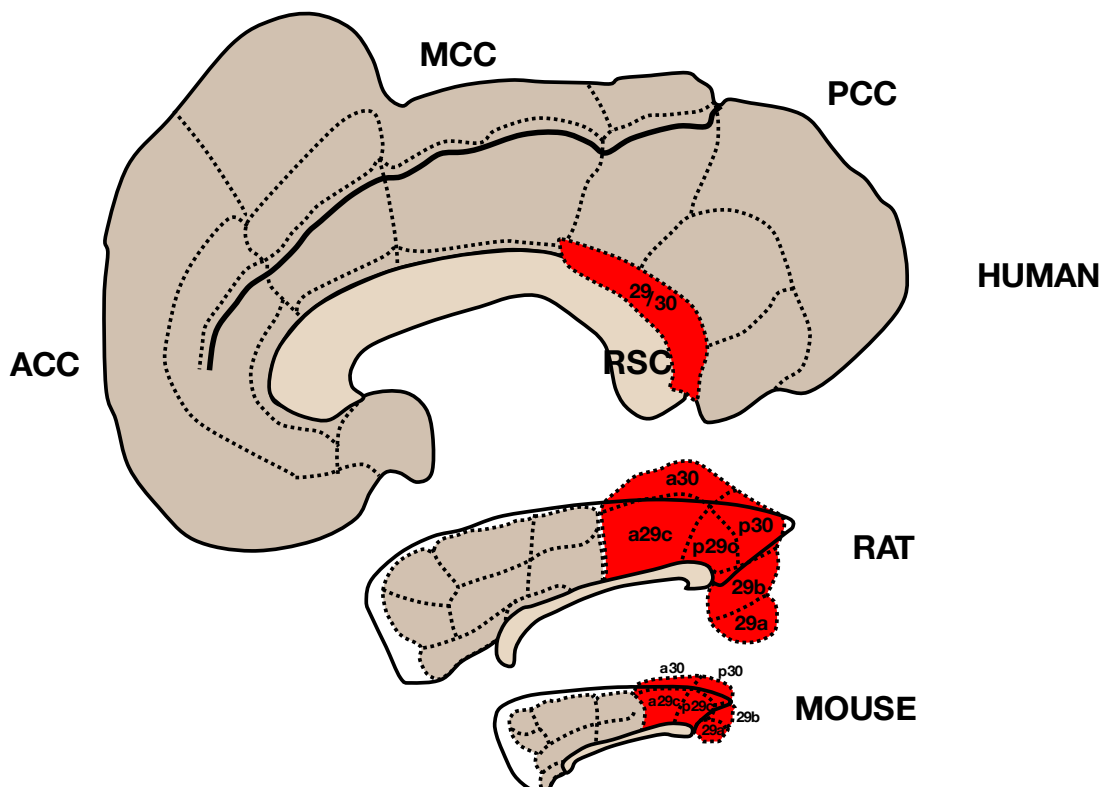
Figure 1.1.3. The cingulate cortex and its equivalent in mouse and rat. The diagrams represent unwrapped cingulate cortices, allowing for the appreciation of their relative size in the three species. ACC – anterior cingulate cortex, MCC – medial cingulate cortex, PCC – posterior cingulate cortex, RSC – retrosplenial cortex. In mouse and rat, the RSC can be subdivided into the granular (area 29) and dysgranular (area 30) parts. Granular

retrosplenial cortex is further divided into areas a, b and c according to Vogt (Vogt & Paxinos, 2014) or a and b (area b encompassing b and c on this diagram) according to van Groen and Wyss (1992). Moreover, dysgranular RSC and granular area b/c are often considered also based on their rostrocaudal position (here the a prefix denotes anterior and p, posterior). Modified from (Vogt & Paxinos, 2014).

Experiments in rodents show a homologous set of retrosplenial connections to those of the primate brain. The connectivity of the rat retrosplenial cortex is summarised in Figure 1.1.5. The rat granular a subdivision (Rga) receives inputs from the anterodorsal and laterodorsal thalamic nuclei, the postsubiculum (as well as presubiculum and ventral subiculum), caudal retrosplenial granular area b (Rgb) and contralateral Rga. Rga innervates both of its thalamic input regions, the anteroventral thalamic nucleus, caudal dysgranular retrosplenial cortex (Rdg), the postsubiculum and contralateral Rga (van Groen & Wyss, 1990a). Rgb receives its connections from anteroventral, anterodorsal and laterodorsal thalamic nuclei, dorsal subiculum and postsubiculum as well as the anterior cingulate, visual area 18b, claustrum and contralateral Rgb. Its projections include the anteroventral and laterodorsal thalamic nuclei, postsubiculum, anterior cingulate, area 18b, Rga, ventral pontine nuclei and contralateral Rgb (van Groen & Wyss, 2003). Finally, the Rdg subdivision receives inputs from the anteromedial, laterodorsal and reuniens thalamic nuclei, area infraradiata, Rga, contralateral Rdg, postsubiculum and visual areas 17 and 18b. Its projection targets include area infraradiata, caudate, lateral and anterior thalamic nuclei, both granular subdivisions of the retrosplenial cortex (Rga, Rgb), area 18b and postsubiculum (van Groen & Wyss, 1992). All three retrosplenial subdivisions additionally receive modulatory input from the diagonal band, raphe nuclei and locus coeruleus.

The pattern of connectivity in the mouse is similar but not as well established as in the rat (Oh et al., 2016). Nevertheless, a number of studies investigating functional connectivity in the mouse present a very similar picture (see below).
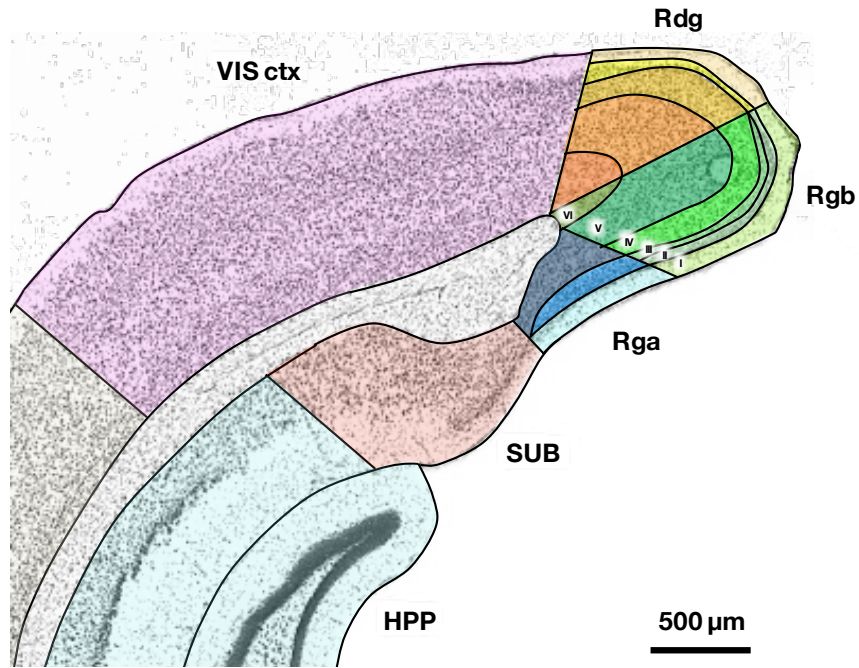
Figure 1.1.4. The cytoarchitecture and subdivisions of the mouse retrosplenial cortex based on (Paxinos & Fraklin, 2012). The figure displays a coronal slice of the posterior retrosplenial cortex, which contains all its subdivisions. Roman numerals denote cortical layers. Rdg – dysgranular retrosplenial cortex, Rgb – granular b retrosplenial cortex, Rga – granular a retrosplenial cortex, SUB – subiculum, HPP – hippocampus, VIS ctx – visual cortex.
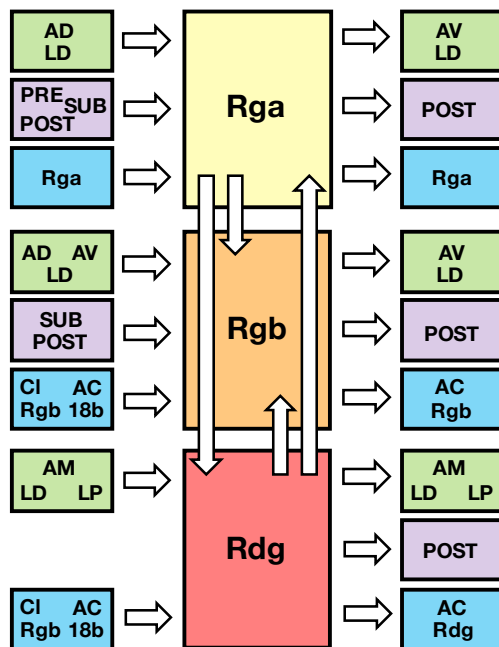
Figure 1.1.5. A summary of the connectivity of the rat retrosplenial cortex (modified from (van Groen & Wyss, 2003). The boxes in the middle represent the three subdivisions of the retrosplenial cortex: granular area a (Rga), granular area b (Rgb) and the dysgranular area (Rdg). Boxes shaded in green represent structures within the thalamus (anterodorsal nucleus – AD, laterodorsal nucleus – LD, anteroventral nucleus – AV, anteromedial nucleus

– AM), boxes shaded in violet represent the subdivisions of the subiculum (presubiculum – PRE, postsubiculum – POST, subiculum proper – SUB) and boxes shaded in blue represent cortical areas (anterior cingulate – AC, secondary visual cortex – 18b) and claustrum – Cl. The arrows denote the direction of the connections.

Evidence for the functional relevance of retrosplenial connections is further demonstrated by neuroimaging studies in humans and rodents. A meta-analysis of eight positron emission tomography studies in humans revealed the co-activation of the retrosplenial, prefrontal and occipital areas during random episodic silent thinking (that is unrestricted thought wandering, including recollection of past events, mental imagery, emotions as well as imagination) (Mazoyer et al., 2001). Similarly, resting-state functional magnetic resonance studies (rsfMRI) place the retrosplenial cortex within the Default Mode Network (DMN), a set of interconnected brain regions, which show correlated activity during introspective thought, including recall of autobiographical memory. The DMN comprises the posterior cingulate cortex, retrosplenial cortex, medial and dorsomedial prefrontal cortices, lateral temporal cortex, hippocampus, parahippocampal areas and others (Andrews-Hanna, Smallwood & Spreng, 2014; Spreng, Mar & Kim, 2008). There also exists structural neuroimaging evidence for white matter connectivity between the components of the DMN (Greicius, Supekar & Menon, 2009). rsfMRI studies in mice and rats have also demonstrated retrosplenial involvement in the DMN and highlighted its strong functional connectivity with visual areas (Becerra et al., 2011; Liska et al., 2015; Lu et al., 2012; Pawela et al., 2008; Poirier et al., 2017; Sforazzini et al., 2014; Shah et al., 2015; Stafford et al., 2014; Zhang et al., 2010).

1.1.4 The retrosplenial cortex as a component of the circuit of Papez

As early as 1937, the retrosplenial cortex was recognised as a component of a wider functional network comprising the hippocampus, mammillary bodies, anterior thalamus and the cingulate gyrus (including the retrosplenial cortex). Although Papez originally proposed it to be involved in the processing of emotion (Papez, 1937), it has become apparent that the circuit is vital for memory. For that reason, the Papez system is now often referred to as the

extended memory system (Figure 1.1.6) (Aggleton & Brown, 1999; Aggleton et al., 2016; Vann, 2013; Vann, Aggleton & Maguire, 2009; Vertes, Albo & Di Prisco, 2001).

The anatomical basis of the Papez circuit has been shown in microdissection (Shah, Jhawar & Goel, 2012) and tractography (Granziera et al., 2011) studies of the human brain as well as in tract-tracing and electrophysiological experiments in the macaque (Aggleton, Vann & Saunders, 2005), cat (Parmeggiani, Azzaroni & Lenzi, 1971) and rat species (Seki & Zyo, 1984; Vann, 2013; Wyss & van Groen, 1992). Moreover, the different components of the Papez circuit show evidence of coordinated activity mediated by periods of synchronous firing in the theta band, which is thought to facilitate its role in the processing of memory (Del Vechio Koike et al., 2017; Kocsis & Vertes, 1994; Vertes et al., 2001).
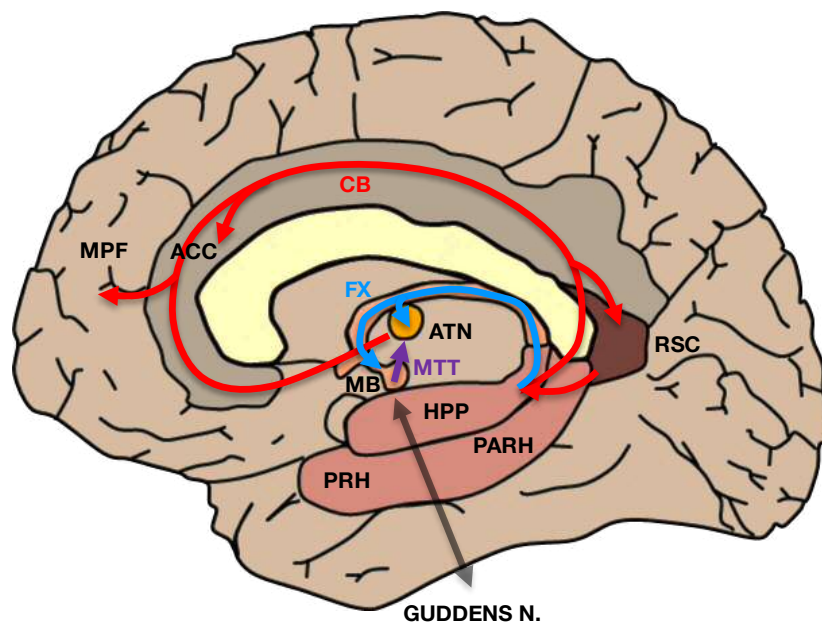
Figure 1.1.6. The anatomical connections of the extended memory system (Papez circuit). The circuit comprises projections from the hippocampus (HPP) to the anterior thalamus (ATN) and mammillary bodies (MB) carried by the fornix bundle (FX); midbrain input into the MB from the tegmental nuclei of Gudden (GUDDENS N.); a connection between the MB and ATN via the mammillothalamic tract (MTT); efferent projections from the hippocampal formation to cingulate areas including the retrosplenial cortex (RSC), anterior cingulate (AC) and medial prefrontal cortex (MPF) carried by the cingulum bundle (CB) and retrosplenial outputs to the hippocampal formation and ATN.

Consistent with a role in memory, damage to the components of the Papez system results in amnesia, most commonly of the anterograde type (inability to form new memories)(retrosplenial cortex: Bowers & Watson, 1988; Gainotti et al., 1998; Saito et al., 2003; anterior thalamus and hippocampus: Harding et al., 2000; Nishio et al., 2011; Park, Seo & Yoon, 2007; Squire, Amaral & Press, 1990; mammillary bodies: Kapur et al., 1996; Shear et al., 1996; Squire et al., 1990; Tanaka et al.,1997; frontothalamic connections: Tanji et al., 2003; fornix: Thomas, Koumellis & Dineen, 2011; splenium of the corpus callosum and parahippocampal area: Ay et al., 1998). Moreover, severe memory impairment is also found when diffuse damage occurs at multiple sites within the Papez system, as is the case in the sufferers of Korsakoff's Syndrome (Fazio et al., 1992; Nahum et al., 2015; Shear et al., 1996; Squire, 1981). One of the goals of the work presented in this thesis has been to further elucidate the effects of damage to the Papez circuit, which is described in **Chapter 4** along with a more-in-depth discussion of retrosplenial involvement in amnesic syndromes. A wider account of the role of the retrosplenial cortex in memory is also discussed in **Chapter 3**, which presents physiological evidence supporting its involvement in the processes of memory encoding and retrieval.

1.1.5 The role of the retrosplenial cortex in navigation

Another major role of the retrosplenial cortex, beside that in memory, is its proposed involvement in navigation. Around 10% of retrosplenial neurons are head-direction cells (Chen et al., 1994; Cho & Sharp, 2001; Jacob et al., 2017; Lozano et al., 2017), that is cells whose firing frequency correlates with the direction the animal is facing. In the retrosplenial cortex, these cells exhibit activity not only in relation to self-generated information, provided by vestibular, proprioceptive and motor inputs, but also in response to visual landmarks (Alexander & Nitz, 2015; Jacob et al., 2017; Lozano et al., 2017). Such integratory activity may be important for anchoring idiothetic (self-centred) inputs to the allothetic (landmark-based) representation of the environment and computational models support the plausibility of this kind of processing by

retrosplenial circuits (Bicanski & Burgess, 2016). The retrosplenial cortex is also reciprocally connected to other head-direction areas, including the anterodorsal thalamic nucleus (Shibata, 1993a, 1993b; Taube, 1995; van Groen & Wyss, 1990a, 2003) and postsubicular cortex (Shibata, 1994; Taube, Muller & Ranck, 1990; van Groen & Wyss, 1990a, 1990b, 1992). While retrosplenial input is not required for the presence of thalamic head-direction signal, it may contribute to its stabilisation by providing a global reference frame (Shine et al., 2016). This would be consistent with the finding that lesions of the retrosplenial cortex lead to unstable coding of anterior thalamic head-direction cells (Taube, 2007). Place cells, that is neurons showing preferential activity at certain environmental locations, have also been found in the retrosplenial cortex (Mao et al., 2017) and shown to have many similarities with their hippocampal counterparts, including stability in the dark. These cells may be involved in the tracking (by summation and compartmentalisation) of the animal's movement through the environment, as seen in the periodic activity of retrosplenial neurons upon navigating simple tracks such as the T-maze and a cross-shaped track (Alexander & Nitz, 2017; Vedder et al., 2016). Nevertheless, to date there exists no account of retrosplenial place cells in classical open-field environments (which were originally used to show hippocampal place cells), suggesting that tracking of location within the retrosplenial cortex may require input beyond simple self-motion cues.

Consequently, the retrosplenial cortex may be play a vital role in the translation of egocentric and allocentric world views when constructing internal representations of the environment, be it during navigation, recall of past events or planning of future actions (Evans et al., 2015; Vann, Aggleton & Maguire, 2009).

1.1.6 Retrosplenial cortex as a visual area

Connections of the retrosplenial cortex with visual areas also imply its role in sensory perception. Human neuroimaging studies place the retrosplenial cortex within the framework of the dorsal visual stream. The dorsal visual stream

includes posterior parietal areas involved in the 'where' or 'how' of visual imagery as opposed to the 'what' processed by the inferotemporal ventral stream. The two pathways are segregated not only anatomically but also by their predominant inputs. The dorsal stream receives most of its inputs from the magnocellular geniculate projections, which show high temporal and low spatial frequency sensitivity while the ventral stream receives most of its input from parvocellular geniculate projections showing sensitivity to low temporal and high spatial frequencies (Norman, 2002). The dorsal visual stream is therefore specialised to perceive the coarse features of dynamic scenes, while the ventral stream is suited for processing the fine detail of static objects (Bar, 2009). The retrosplenial cortex has been shown to respond more strongly to images of faces (Vuilleumier et al., 2003) and scenes (Bar, 2004; Watson et al., 2016) filtered to contain low compared to high spatial frequency features.

The sensitivity of the retrosplenial cortex to visual stimulation is consistent with its placement within the group of scene-selective brain areas. Scene-selective areas are visually-responsive cortical sites exhibiting preferential activation upon exposure to images of scenes, as opposed to objects, faces or symbols alone (Choi & Henderson, 2015). The most commonly-studied scene-selective areas are the parahippocampal place area (PPA), the occipital place area (OPA) and the retrosplenial cortex. Consistent with its pattern of connectivity with the visual cortex, the retrosplenial cortex displays highest blood-oxygen-level dependent (BOLD) activity contralaterally to the presented visual scene when assessed in fMRI studies (Groen, Silson & Baker, 2017). On the other hand, in contrast to other scene-selective areas, the retrosplenial cortex does not show clear preference along the vertical axis of the visual field, responding equally to low-lying and elevated visual stimuli (Groen, Silson & Baker, 2017), indicating it may be involved in the processing of scenes in their entirety. Furthermore, the investigation of the dependence of retrosplenial activity on the dimensionality of scenes revealed that it is more likely to process simple geometric features rather than the three-dimensional arrangement of its components (Henderson, Larson & Zhu, 2008). This would be consistent with the lack of its involvement in the

assessment of the spatial affordability of potential navigational paths (that is whether they can be traversed based on the presence of environmental obstacles), unlike other scene-selective areas (Bonner & Epstein, 2017). Yet, despite evidence suggesting possible retrosplenial engagement in processing of medium-to-low level visual features, a recent study revealed it was insensitive to the statistical properties of visual imagery, as assessed with scrambled scenes (Watson, Andrews & Hartley, 2017). Furthermore, while other scene-selective areas were shown to accurately classify presented scenes based on their basic visual properties (such as texture and contrast level), this was not the case for the retrosplenial cortex.

The retrosplenial cortex may therefore be functionally distinct from the other two scene-selective areas. Its specific role may be that of relating navigationally-relevant visual landmarks to internal representations of space. Multiple studies have shown retrosplenial engagement in the encoding and retrieval of landmarks in passively-viewed or actively-explored environments (Auger & Maguire, 2013; Auger, Zeidman & Maguire, 2015, 2017; Burles, Slone & Iaria, 2016; Patai et al., 2017). Moreover, the level of retrosplenial activity correlates with the abundance and permanence of visual landmarks and is predictive of navigational aptitude (Auger & Maguire, 2013). On the other hand, the size and perceived salience of objects in an environmental scene does not influence retrosplenial activity (which would argue against it processing basic visual features). The importance of the retrosplenial cortex for efficient landmark-based (or allothetic) navigation is also highlighted in patients with damage to this structure, which has been shown to result in severe spatial disorientation. While patients are able to identify environmental features, they lack the ability to utilise this information to plan their routes (Aguirre & Esposito, 1999; Gainotti et al., 1998; Greene, Donders & Thoits, 2006; Osawa, Maeshima & Kunishio, 2008; Takahashi et al., 1997).

The role of the retrosplenial cortex in visual processing may also be that of identifying and suppressing permanent but irrelevant visual information, including much simpler objects than real-world landmarks. In a visual search

guidance paradigm where participants trained to locate a reward-related visual object, the retrosplenial cortex was shown to facilitate the effect of contextual cuing, that is a form of incidental learning allowing to ignore repeating, irrelevant visual information which hinders rapid fixation on the behaviourally-relevant object (Pollmann et al., 2016). In this study, as well as in another related study in the macaque (Mccoy et al., 2003), retrosplenial responses were shown to strongly react to the actual or expected value of visual targets. Moreover, in the macaque, retrosplenial neurons were shown to fire in response to saccadic eye movements, indicating a role of the retrosplenial cortex in oculomotor behaviours such as gaze shifting. Interestingly, the retrosplenial cortex issues projections to the superior colliculus and these exhibit plastic changes following retinal enucleation, which may be sign of a homeostatic compensatory mechanism (García, Gerrikagoitia & Martínez-Millán, 2001). The retrosplenial cortex may also be crucial for assigning negative valence to ethologically-relevant stimuli. In a study in the Mongolian gerbil, lesions of the retrosplenial cortex led to greatly diminished instinctual avoidance behaviour upon presentation of an overhead visual threat, which was more severe than following lesions to the visual cortex itself (Ellard & Chapman, 1991).

The retrosplenial cortex may also categorise visual objects irrespective of their emotional valence but based on their semantic meaning. Modelling variance within all three scene-selective areas (parahippocampal place area, occipital place area and retrosplenial cortex) upon presentation of movies of natural scenes revealed that it was better explained by the category of the observed objects (cars, humans, animals, etc.) than by the lower-level visual features such as spatial texture and layout. Interestingly, all three scene-selective sites were shown to be further subdivided into two anatomical subdomains exhibiting more selective activity in response to either static or dynamic objects (Huth, Nishimoto & Gallant, 2016). Such is the prominence of the retrosplenial cortex in visual scene research that authors of the aforementioned publication categorise it as part of the visual cortex itself!

The retrosplenial cortex may also have a role in propagating visual information to other areas (see **Chapter 2**), which may contribute to its involvement in the processing of memory. For example, the hippocampus and primary visual cortex have been observed to exhibit coordinated bouts of spatial memory replay during slow-wave sleep, which is thought to facilitate the maturation and consolidation of memory (Ji & Wilson, 2007). Hippocampal replay events trail behind activity within the visual cortex by about 56 ms, a time-window consistent with the involvement of intermediary sites in the communication between the two regions. As such, the retrosplenial cortex might be one of the routes via which such communication occurs. Theta-band synchronisation between the hippocampus and retrosplenial cortex during paradoxical sleep is thought to mediate both long-term memory consolidation but also potentially the emergence of vivid perceptual scenery during dreaming (implicating involvement in offline visual processing)(Del Vechio Koike et al., 2017).

1.1.7 Retrosplenial cortex and disease

The engagement of the retrosplenial cortex in multiple networks supporting memory, navigation and visual processing may come at a cost of its vulnerability to disequilibration of its inputs. The retrosplenial cortex is often seen as a site of secondary pathology in range of conditions. The sensitivity of the retrosplenial cortex to discrete lesions within the Papez circuit as well as more diffuse damage, as seen in cases of chronic alcohol abuse, is discussed in **Chapter 4**.

The retrosplenial cortex is one of the first brain regions to show hypoactivity in Alzheimer's Disease and mild cognitive impairment (Aggleton et al., 2016; Nestor et al., 2003; Valla, Berndt & Gonzalez-Lima, 2001) and it shows increased levels of amyloid deposition in both conditions (Buckner et al., 2005; Forsberg et al., 2008). Moreover, rsfMRI indicates diminished connectivity between the components of the default mode network (DMN)(including the retrosplenial cortex) already at early stages of the disease (Bai et al., 2008; Sheline et al., 2010; Wang et al., 2007; Wang et al., 2006). Furthermore, atrophy of the retrosplenial cortex may also be the defining feature of the human

immunodeficiency virus associated neurocognitive disorder where it shows a relationship with the degree of verbal memory and fine motor skill impairment (Shin, Hong & Choi, 2017). Altered connectivity within the DMN has also been observed in a number of psychiatric disorders, including attention deficit hyperactivity disorder, autism spectrum disorder, depression and paranoid schizophrenia (Cherkassky et al., 2006; Greicius, 2008; Starck et al., 2013; Weng et al., 2009; Zhou et al., 2007). Abnormally high retrosplenial activity, on the other hand, has been implicated in the pathogenesis of secondary hyperalgesia in fibromyalgic patients (Wik et al., 2003).

Consequently, both increases and decreases in retrosplenial activity as well as change in the strength of its connections may be linked to the development of various pathologies. For that reason, further understanding of its basic biology and sensitivity to disruption is a major goal of neuroscience research.

1.1.8 Overview of the experimental chapters

Work presented in this thesis has been described in three experimental chapters. While these three chapters test a wide scope of hypotheses and employ a number experimental techniques, they all converge on the topic of the retrosplenial cortex in health and disease. Since the retrosplenial cortex appears to be engaged in a number of functional networks, a true understanding of its role requires a multifaceted approach. **Chapter 2** investigates retrosplenial contributions to visual processing in mice. Three groups of animals were presented with a set of drifting gratings under varying levels of anaesthesia in order to probe whether the retrosplenial cortex exhibited evidence of responses to basic visual stimulation. It was hypothesised that drifting gratings would elicit intrinsic signal activity within an anatomically-defined area within the retrosplenial cortex displaying sensitivity to low spatial and high temporal frequencies, as would be expected for a region of the dorsal visual stream (see above). **Chapter 3** examines the formation and persistence of spatial memory in genetically-modified mice expressing the green fluorescent protein in active neurons. It was hypothesised that training on a spatial reference memory task

would lead to the formation of a stable neuronal representation that would persist over time and show a relationship with animal performance. Finally, **Chapter 4** explores the vulnerability of the retrosplenial cortex to disconnection within the Papez circuit by employing diffusion tensor MRI imaging as well as staining for a marker of metabolic activity in the rat. It was hypothesised that transection of the mammillothalamic tract would lead to widespread microstructural changes as well as reduction of metabolic activity in the retrosplenial (and dorsal hippocampal) region.

Taken together, these three experimental chapters focus on the contribution of the retrosplenial cortex to visuospatial processing and visuospatial memory and employ intrinsic signal, immediate-early-gene and magnetic resonance imaging techniques. The rationale for choosing these methods is discussed in the following chapters.

2 Intrinsic signal imaging of retrosplenial visual responses

2.1 Introduction

Our understanding of the role of the retrosplenial cortex has come a long way since the original proposal of its involvement in the processing of emotion by James Papez (1937). While the retrosplenial cortex might still be important for emotion (Maddock, 1999), converging anatomical and functional evidence indicates that it may be especially well-suited for integrating multiple information streams in support of various aspects of cognition, such as episodic memory, navigation, imagination and planning for the future (Vann, Aggleton & Maguire, 2009). One relatively underexplored facet of retrosplenial function is its proposed involvement in visual processing. Although human studies place the retrosplenial cortex among several scene-selective areas (see **Chapter 1**), little is known about its contributions to more basic visual processing, partly owing to the inherent limitations of the available neuroimaging methods (such as low temporal or low spatial resolution). For that reason, the understanding of the characteristics of visual features that may be processed in the retrosplenial cortex necessitates supporting experiments in animal models. Work presented in the following chapter examines retrosplenial activity upon presentation of simple visual stimuli in mice and contrasts it with the activity evoked in the visual and somatosensory cortices.

2.1.1 Retrosplenial connectivity suggests its role in visual processing

In rodents, both primary and secondary visual cortical areas exhibit dense reciprocal connections (mainly ipsilateral) with all subdivisions of the retrosplenial cortex (Olsen et al., 2017; van Groen & Wyss, 2003; Velez-Fort et al., 2014; Vogt & Miller, 1983; Wang & Burkhalter, 2007; Wang, Gao & Burkhalter, 2007; Wang, Sporns & Burkhalter, 2012; Wilber et al., 2015; Zingg et al., 2014). Tract-tracing in the macaque brain has also identified direct projections between the visual (area V4) and retrosplenial cortices, as well as indirect routes (claustrum and pulvinar) via which visual information may reach the retrosplenial cortex (Vogt, 1985).

The number of retrosplenial projection neurons innervating the mouse primary visual cortex exceeds that of any other cortical area, including contributions from secondary visual cortices (Leinweber et al., 2017). While this may be related to the relatively large size of the rodent retrosplenial cortex (which comprises nearly half the length of the cerebrum in mice and rats), the numerous retrosplenial inputs may play a vital role in modulating the balance of bottom-up and top-down excitatory drive. For example, a study by Makino & Komiyama (2015) has shown increasing retrosplenial and decreasing sensory influence at layer 2/3 primary visual cortex pyramidal cell synapses during the acquisition of a visual discrimination task. Such plastic changes are thought to improve the animal's ability to predict and categorise visual stimuli based on internally-stored representations as well as diminish perceptual noise.

Further evidence for the functional connectivity between visual and retrosplenial areas comes from multiple resting-state functional magnetic resonance (resting-state fMRI) studies in rodents, which show moderate-to-strong correlations in baseline activity between the two regions (Becerra et al., 2011; Lu et al., 2012; Pawela et al., 2008; Poirier, Huang et al., 2017; Sforazzini et al., 2014; Shah et al., 2015; Zhang et al., 2010). In contrast, one of the first accounts of resting-state connectivity in humans described a negative activity correlation pattern for lateral visual cortical areas and the retrosplenial cortex (more specifically, its dysgranular portion/Brodmann Area 30)(Beckmann et al., 2005) while a more recent study found evidence for both correlated (with extrastriate visual cortex) and anticorrelated (mostly with striate visual cortex) activity between the retrosplenial cortex and visual cortices (Smith et al., 2012). It remains, however, unclear whether apparent anticorrelations of the resting-state signal reflect a genuine phenomenon or perhaps arise from the treatment of data alone (Murphy et al., 2009).

Xu, et al. (2007) observed the existence of visually-evoked and spontaneous cortical waves of depolarisation originating in the primary visual cortex of the rat and spreading across secondary visual areas and, eventually, into the

retrosplenial cortex. Moreover, functional studies in rodents also indicate the role of the retrosplenial cortex as a relay of visual information to other brain sites, particularly the hippocampal formation and frontal cortices. Electrical stimulation of the visual cortex in rat brain slices has been shown to generate waves of oscillatory activity within the retrosplenial cortex, which subsequently travelled back toward the visual cortex and forward, toward the postsubiculum (Kaneyama et al., 2007; Yoshimura et al., 2005). This putative circuit shows evidence of reorganisation upon longer stimulation periods, which results in faster and more efficient communication. The presence of circuit-level short-term plasticity between the retrosplenial and visual cortices highlights the functional relevance of their connections. Dysgranular retrosplenial cortex (along its rostrocaudal extent) has also shown responses to transcranial magnetic stimulation of the posterior parietal association area (a secondary visual area) under flavoprotein imaging, a technique bearing similarities to intrinsic signal imaging (see below) (Hishida, Kudoh & Shibuki, 2014). The retrosplenial cortex acted as a relay station propagating the signal further into the anterior cingulate and frontal areas. On the other hand, a different study employing actual visual stimulation and the same imaging technique did not observe defined retrosplenial responses (Tohmi et al., 2006). A possible explanation for the lack of retrosplenial signal might be that animals were stimulated with only simple light flashes delivered monocularly.

2.1.2 Properties of visual features processed by the retrosplenial cortex

Despite multiple lines of evidence implicating the retrosplenial cortex in aspects of visual processing (also see **Chapter 1**), supporting physiological data are scarce. To date, only a single publication has explicitly examined retrosplenial responses to varying properties of basic visual stimuli. In their study, Murakami et al. (2015) used a combination of wide-field and 2-photon calcium imaging to characterise retrosplenial activity upon presentation of drifting gratings in lightly-anaesthetised mice. They found around 13% of all neurons in the dysgranular retrosplenial cortex responded to visual stimulation. Of these, over half exhibited direction and orientation selectivity, which are features characteristic of neurons

within classical visual areas. Surprisingly, the spatial and temporal tuning properties of these cells did not align well with what might be expected for a region belonging within the dorsal visual stream (see section **1.1.6: Retrosplenial cortex as a visual area**) (Glickfeld, Reid & Andermann, 2014; Kravitz, 2011; Shah et al., 2015; Wang & Burkhalter, 2007; Wang et al., 2007; Wang, Gao & Burkhalter, 2011; Wang et al., 2012).

While these results might be a true reflection of the mouse visual physiology, it cannot be ruled out they were influenced by certain methodological aspects of the study. First, imaging was carried out immediately following craniotomies, as is customary in experiments with voltage sensitive calcium dyes, and this raises the possibility of surgery-induced oedema and consequent changes to neuronal excitability. The animals were also subject to anaesthesia, which might have also affected the recorded responses. Next, spatiotemporal tuning curves were obtained from wide-field imaging of the cortex, which might have led to non-specific signals arising from adjacent tissue. Finally, chemical calcium indicators are known to label both neurons and astrocytes (with different protocols showing higher or lower specificity of neuronal labelling)(Paredes et al., 2008) and consequently, the spatiotemporal tuning curves reported by Murakami et al. may not be representative of neuronal populations alone.

The purpose of the current study was to investigate the presence of visually-evoked responses in the mouse retrosplenial cortex by employing an equivalent stimulation protocol to Murakami et al. but using a different experimental technique.

2.1.3 Intrinsic signal imaging of visually-evoked activity

The current study measured intrinsic signal responses to drifting gratings in the retrosplenial cortex of awake and anaesthetised mice. The choice of this technique was motived by its relevance to human fMRI studies (see below) and is further supported by recent findings showing it to successfully capture the functional connectivity between the visual and retrosplenial cortices during resting-state activity (Bumstead et al., 2016).

Intrinsic signal imaging (ISI) measures changes in cortical reflectance of light caused by activity-dependent alterations in the optical properties of the tissue. Originally developed by Grinvald et al. (1986), ISI has found widespread use in the study of stimulus-evoked cortical activity, predominantly in the sensory cortices (Bathellier et al., 2007; Grinvald & Hildesheim, 2004; Logothetis et al., 1999; Ma et al., 2016; Martin et al., 2006; Schiessl, Wang & McLoughlin, 2008). An example of an experimental set-up for detecting visually-evoked responses is displayed in Figure 2.1.1. The major advantages of ISI over other approaches are that it is relatively non-invasive, has high spatial and temporal resolution as well as the ability to simultaneously survey large areas of the cortex (Zepeda, Arias & Sengpiel, 2004). The main disadvantage of ISI is that it measures cortical activity only indirectly, as is the case for fMRI. Light reflectance measured by ISI depends on at least three factors, including total blood volume, oxygenation level and tissue light scattering (Narayan, Santori & Toga, 1994). Neuronal activity first leads to a local depletion of oxygen concentration which is then restored by an increase in arterial blood flow to a slightly larger region of tissue (active hyperaemia). The consequent changes in the ratio of oxy- and deoxyhaemoglobin produce one of the components (the oxymetric component) (Figure 2.1.2) of the intrinsic signal since the redox state of haemoglobin determines its light absorbance profile (Vanzetta & Grinvald, 1999). For that reason, intrinsic signals under anaesthesia show an initial decrease when measured at light wavelengths of 600 nm and above, which corresponds to the part of the light spectrum which best differentiates between deoxyhaemoglobin and oxyhaemoglobin (Ma et al., 2016). This 'initial dip', reaching its peak at around 2-4 seconds following stimulus presentation, is also a feature observed in certain fMRI studies (e.g., Kim, Duong & Kim, 2000). Moreover, it is generally considered more localised and a better correlate of neuronal activity than subsequent intrinsic signal changes (McLoughlin & Blasdel, 1998; Shtoyerman et al., 2000). The 'initial dip' is followed by the gradual lightening of tissue caused by the increase in total blood volume, which leads to a decrease in deoxyhaemoglobin and an increase in oxyhaemoglobin concentrations. This compensatory haemodynamic component of the intrinsic signal corresponds

best to what is measured by a typical BOLD response in fMRI, and is much greater in awake animals (Ma et al., 2016; Zepeda et al., 2004). Finally, light scattering is the fastest intrinsic signal component, reaching a peak at 2-3 seconds following stimulus, and is thought to reflect activity-induced reorganisation of the microarchitecture of the tissue including astrocytic swelling and capillary distension (Zepeda, Arias & Sengpiel, 2004). Mice in the current study were imaged at the wavelength of 700 nm which is most sensitive to the presence of deoxyhaemoglobin and tissue scatter and least sensitive to haemodynamic changes, consequently producing intrinsic data which is best correlated with the underlying neuronal activity (Shtoyerman et al., 2000).
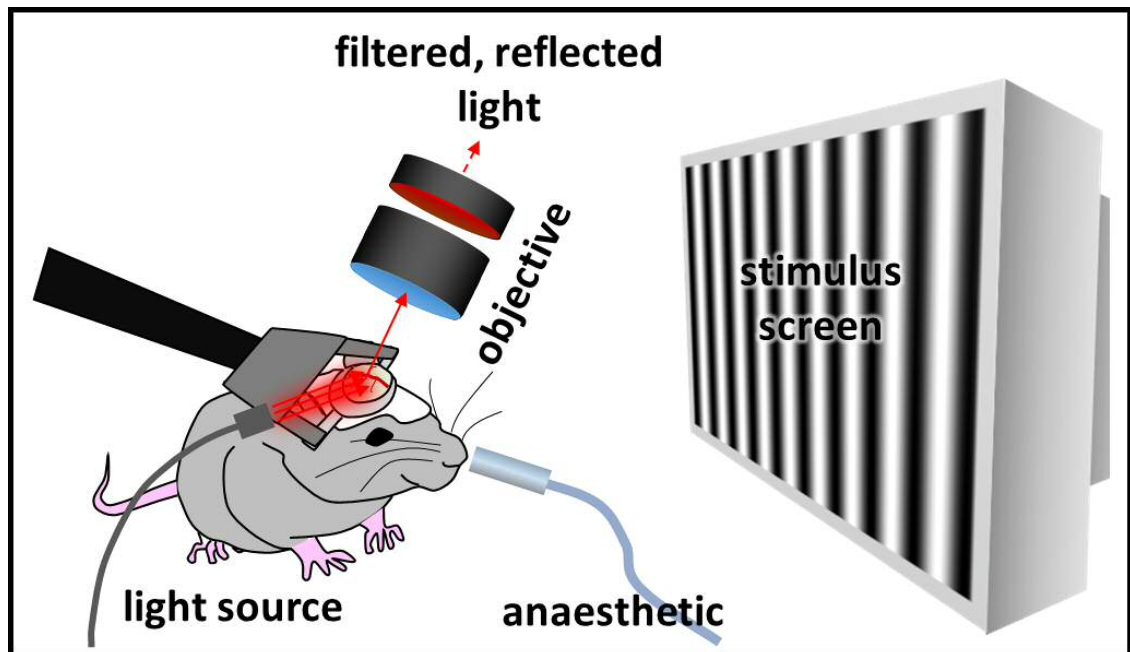
Figure 2.1.1. A diagrammatical representation of an intrinsic signal imaging (ISI) experiment. Visual stimulation is delivered by a computer screen in front of the animal. The mouse is anaesthetised and held in place by a metal fork attached to the headplate of the cranial window. The cortex of the mouse is illuminated by red LED light which is reflected into the lens of a camera objective. Prior to reaching the camera photodetector, the reflected light is filtered to a narrow bandwidth corresponding to the desired part of the spectrum.
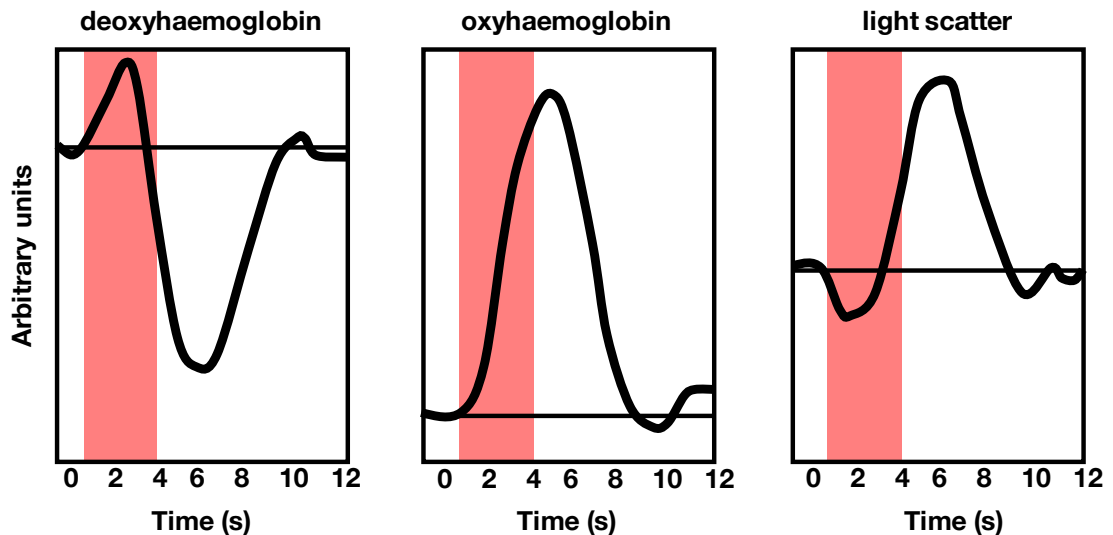
Figure 2.1.2. Comparison of the timecourses of the three main components of intrinsic signals. The y axis corresponds to the amplitude of the response. The salmon-coloured bar represents the duration of a visual stimulus. Modified from Malonek and Grinvald (1996).

The rodent retrosplenial cortex is ideally suited for ISI recordings due to its accessibility (it lies on the dorsal surface of the brain) as well as size (it occupies nearly half of the length of the cerebrum). In the present study, mice were craniotomised and implanted with glass windows to enhance the signal-to-noise ratio of the recorded signals as well as to enable repeated recording sessions in each animal. Mice were split into three groups to allow for the comparison of different levels of alertness on ISI signals: **Group 1** and **Group 2** were imaged under moderate and mild anaesthesia while **Group 3** animals were awake and allowed to run on a UFO hamster wheel.

Animals in **Groups 2** and **3** were craniotomised over the retrosplenial cortex while animals in **Group 1** were craniotomised over the visual and somatosensory cortical areas. **Group 1** served as a control introduced to assess the specificity of retrosplenial signals. While mice in all three groups were presented with a set of high-contrast drifting gratings (equivalent to those employed in the Murakami et al. (2015) study) to examine their responses to different spatiotemporal frequencies and orientations, mice in **Group 1** were also exposed to whisker pad stimulation. This allowed to indirectly address the question of the specificity of the signal by comparing intrinsic signals elicited by visual or whisker stimulation.

The distances between the primary visual cortex and the retrosplenial cortex and between the primary visual cortex and the barrel field are comparable. Second, the visual cortex and the barrel cortex are not directly connected (Wang et al., 2012) and hence any "crossmodal" responses would likely represent non-specific activity.

The current study was designed to answer a simple set of questions: 1) does visual stimulation produce activity in the retrosplenial cortex; 2) what is the spatiotemporal profile of these responses?; 3) do retrosplenial responses exhibit tuning properties for spatial frequency and orientation?; 4) are signals recorded in the retrosplenial cortex specific to this cortical region?

2.2   Methods

2.2.1 Animals and surgery

Subjects were 12 male and 3 female C57BL/6 mice aged 3-6 months housed individually under a standard light/dark cycle (14h light/10 h darkness) and given *ad libitum* access to food and water.

To maximise intrinsic signal detection, mice were craniotomised and implanted with see-through glass windows. One set of animals was implanted with a cranial window (2.5×2.5 mm) over the right primary visual cortex (V1) and the posterior edge of the posteromedial barrel subfield (PMBS) (n = 5) whilst another set of animals was implanted (window: 2.5×5 mm) over the midline, exposing the retrosplenial cortex (RSC) (n = 10). Figure 2.2.1 shows a top view cortical map of the brain (adapted from the Allen Mouse Brain Atlas, (Allen Institute for Brain Science, 2017)) with the positions of the windows indicated.

Mice were anaesthetised with isoflurane (1.5-2%, 100% O_2) and the body temperature maintained with a heating pad. Each animal received an intramuscular injection of dexamethasone (30 µL; Intervet, UK) to reduce cortical swelling and a subcutaneous injection of an analgesic (50 µL of 10% solution of Meloxicam; Boehringer Ingelheim, Germany); the eyes were protected with an eye ointment (Chloramphenicol, Martindale Pharmaceuticals Ltd, UK). After placement in ear bars, the hair on the scalp was glued down with a layer of Germolene gel (Bayer, Germany) and sterilised with the application of iodine, followed by a rinse with 70% ethanol. A local, fast-acting analgesic (lidocaine; Pfizer, USA) was then injected under the scalp and the skin resected to expose the skull. The skin around the incision was sealed with tissue glue (Vetbond; 3M, USA) and dried with 70% ethanol. A layer of dental cement (Super-Bond C&B; Sun Medical, Japan) was applied and a custom-made aluminium head-plate was affixed on top of the skull.
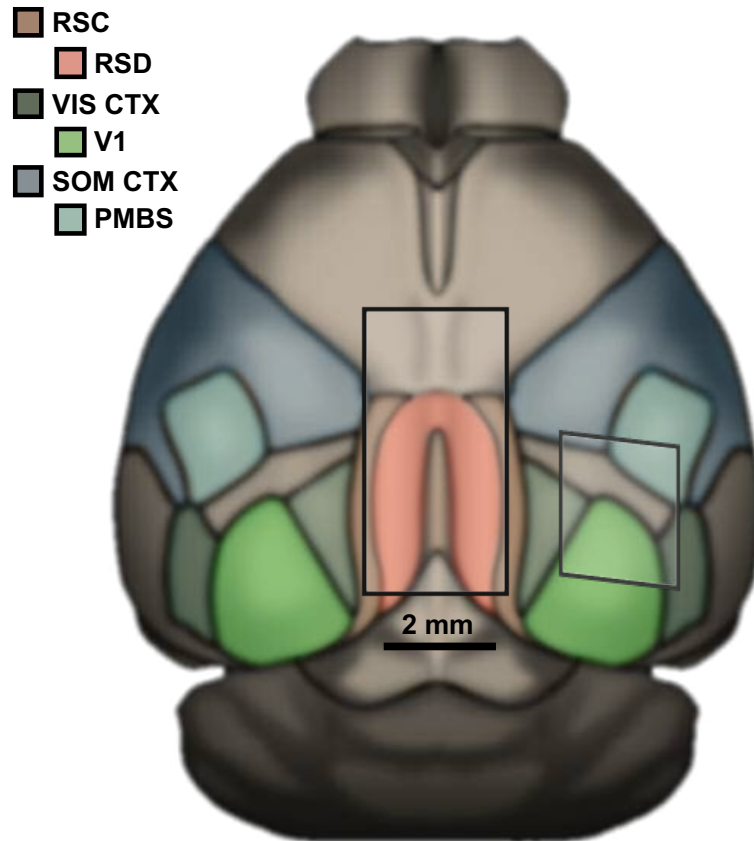
Figure 2.2.1. A top view cortical map with the positions of cranial windows. In one group of animals (Group 1), the window was implanted over the primary visual cortex (V1) and the posterior edge of the posteromedial barrel subfield (PMBS). Another two groups of animals (Groups 2 and 3) were craniotomised over the midline to expose the dysgranular retrosplenial cortex (RSD). The lines represent the subdivisions of the different cortical areas. VIS CTX – visual cortex, SOM CTX – somatosensory cortex, RSC – retrosplenial cortex.

The cement was left to dry for 20 minutes after which the animal was transferred from ear bars to a head-holder device. Excess cement was drilled off and a craniotomy was performed to reveal the cortex. The brain was rinsed several times with standard ice-cold artificial cerebrospinal fluid (ACSF) and a glass window was inserted to replace the missing skull-flap. Excess ACFS was removed and the edges of the cranial window were sealed with tissue glue, dried and secured with dental cement after which the animal was transferred to an incubator to recover. Imaging procedures began after 14 days to allow for the clearing of the windows and recovery.

2.2.2 Intrinsic signal acquisition

Recordings were taken using an Imager 3001 system (Optical Imaging Inc, Mountainside, NJ) connected to a CCD camera with a macroscope 50 mm tandem lens. The vasculature pattern was captured under green light illumination provided by a halogen box with a 546 nm bandwidth interference filter. The camera objective was then lowered by 100-150 µm to focus on the superficial cortical layers and avoid signal contamination from surface blood vessels. Intrinsic signals were recorded under red light illumination provided by a DC powered halogen lamp with a 700 nm filter and the reflected light was further filtered at 700±30 nm before reaching the camera lens. The signals were acquired at a temporal resolution of 100 ms and a spatial resolution of 20 µm/pixel.

2.2.3 Visual stimulation

The visual stimuli comprised a set of black-and-white square drifting gratings at a 100% contrast level. 12 distinct stimuli at 3 spatial frequencies and 4 orientations as well as 5 blank stimuli (grey screen) were presented in a pseudorandom order within each experimental block (the order was different in each block) (Table 2.2.1). Each recording consisted of 3 seconds of baseline preceding the stimulus, 3 seconds of stimulus presentation and 4 seconds of a grey screen until the end of each recording. The inter-stimulus interval was 16 seconds. Two animals with V1 windows received a slightly different set of gratings (Table 2.2.2) which contained 11 distinct stimuli (due to a technical problem). Within a typical experimental session, anaesthetised animals saw 25-40 blocks of stimuli while awake animals were exposed to half that number of blocks.

Table 2.2.1. The parameters of Visual Protocol 1.

STIMULUS FEATURE	STIMULUS NUMBER												
	1	2	3	4	5	6	7	8	9	10	11	12	13-17
spatial frequency (cycles/degree)	0.02	0.02	0.02	0.02	0.04	0.04	0.04	0.04	0.08	0.08	0.08	0.08	blank condition = grey screen
temporal frequency (Hz)	4	4	4	4	2	2	2	2	1	1	1	1	
orientation (degrees)	0	45	90	135	0	45	90	135	0	45	90	135	

Table 2.2.2. The parameters of Visual Protocol 2.

STIMULUS FEATURE	STIMULUS NUMBER											
	1	2	3	4	5	6	7	8	9	10	11	12-17
spatial frequency (cycles/degree)	0.025	0.025	0.025	0.025	0.05	0.05	0.05	0.05	0.1	0.1	0.1	blank condition = grey screen
temporal frequency (Hz)	4	4	4	4	2	2	2	2	1	1	1	
orientation (degrees)	0	45	90	135	0	45	90	135	0	45	90	

2.2.4 Whisker pad stimulation

Animals with V1 and PMBS windows (**Group 1**) also received whisker pad stimulation separately to visual stimulation. The whiskers were stimulated with air puffs manually delivered via tubing positioned adjacent to the left whisker pad. Each experimental block mirrored the pattern of visual stimulation experiments such that the experimenter observed the stimulus screen (facing away from the animal) and delivered three air puffs during the presentation of drifting gratings and did not deliver air puffs during grey screen presentations. Each animal received 4-8 blocks over three experimental sessions (which were the same sessions in which animals also received visual stimulation).

2.2.5 Experimental conditions

There were three experimental groups in the study. Five mice with windows over the V1 and the PMBS (**Group 1**) and 5 mice with windows over the RSC (**Group 2**) were imaged under sedation (Chlorprothixene, 0.25 mg; Sigma-Aldrich, USA) and at two levels of anaesthesia (0.7%, followed by close to 0% isoflurane) whilst a third group of animals with RSC windows (**Group 3**, n = 5) was imaged

in the absence of anaesthesia or sedation and allowed to run on a wheel during stimulus presentation. Prior to data acquisition, **Group 3** had received 5 habituation sessions of increasing length (15 min – 1 hour) during which they were shown a grey screen. Mice with windows over the RSC were presented with visual stimuli whilst mice with windows over the V1 and PMBS received both visual and whisker pad stimulation.

Among mice with V1 windows, two were presented with **Visual Protocol 2** and three with **Visual Protocol 1**. In the RSC groups, all mice were presented with **Visual Protocol 1** (see **Visual stimulation** above).

2.2.6 Data processing and analysis

Intrinsic signals were calculated in Matlab (version 14b, MathWorks, USA) as the ratio of light reflected in stimulus trials versus light reflected during grey screen presentations. For each stimulus block, each of the stimulus presentations (10-12) was divided by the mean blank (grey) screen reflectance (13-17). Values of 1 signify no change in signal, values <1 signify a decrease in reflectance (i.e. activity-evoked increase in the deoxy-/oxyhaemoglobin ratio) and values >1 signify an increase in reflectance (i.e. increase in the oxy-/deoxyhaemoglobin ratio). All Matlab scripts were written by Irina Erchova.

2.2.7 Cortical activity maps

To generate cortical maps of retrosplenial activity, images were averaged (by mean) across blocks and then across sessions for each animal. The images were further averaged (by mean) across animals. For display purposes and all subsequent analyses, only the hemisphere contralateral to the light source was considered as it reliably demonstrated higher quality responses than the ipsilateral hemisphere (due to the angle of the incident light). The mean cortical activity map was created by combining images of activity under mild and moderate anaesthesia such that the moderate activity map was placed on the left and the mild activity map, flipped horizontally, was placed on the right. The

mean cortical activity map was then overlaid with a 0.5x0.5 mm reference grid. Individual animal heat maps overlaid with the blood vessel pattern were also generated to reveal the range of responses. The intrinsic signals were expressed as % change from baseline.

2.2.8 Timecourse analysis

Intrinsic signal maps were averaged (by mean) across stimuli for each individual experimental session and the mean signal strength within free-hand selections of approximately 0.5 mm^2 (centred at the peak of activity at around 1.0 mm anterior from lambda and 0.7 mm lateral from the midline, respectively) were plotted against time. The same procedure was applied to maps of the visual cortex (size of around 0.7-1 mm^2, centred on the peak of activity). Responses were further averaged across sessions for each animal and the mean peak response, latency of peak and slope of the rising phase (0.5-1s from stimulus onset) were calculated.

2.2.9 Comparison of whisker and visual stimulus-evoked responses

Peak responses were calculated as above and activity elicited by visual or whisker stimulation within the same animals were compared. The region of interest (ROI) for the visible portion of the PMBS was approximately a third of the size of the visual ROI. The values were expressed as % change from baseline.

2.2.10 Quantification of the parameters of visually-evoked responses

Three parameters were compared: the peak response, the latency to peak and the slope of the initial rising phase of the response. The peak response allows for the comparison between the highest measurable level of activity seen in V1 and activity in other cortical regions, such as the RSC. The latency to peak, on the other hand, potentially allows for the comparison of the duration of the response and the order of synaptic separation between the retinal and cortical

neurons part-taking in visual processing. The latter also applies to the slope of the rising phase of the signal, which may, however, be a more sensitive measure as it precedes the onset of the haemodynamic response.

2.2.11 Spatial frequency and orientation tuning curves

The timecourses of intrinsic signals were further analysed to compare responses at different spatial frequencies and stimulus orientations. For that purpose, responses to the 12 stimuli were split according to the spatial frequency (0.02, 0.04, 0.08 cycles/degree) or orientation ($0°$, $45°$, $90°$, $135°$) of the gratings and averaged (by mean) across sessions and animals. Comparing peak response values or the integrated area under the curve (negative deflections) yielded very similar results, however, integration produced less variance and it was therefore used for subsequent analyses.

Integrated activity values were further converted into ratios so that RSC and V1 responses could be more easily compared (because RSC and V1 responses differed in absolute magnitude). For each spatial frequency or orientation the integrated value per animal was divided by the sum of integrated values across all spatial frequencies or orientations, respectively. In this way, the relative values for the three spatial frequencies or four orientations now added up to 1. A lack of spatial tuning would correspond to responses of 0.33 for each spatial frequency and a lack of orientation tuning would yield values of 0.25 for each orientation.

The comparison of spatial frequency preference between the RSC and V1 was carried out by expressing the sharpness of tuning as the ratio of the responses to the lowest (0.02 cycle/degree) and highest (0.08 cycles/degree) spatial frequency for each animal. For the comparison of orientation tuning, responses to cardinal orientations ($0°$, $90°$) and non-cardinal orientations ($45°$, $135°$) were averaged by mean.

2.2.12 Statistical analysis

Due to the low number of cases, only independent-samples or paired-samples t-test were used where appropriate. All statistical tests were carried out in SPSS (version 21; IBM, USA).

2.3 Results

2.3.1 Cortical spread of visually-evoked activity

Visual stimuli evoked increased light reflectance of the blood vessel areas and decreased light reflectance in the surrounding cortex (Figure 2.3.1 & Figure 2.3.2). Since lower reflectance values represent an increase in activity-related cellular respiration and higher values are brought about by compensatory increases in blood flow, the divergent pattern of reflectance change likely suggests that cortical signals were not driven by haemodynamic effects but by the instantaneous metabolic state of the cortex.

The intrinsic signals were strongest in the caudal portion of the retrosplenial cortex, around 1 mm anterior from lambda and 0.6-0.7 mm lateral from the midline and were thus largely confined within the extent of the dysgranular retrosplenial cortex. Signals in awake animals showed much higher variability and did not display an obvious anatomical location. For that reason, they are not presented in the form of average cortical maps here. From here on, the retrosplenial cortex ROI (region of interest) is referred to as RSC and the primary visual cortex ROI as V1.

2.3.2 The comparison of the strength and time-dependence of visually-evoked intrinsic signals

Following the establishment of the spread of visually-evoked activity, signals were further analysed to reveal their magnitude and time-dependence. Figure 2.3.3 depicts signal timecourses at 0.7% and 0% isoflurane anaesthesia for the V1 and RSC regions and in the awake state for the RSC region alone. Both the V1 and the RSC showed clear visually-evoked responses following stimulus presentation.
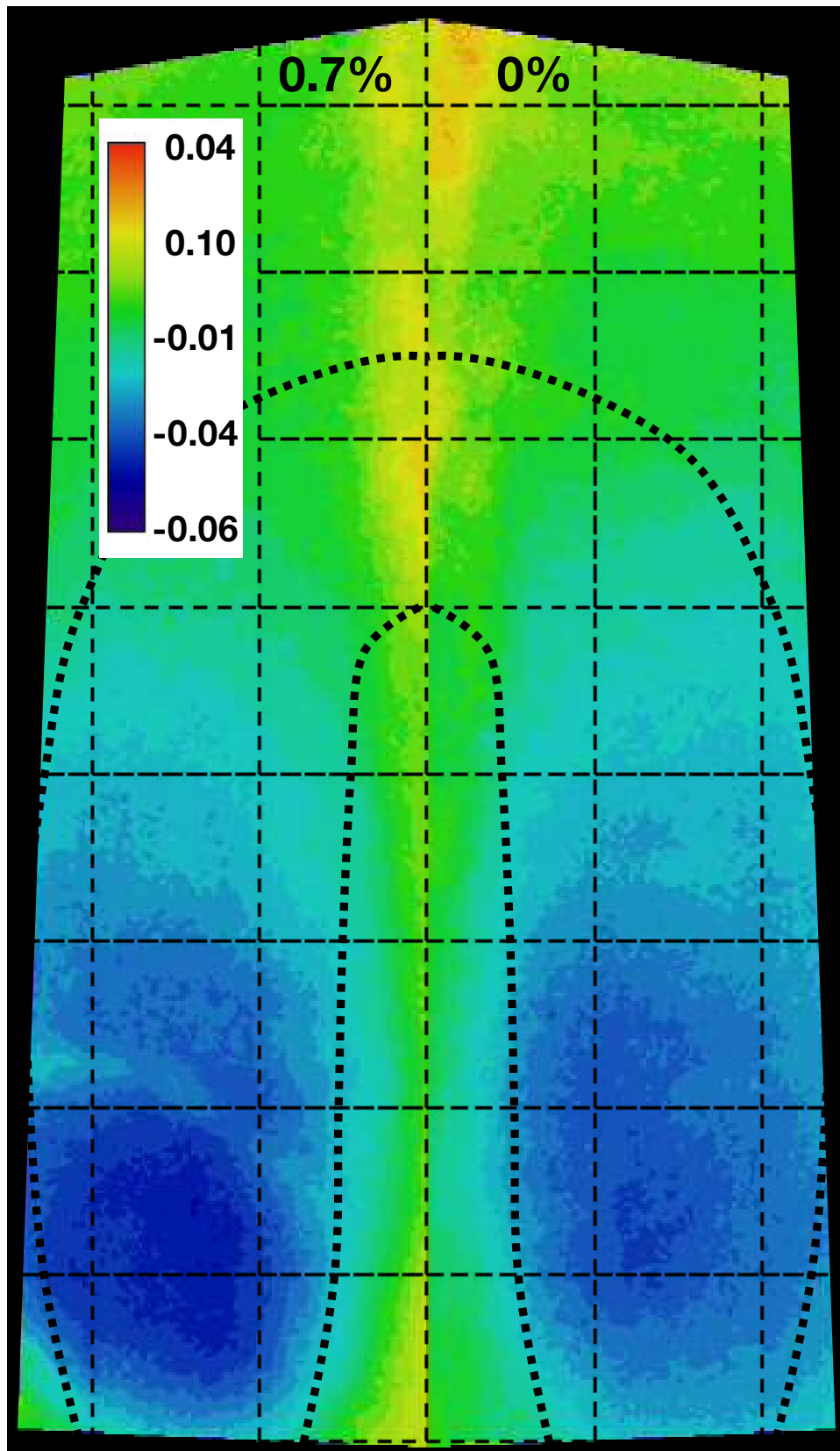
Figure 2.3.1. Mean cortical activity map of visually-evoked intrinsic responses. The boundaries of dysgranular retrosplenial are denoted by the the thick, dotted line. The grid pattern is made up of 0.5×0.5 mm squares. The left and right sides of the figure show responses recorded under moderate and mild anaesthesia, respectively (the map is horizontally flipped on the right).
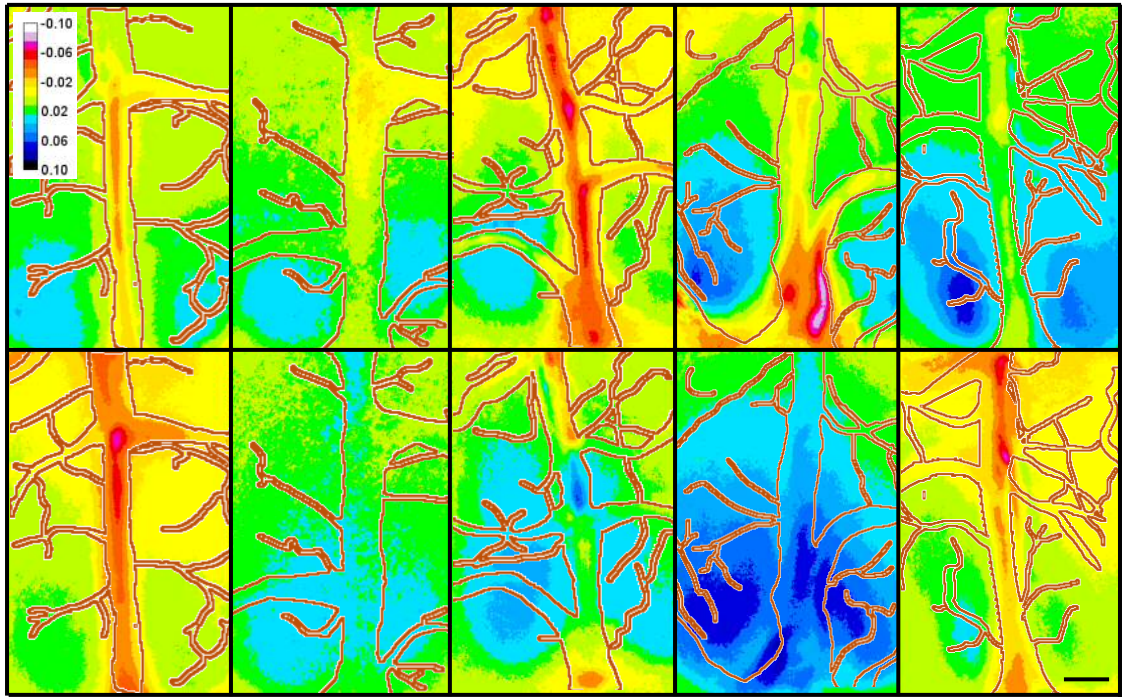
Figure 2.3.2. Individual animals' cortical activity maps with responses under 0.7% isoflurane in the top panel and responses under 0% isoflurane in the bottom panel. Red lines are outlines of large blood vessels, scalebar = 0.5mm.
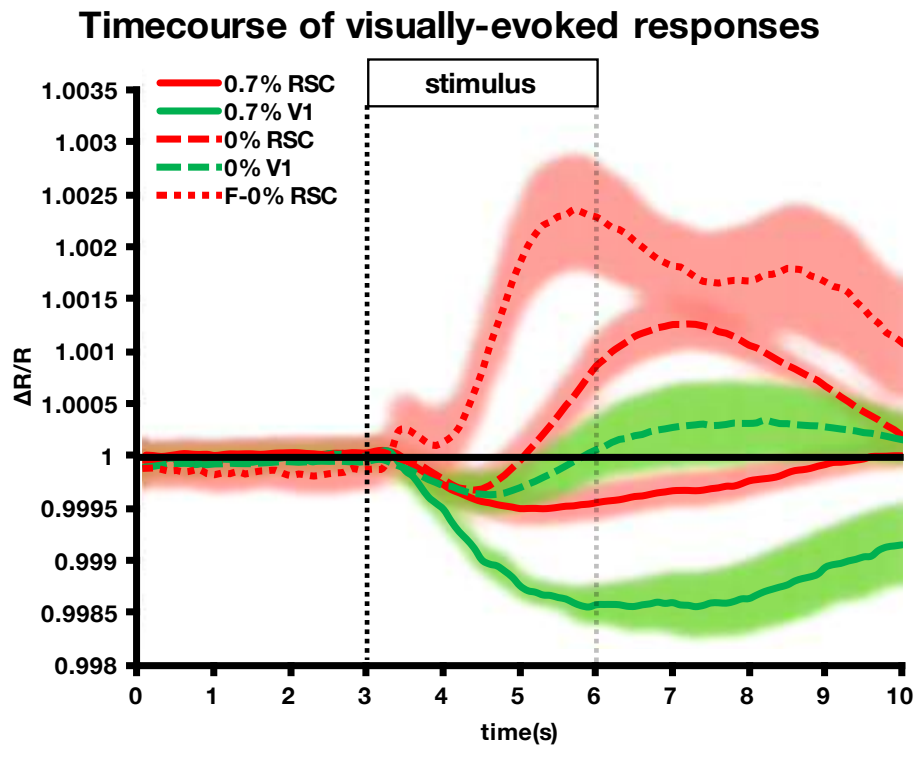
Figure 2.3.3. Intrinsic signal timecourses of visually-evoked responses in the RSC and V1 areas. Red lines show retrosplenial responses and green lines represent signals from V1. ΔR/R – stimulus versus blank reflectance ratio. The shaded areas represent error bars, which are the standard error of the mean. 0.7% RSC – retrosplenial signal under moderate

anaesthesia, 0.7% V1 – primary visual cortex responses under moderate anaesthesia, 0% RSC – retrosplenial responses under mild anaesthesia, 0% V1 – primary visual cortex responses under mild anaesthesia, F-0% RSC – responses recorded in the retrosplenial cortex of awake, freely-running mice.

Under moderate anaesthesia, both cortical regions showed a decrease in reflectance, followed by a slow return to baseline values. The peak RSC signals were one-third the size of peak V1 responses (t = 5.9, $p < 0.001$)(Table 2.3.1) and showed shorter latencies (by around 1.2 seconds)(t = 3.4, $p < 0.02$). The initial rising phase of the intrinsic signal, on the other hand, was much steeper in the V1 region (by a factor of around 2)(t = 6.06, $p < 0.001$). RSC signals diminished faster than V1 signals did, returning to baseline within 7 seconds from stimulus onset while V1 responses persisted throughout the sampling time window.

The timecourse of the intrinsic signals under mild anaesthesia showed a very different pattern. The curves displayed a biphasic shape with a negative deflection within the first 2 seconds following stimulus and a positive deflection thereafter. While the RSC peak responses did not show a significant difference between the two levels of anaesthesia (t = 1.51, $p > 0.05$), V1 peak signals diminished by over 75% (t = 12.68, $p < 0.01$) and thus reached equivalent values to RSC signals (t = 0.07, $p > 0.05$). In both areas, peak responses occurred closer to stimulus onset (V1: t = 4.39, $p < 0.05$; RSC: t = 5.39, $p < 0.01$) and no longer showed a difference (t = 1.17, $p = 0.288$). Finally, the slopes of the rising phase did not significantly differ between moderate and mild anaesthesia for either the RSC (t = 0.49, $p > 0.5$, paired-samples t-test) or the V1 (t = 3.67, $p = 0.067$), however, they were no longer different between the RSC and the V1 (t = 0.15, $p > 0.05$).

Awake animals did not demonstrate a decrease but, instead, an increase in reflectance in response to stimulus presentation. The signal showed an initial positive deflection (0-0.5 seconds from stimulus onset), followed by a small decrease in reflectance and, finally, a very high increase in ΔR/R, which continued beyond the sampling time window. Due to high noise and the lack of

a defined negative change in reflectance, which is considered a much more precise predictor of activity than increases in reflectance (Shtoyerman et al., 2000), awake recordings were not analysed further.

Table 2.3.1. Peak value, latency to peak and slope of the initial rising phase for V1 and RSC intrinsic signals. All values are presented as mean±standard error of the mean.

CORTICAL REGION		PEAK VALUE (%)	LATENCY TO PEAK (s)	SLOPE OF THE INITIAL RISING PHASE (%)
0.7 %	V1	0.155±0.019	3.4±0.45	0.087±0.007
	RSC	0.052±0.008	2.18±0.11	0.040±0.004
0 %	V1	0.037±0.011	1.58±0.07	0.033±0.009
	RSC	0.036±0.010	1.38±0.09	0.036±0.012

Together, these data provide evidence for the presence of visually-evoked activity in the retrosplenial cortex of anaesthetised animals. Recordings in mildly-anaesthetised and awake mice showed a prominent, delayed haemodynamic response, which, respectively, partially or fully occluded the intrinsic signals.

2.3.3 The specificity of recorded signals to the retrosplenial cortex

Both the V1 and PMBS (posteromedial barrel subfield) regions showed high responses to their native sensory modalities (Figure 2.3.4). The visually- or whisker-responsive areas were spatially distinct and easily identifiable (not shown here). On the other hand, responses to non-native modalities produced very low intrinsic signals, which were 85.8±1.8 and 71.4±8.0 % lower in the V1 and in the PMBS regions, respectively. As a comparison, visually-evoked intrinsic signals were over three times higher in the retrosplenial region than in the barrel cortex (t = 4.3, $p < 0.01$).

Peak responses to visual or whisker pad stimulation
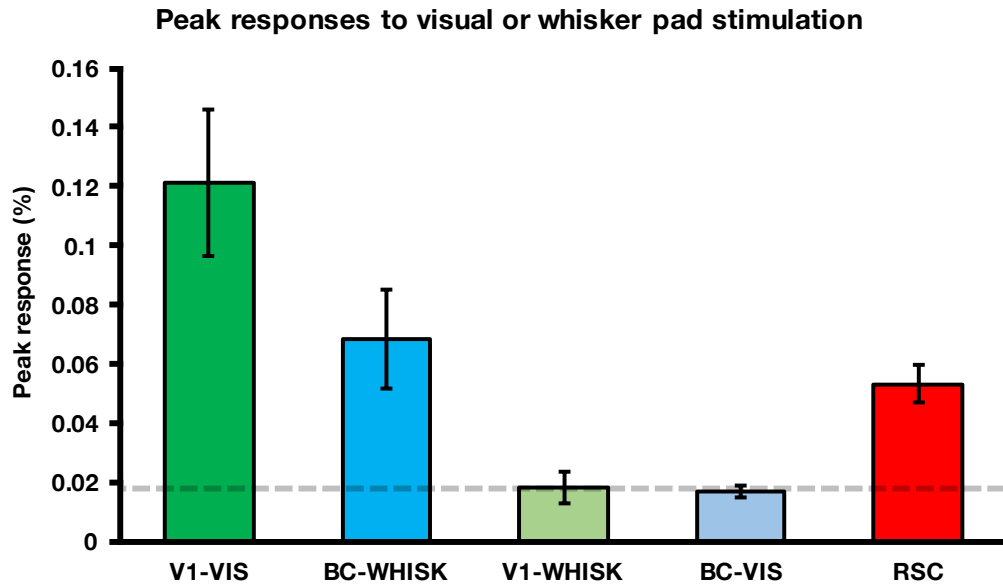
Figure 2.3.4. Bar chart of mean responses to visual stimulation (V1-VIS, BC-VIS, RSC) and to whisker stimulation (BC-WHISK, V1-WHISK). The dashed line is positioned atop the two lowest (crossmodal) responses. V1 – primary visual cortex, BC – barrel cortex, RSC – retrosplenial cortex. Error bars denote the standard error of the mean.

2.3.4 The retrosplenial cortex exhibits tuning for spatial frequency and orientation of drifting gratings

Visually-evoked intrinsic signals were further analysed for their spatial and orientation tuning properties. Both V1 and RSC showed preference for lower spatial frequencies under moderate anaesthesia (V1: $t = 51.22$, $p < 0.001$, RSC: $t = 7.68$, $p = 0.002$)(Figure 2.3.5a) whilst there was no such preference under mild anaesthesia ($p > 0.5$) (Figure 2.3.5b). Moreover, RSC displayed a stronger preference for the lowest spatial frequency than V1 under moderate anaesthesia ($t = 3.77$, $p = 0.005$). The RSC also showed a small ($14.45 \pm 2.33\%$) preference for cardinal versus non-cardinal grating orientations under moderate anaesthesia ($t = 3.97$, $p < 0.05$) whereas there was no significant difference in preference under mild anaesthesia (Figure 2.3.5d). On the other hand, in the V1 region, there were no statistically-significant differences between responses to cardinal and non-cardinal orientations at either level of anaesthesia (Figure 2.3.5d).
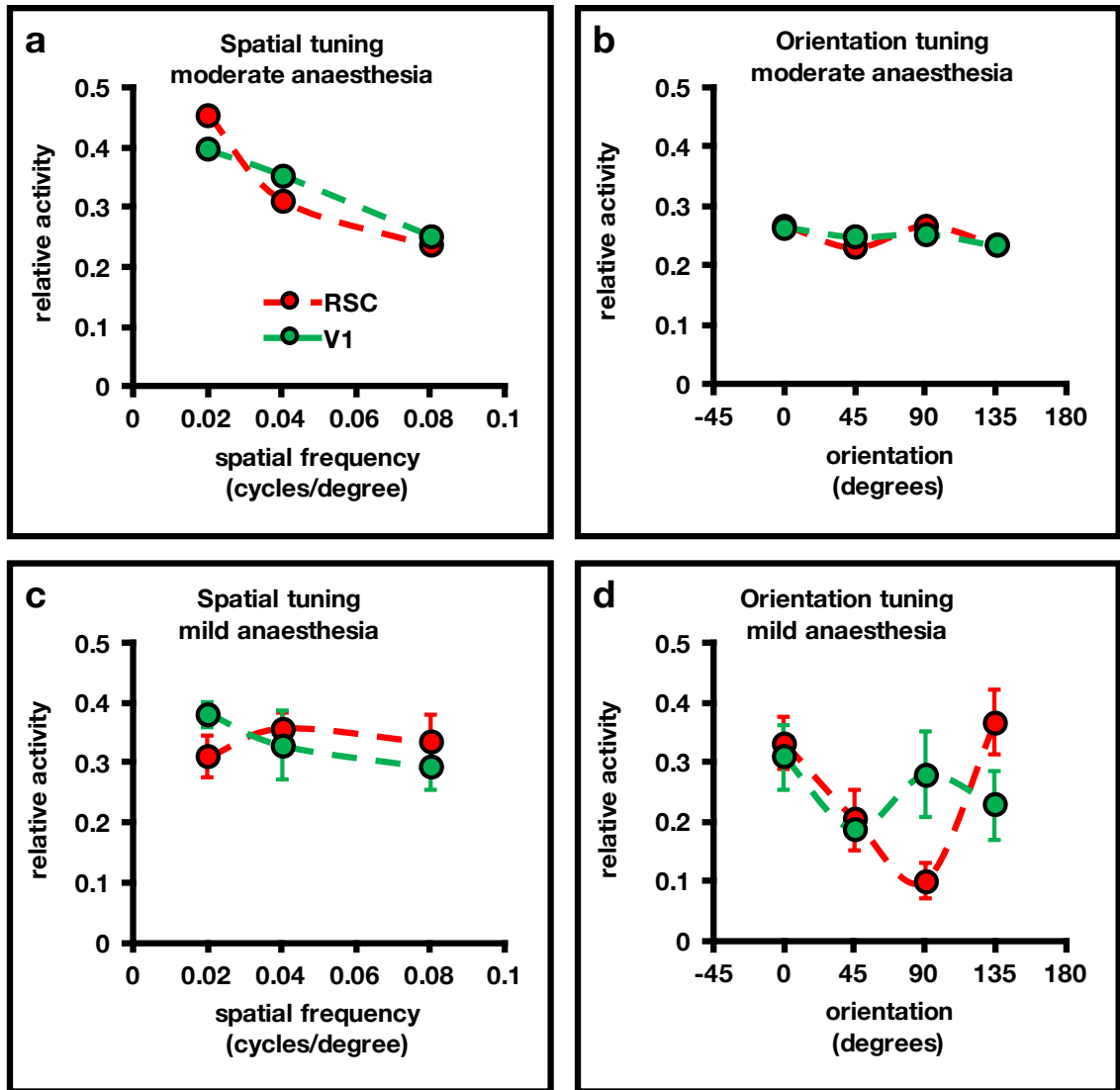
Figure 2.3.5. Frequency and orientation tuning curves displaying relative activity levels under moderate and mild anaesthesia for the RSC and V1 regions. a – spatial tuning under moderate anaesthesia, b – spatial tuning under mild anaesthesia, c – orientation tuning under moderate anaesthesia, d – orientation tuning under mild anaesthesia. Error bars represent the standard error of the mean and are buried within the symbols in a and b.

2.4 Discussion

The current study demonstrates the presence of visually-evoked intrinsic signals in the retrosplenial cortex of craniotomised mice. In anaesthetised animals, the responses varied according to the properties of the stimulus and the level of anaesthesia. Furthermore, the anatomical localisation of the signals was consistent across animals and corresponded well with previously reported retrosplenial-visual cortex connectivity (see discussion below). Conversely, the responses in awake mice were variable and masked by a large, nonspecific haemodynamic response, likely the effect of motor activity. Intrinsic signal imaging has therefore proven useful in showing that retrosplenial activity may be studied analogously to visual cortex responses albeit not under conditions allowing for further elucidation of its role in behavioural and memory processes.

2.4.1 What can the ISI tell us about retrosplenial function?

The current study characterised retrosplenial responses to visual stimulation under two levels of anaesthesia and in awake mice. The quality and reproducibility of the traces were best under moderate anaesthesia where they largely resembled "classical" intrinsic signals known from sensory areas (Grinvald et al., 1986; Masino et al., 1993; Shtoyerman et al., 2000) with peak responses at around 2 seconds post-stimulus onset and persistence for an extended period after stimulus termination. With increased levels of wakefulness, however, signals showed considerable deterioration as a large positive deflection obscured the "classical" downward intrinsic signal. The retrosplenial signal traces appear to originate from at least two opposing sources: one relating to the concentration of deoxyhaemoglobin, which causes the darkening of the cortex, and one relating to increased blood flow and tissue oxygenation, producing increased light reflectance (Grinvald & Bonhoeffer, online resource.; Vanzetta & Grinvald, 1999).

Retrosplenial signals seem particularly sensitive to the latter component due to the presence of large surface vessels in the area. In contrast to studies of the monkey visual cortex (Grinvald et al., 1991), stable traces were not obtained in fully awake animals. This may be because mice in the present study exhibited more motor activity, which contaminated the signal, as well as due to the recording and post-processing procedures. Additionally, in the current study, noisy trials were not excluded to avoid bias as there is a possibility that more salient stimuli evoke stronger motor responses. A more recent study has successfully recoded intrinsic signals in the awake rat (Martin et al., 2006). While traces were shown to exhibit a very good relationship with neuronal firing, they represented the delayed haemodynamic component of the response, which has little spatial specificity (Dunn et al., 2005). Consequently, the analysis of the delayed, positive signal deflection could have provided a general measure of cortical activity in the current study but it would not have offered the degree of spatial resolution required for demonstrating specific retrosplenial engagement in visual processing.

Nevertheless, under moderate anaesthesia we found responses that were quantitatively and qualitatively different between the retrosplenial and visual cortices. As expected, the magnitude of retrosplenial responses was significantly lower but within the same order of magnitude. We also observed the latency to peak to be shorter and the slope of the response to be lower in retrosplenial cortex compared to visual cortex. The difference in the latency to peak likely indicates that retrosplenial signals were terminated faster due to a larger vascular component of the response. On the other hand, the slope of the initial rising phase was much steeper in the visual cortex area, indicating it was recruited prior to the retrosplenial cortex. Under mild anaesthesia, visual and retrosplenial responses were similar, probably due to the higher contribution of the global, non-specific vascular response producing increased reflectance values.

It was attempted to further examine the specificity of the retrosplenial signals by recording visually-evoked activity in a non-visual area, the barrel cortex. It was found that "cross-modal" responses in the barrel cortex were weak and devoid of any distinguishable spatial profile (not shown here), which contrasted with the stereotyped signals observed in the retrosplenial cortex. This would argue for the specificity of the retrosplenial intrinsic responses recoded upon visual stimulation.

2.4.2 The question of retrosplenial topography in the rodent brain

Since the advent of the genetic revolution in neurosciences, the mouse has been increasingly employed as a model for examining cortical activity. The species is particularly well-suited for direct imaging approaches owing to its genetic manipulability as well as a small size and the relatively (to rat) flat brain surface. One of the downsides of using mouse as a model, however, is its largely uncharted brain anatomy. The precise topography of the mouse retrosplenial cortex varies from source to source, taking the form of either a narrow, ~0.5 mm band almost entirely obscured by the central sinus (Gucht et al., 2007; Nasiriavanaki et al., 2014), or a more prominent area, extending up to 1-1.2 mm from the midline (Wang et al., 2011; Zingg et al., 2014). The current study made use of the Allen Mouse Brain Atlas (Allen Institute for Brain Science, 2017) which can be viewed in a 3D form, allowing for the alignment of imaging data with the brain surface (together with post-mortem histological validation). We observed the peak of retrosplenial signals within the borders of the dorsal (dysgranular) retrosplenial cortex at around lateral 0.6-0.7 mm from midline. This was markedly different from the peak activity position of 1.2 mm away from midline attributed to the bordering posteromedial visual area (PM) in a study using equivalent methodology to ours (Roth, Helmchen & Kampa, 2012). PM was shown to occupy a focal spot which did not overlap with the responses described in our study. Furthermore, in the current study, visually-evoked responses were observed predominantly within the caudal portion of the dysgranular retrosplenial cortex with a rostrocaudal peak at around 1 mm anterior from lambda.

Whilst visual-to-retrosplenial inputs show diffuse distribution throughout the retrosplenial cortex (in both mouse and rat) (Velez-Fort et al., 2014; Q. Wang & Burkhalter, 2007; Q. Wang et al., 2007, 2012; Zingg et al., 2014), retrosplenial-to-visual projections appear to originate predominantly from the caudal portion of dysgranular retrosplenial cortex in the rat brain (Groen & Wyss, 1992), although this distinction has not been found by Wilber, et al. (2015) in the mouse. This might represent a genuine inter-species difference or reflect different methodologies used by the authors of the two studies.

The caudal subdivision of the dysgranular retrosplenial cortex is also anatomically dissociable at the intra-retrosplenial level where it shows stronger caudal versus rostral projections to both itself and other retrosplenial areas (Jones, Groenewegen & Witter, 2005; Shibata, Honda & Sasaki, 2009). The specific importance of the dysgranular subdivision of the retrosplenial cortex for visually-guided behaviour has been demonstrated in lesion studies (Hindley et al., 2014; Vann & Aggleton, 2005) and with immediate-early-gene imaging (Pothuizen et al., 2009). In particular, dysgranular retrosplenial cortex appears to provide visual context for navigational tasks and may aid in cross-modal translation between stimuli. No studies have investigated the effect of selective caudal dysgranular lesions, however, ablating the caudal retrosplenial cortex as a whole produces some subtle behavioural deficits, especially when frames of reference are changed within a navigational task (Vann et al., 2003).

2.4.3 The tuning properties of the retrosplenial cortex indicate its role in the dorsal visual stream

In contrast to Murakami et al. (2015), both the visual and retrosplenial cortices in this study showed preference for low spatial and high temporal frequencies when under moderate anaesthesia. Moreover, the preference for low spatial frequencies was stronger for the retrosplenial cortex. A V1 spatial frequency tuning curve similar to the one obtained here was also reported in another ISI study (which also employed 700 nm incident light) while other studies employing calcium-imaging revealed domed-shaped curves in V1 in response to a wider-

range of spatial frequencies (Roth et al., 2012; Salinas et al., 2017) (with most V1 neurons preferring low spatial frequencies).

Murakami, et al. explained their unexpected results by noting that the two major secondary visual cortex inputs to the retrosplenial cortex, the posteromedial (PM) and anteromedial (AM) areas, exhibit tuning properties consistent with those of the retrosplenial neurons they recorded from (Andermann et al., 2013; Glickfeld et al., 2014; Roth et al., 2012). While this may be the case, they failed to directly demonstrate it under their experimental conditions (which they could have done based on their wide-field data). Furthermore, the spread of activity following the presentation of visual stimuli in their preparation encompassed almost the entire caudal aspect of the hemisphere, making it difficult to interpret the specificity of their signal. Conversely, in the current study, retrosplenial responses were marked with a distinct spatial peak surrounded with a gradient of activity, which distinguished the retrosplenial cortex from the adjacent areas.

Finally, the authors remark that the calcium indicator used in their experiment is also expressed in astrocytes, which, according to some publications do not contribute strongly to the calcium signal. On the other hand, there have been reports of astrocytic involvement in visual processing and, what is more, astrocytes have been shown to exhibit sharp tuning properties (Schummers, Yu, & Sur, 2014) under certain conditions, making the interpretation of joint neuronal and astrocytic calcium responses difficult.

We did not observe spatial tuning under mild anaesthesia which may reflect a modulatory facilitation of spatial frequency processing or the fact that the responses originated from different neuronal ensembles (or cortical layers). Alternatively, the lack of tuning might have also resulted from increased experimental noise under lower isoflurane.

Drifting gratings of low spatial frequencies in the current study were presented at high temporal frequencies. As such, animals under moderate anaesthesia

showed a preference for high temporal frequencies. It is interesting that the prostriata region of the human cingulate cortex, which forms a bridge between the retrosplenial and visual areas, also exhibits selectivity for high temporal frequencies (Yu et al., 2012). The role for this specialisation has been proposed to be that of rapid perception of moving objects in peripheral vision, which may be linked to retrosplenial function in navigation.

Under moderate anaesthesia, the retrosplenial cortex also exhibited subtle orientation tuning in that it preferred cardinal over oblique gratings. Orientation tuning (of individual neurons) in the retrosplenial cortex was also reported in the Murakami, et al. paper, however it was not analysed for preferred responses across the population of all neurons. Human fMRI studies have also observed cardinal orientation bias in scene-selective visual areas but not in the retrosplenial cortex (Nasr & Tootell, 2012). The "oblique bias" has also been reported for the mouse V1 and PM areas (with PM showing stronger bias) (Roth, et al., 2012), suggesting that the retrosplenial cortex may exhibit similar properties.

In mildly-anaesthetised animals, we did not see a consistent pattern of responses to different stimulus orientations which might have resulted from the high variance of the signal.

Taken together, the spatiotemporal tuning properties of the retrosplenial cortex observed under moderate anaesthesia in the current study are consistent with its placement within the dorsal visual stream (**see Chapter 1**).

2.4.4 Alternative analysis methods and the usefulness of intrinsic imaging

The quality and fidelity of intrinsic signals may be improved by the simultaneous recoding at multiple wavelengths, each relating to a different aspect of the signal (Dunn et al., 2005; Yin et al., 2013), with lower wavelengths representing vascular coupling and higher, near-infrared wavelengths being more closely related to tissue oxygenation and light scattering properties (Frostig et al., 1990; Zepeda

et al., 2004). There have also been attempts to isolate meaningful signals from noisy recordings by restricting the time-window of the analysis (Chen-Bee et al., 1996) or employing multivariate analyses (Yokoo, Knight & Sirovich, 2001). A recent development distinguished two further components of signal in the awake mouse: a fast, local signal coupled to cortical activation and a large, slow and diffuse signal showing tight correlation with pupil state, i.e. the alertness of the animal (Pisauro, Benucci & Carandini, 2016).

While a more comprehensive understanding of intrinsic signals coupled with superior analytic tools may further enhance their usefulness for studying cortical activity, ISI has the major limitation of being an indirect method. Paradoxically, it is also ISI's greatest strength due to the similarity with fMRI recordings. Other techniques which successfully capture the dynamic nature of cortical activity include calcium and voltage imaging as well as multi-electrode array systems.

It remains uncertain what exactly is measured by ISI. It has been alternately proposed that observed reflectance changes originate from spiking activity, dendritic potentials or the synaptic release by axonal boutons (Grinvald & Bonhoeffer, online resource). As such, even if intrinsic signals do mirror genuine cortical activity, it is unknown how much reflects local firing, subthreshold events or perhaps incoming inputs. A possible solution to this problem could be for example simultaneous ISI and electrophysiological recordings.

2.4.5 Conclusion

In conclusion, ISI is a useful, however, limited tool for investigating visually-evoked retrosplenial activity.

3 The retrosplenial spatial memory engram

3.1 Introduction

The retrosplenial cortex has attracted much attention due to its proposed involvement in the processes of learning and memory. The following chapter provides evidence for the presence of retrosplenial spatial memory engrams by introducing a novel experimental and analytic approach. It will be argued that the retrosplenial cortex participates in the storage, consolidation and expression of spatial memories via the recruitment of a sparse population of context-sensitive, *c-fos*-expressing neurons. Moreover, it will be suggested that the degree of memory consolidation in the retrosplenial cortex predicts the performance of animals upon long-term memory expression.

3.1.1 What is a memory engram?

In simplest terms, an engram is the biological representation of a memory trace and learning is the process by which an engram is formed. Learning entails lasting, stimulus-driven alterations to the physical and chemical traits of neuronal ensembles, rendering them more likely to (or less likely to) fire upon re-exposure to the stimulus. Crucially, re-exposure to only partial features of the learned stimulus may elicit the re-activation of the entire ensemble (a process referred to as pattern completion), triggering retrieval of the original stimulus representation. Consequently, engram cells and their connections constitute the biological substrate of memory. Exactly how memory engrams arise and evolve remains unknown, however, much progress has recently been made.

3.1.2 The pursuit of the memory engram

While the concept of a biologically-encoded memory engram is not new (Semon, 1921), it required many intricately-designed and technically-advanced studies to be explicitly demonstrated. Early evidence came from brain stimulation experiments on surgical patients in which activating random populations of

temporal lobe neurons sometimes led to the recall of episodic memories (Penfield, W. Rasmussen, 1950). Yet, perhaps, the most famous demonstration of the requirement of specific neuronal ensembles for the expression of memory is the case of patient H.M. who underwent a bilateral medial temporal lobe (MTL) resection as treatment for intractable epilepsy. The surgical procedure resulted in severe episodic memory impairments: complete anterograde amnesia and graded retrograde amnesia while preserving other types of memory such as working-memory and procedural memory (Scoville & Milner, 1957). Although H.M.'s case clearly revealed the importance of the hippocampal formation for certain memory processes, it also hinted at the involvement of other brain sites in the storage of remote episodic memories.

3.1.3 The immediate-early gene *c-fos* as marker for engram cells

Further evidence for the existence of memory engram cells came from studies utilising immediate early genes (IEGs) as markers of neuronal activity. IEGs are a group of genes which are rapidly transcribed upon neuronal activation and whose protein products are thought to mediate long-lasting adaptive changes in the brain. Among them, the proto-oncogene *c-fos* has attracted much attention due to it showing differential patterns of expression under various behavioural paradigms. Physical and psychological stress (Briski & Gillen, 2001), novel environment exploration (Hess, Lynch, & Gall, 1995; Staiger et al., 2002), psychoactive substance administration (Sonia & Pich, 1996), spatial memory tasks (Guzowski, et al., 2001; Vann, et al., 2000), object recognition (Kinnavane, et al., 2014; Powell et al., 2017), classical (Grimm & Tischmeyer, 1997; Swank, 2000) and operant conditioning (Hoz et al., 2017; Svarnik,et al., 2013) as well as exposure to noxious (Bullitt, 1990), visual, tactile, auditory (Guenthner, et al., 2013; Hoz et al., 2017), odorant (Hess & Galllj, 1995; Hess et al., 1995) and gustatory stimuli (Swank, 2000) can all be shown to increase *c-fos* levels at various brain sites.

c-fos participates in the transduction of neuronal activity into gene expression by acting as a transcription factor in association with another protein, c-Jun

(Chiu et al., 1988; Kaczmarek & Chaudhuri, 1997). *c-fos* expression level in the human brain positively correlates with the amplitude and frequency of neuronal discharges (Rakhade et al., 2007). Furthermore, *c-fos* is also calcium-dependent (Ghosh, et al., 1993) and its expression can be enhanced by *N*-methyl-D-aspartate (NMDA) receptor agonists (Berretta, Parthasarathy, & Graybiel, 1997; Liste, Rozas, & Guerra, 1995; Parthasarathy & Graybiel, 1997) and diminished by antagonists (Berretta et al., 1997; Ghosh et al., 1993; Vanhoutte et al., 1999), respectively. For all these reasons, it was hypothesised that *c-fos* may constitute a link between neuronal activation and plasticity and implicated in the process of long-term potentiation (LTP) (Dragunow et al., 1988).

3.1.4 *c-fos* and plasticity

LTP, first described by Bliss and Lomo in 1973, is a model of plasticity, most commonly studied in the hippocampus, where stimulation of the perforant path afferents with brief high-frequency electrical pulses produces enhanced postsynaptic responses. LTP involves at least two stages: early LTP (E-LTP) and late LTP (L-LTP), the first characterised by increased AMPA (α-amino-3-hydroxy-5-methyl-4-isoxazolepropionic acid) receptor exocytosis and new spine formation, the second, by protein-synthesis-dependent stabilisation of the modified spines. The role of LTP in memory was first demonstrated by Richard Morris who showed that NMDA-receptor-antagonist-driven impairment of LTP led to a severe long-term spatial memory deficit (Morris, et al., 1986). Since then, LTP has been widely accepted as one of the fundamental mechanisms of memory. As such, induction of LTP can be thought of as an element of memory engram formation, particularly in the context of spatial learning.

While *in-vivo* induction of LTP via artificial means does elevate *c-fos* levels, the magnitude of LTP and *c-fos* expression do not directly correlate (Dragunow, et al., 1989) and, in some cases, appear to even be anti-correlated (Schreiber, et al., 1991). It has been, however, suggested that whether artificial LTP induction shows a relationship with *c-fos* or not depends on precisely which stimulation protocol is employed (Worley, et al., 1993). Nevertheless, more recently, *c-fos-*

positive engram cells were shown to display some key LTP hallmarks, such as protein-synthesis-dependent increase in excitatory postsynaptic currents (EPSCs) and elevated AMPA/NMDA current ratio (Ryan, et al, 2015).

Further evidence for the link between *c-fos* and memory can be gleaned from experiments with antisense oligonucelotides (ASOs) directed against *c-fos*. Infusion of ASOs *in-vivo* has been shown to impair long-term memory consolidation but not task acquisition or short-term memory on taste aversion, spatiovisual discrimination and fear memory tasks as well as social food-preference transmission (Countryman, Kaban & Colombo, 2007; Grimm et al., 1997; Katche & Medina, 2017; Lamprecht & Dudai, 1996; Morrow et al., 1999; Strekalova et al., 2003). Since some reports support the role of *c-fos* in the acquisition and consolidation but not in the retrieval of memory (Yasoshima, et al., 2006), the specific involvement of *c-fos* in mnemonic processes appears to depend on the task and brain region investigated.

Finally, the requirement of *c-fos* for normal memory is evidenced by *c-fos* knockout mouse lines, which show spatial and associative learning deficits along with LTP impairments at hippocampal synapses (Fleischmann et al., 2003; Paylor, et al., 1994). Interestingly, *c-fos* knockout mice also show reduced levels of integrins (Betts et al., 2002), which are cell-adhesion proteins thought to underlie some aspects of L-LTP, and plasticity in general (Mcgeachie, Cingolani, & Goda, 2011). Due to the apparent importance of *c-fos* for spatial (and other types of) memory, the concept of a memory engram may be simplified to the sum of all neurons exhibiting a specific, context-dependent, *c-fos* expression pattern acquired during learning and manifest upon retrieval. To provide clarity, this definition of a memory engram is employed hereafter.

3.1.5 The use of *c-fos*-targeting transgenic methods in the study of engrams

The utility of *c-fos* as a marker of cellular activity has been demonstrated in studies exploiting its promoter region as a driver of transgene expression.

Engrams can now be directly visualised via genetically-encoded tags (Guenthner et al., 2013; Reijmers et al., 2007) as well as manipulated by employing optogenetic or chemogenetic tools *in-vivo* (Gore et al., 2015; Koya et al., 2009; X Liu, Suh, Pignatelli, & Ryan, 2015; Naoki Matsuo, 2015; Ohkawa et al., 2015; Redondo et al., 2014; Ryan et al., 2015; Tayler, Tanaka, Reijmers, & Wiltgen, 2013).

Partly owing to its simplicity, fear conditioning has emerged as one of the most popular paradigms under which engrams have been studied. Fear-conditioning is a model of associative learning where a stimulus or a context is paired with an aversive stimulus, such as a foot shock, to elicit a conditioned fear response. Remarkably, even a single foot shock can produce a long-lasting fear memory trace (Lux et al., 2016). Fear-conditioning experiments allow for studying many fundamental aspects of memory including encoding, consolidation, retrieval and extinction, and arguably constitute one of the most readily-interpretable behavioural paradigms.

The necessity of engram cells for the expression of fear memory is evidenced by the impairment of retrieval upon optogenetic inhibition of hippocampal engram cells (Tanaka, et al., 2014). The sufficiency of engram cells for the expression of memory, on the other hand, has been shown by direct stimulation of hippocampal engrams resulting in a conditioned response in the absence of the conditioned stimulus (Liu et al., 2012). Furthermore, manipulation of engrams can lead to the assignment of novel emotional valance to an existing memory (Liu et al., 2015; Redondo et al., 2014) or even to the combination of two entirely separate memories (Ohkawa et al., 2015).

The use of *c-fos*-driven transgenes has also been applied to counter deficits seen in mouse disease models. In one study, the effect of chronic stress was shown to be mitigated by the artificial activation of a memory engram associated with a positive experience (Ramirez et al., 2015) while in another study, the amnesic phenotype of APP/PS1 (Alzheimer's precursor protein/presenilin 1)(AD

mice) mice was acutely rescued by the artificial re-activation of the hippocampal fear memory engram while artificial dendritic-remodelling of engram cells provided a lasting rescue (Roy et al., 2016).

3.1.6 Systems-level memory consolidation and the retrosplenial cortex

The hippocampus in not the sole brain region responsible for memory. Instead, it participates in the encoding of memory alongside multiple neocortical and subcortical brain sites (Kitamura et al., 2017; Wheeler et al., 2013). As opposed to the primitive hippocampal circuitry, the six-layered neocortex arguably affords the storage of more complex and more flexibly-retrievable memory traces (Marr, 1971). It is now thought that long-term memory retrieval requires hippocampus-driven extrahippocampal engram activity re-instatement (Fiebig & Lansner, 2014; Santoro & Frankland, 2014). The process of strengthening of the extrahippocampal representation of memory is referred to as systems-level consolidation and, in the case of episodic memory, appears to culminate (after many years) in the formation of fully hippocampus-independent neocortical memory engrams (as seen for example in patient H.M. with graded retrograde amnesia) (Scoville & Milner, 1957). One of the cortical sites displaying evidence of memory engram formation is the retrosplenial cortex.

It has been, for example, shown that conditioned fear-memory is simultaneously encoded by the hippocampus and by the retrosplenial cortex and that inhibition of the hippocampal engram prevents both the re-activation of the retrosplenial engram (without affecting the overall level of retrosplenial activity) and the expression of memory (Tanaka, et al., 2014). Furthermore, artificial activation of the retrosplenial fear-memory engram in the absence of hippocampal activity is sufficient for long-term memory retrieval (Cowansage, et al, 2014). The retrosplenial memory engram also appears to be more stable than the hippocampal (and amygdalar) representations when tested after a long delay (Tayler et al., 2013), highlighting the importance of the retrosplenial cortex for long-term memory storage. Similarly, a time-dependent increase of context-dependent involvement of the retrosplenial cortex was also observed in another

fear-conditioning study employing *Zif268* (another IEG) as driver of EGFP (enhanced GFP) expression (Xie et al., 2014).

3.1.7 The search for the retrosplenial spatial memory engram

Multiple lines of research support the involvement of the retrosplenial cortex in the processing of spatial memory (Vann, Aggleton & Maguire, 2009), however, not much is known about the identity and time-dependence of the retrosplenial spatial memory engram. To date, only a single study has partially addressed this issue by utilising the *c-fos*-based engram tagging methodology (Czajkowski et al., 2014). Tracking *c-fos*-positive cells in anaesthetised mice revealed increased retrosplenial memory involvement upon spatial memory retrieval compared to navigation alone. Moreover, inactivation of the retrosplenial cortex by infusion of the selective AMPA receptor antagonist 6-cyano-7-nitroquinoxaline-2,3-dione (CNQX) reduced the mice' ability to employ an allothetic-cue based navigation strategy. Finally, virally-induced overexpression of the transcription factor CREB in the retrosplenial cortex led to an enhancement of spatial performance, which was abolished by the selective inhibition of CREB-overexpressing cells.

While the Czajkowski, et al. study successfully reveals the involvement of the retrosplenial cortex in the encoding and storage of spatial memory, it does not explicitly demonstrate the existence of a defined retrosplenial memory engram. Moreover, the design of the study could be improved in several ways. To start with, the use of the Morris water maze task may not be desirable in *c-fos*-tag engram studies as it displays sensitivity to animal anxiety levels (Hoelscher, 1999) and also because retrosplenial *c-fos* expression itself increases under stressful conditions (Hsu, et al, 2007). Another issue is that of anaesthesia. While the use of fentanyl/midazolam does not appear to significantly alter *c-fos* levels in the brain (Takayama, Suzuki & Miura, 1994), midazolam was shown to induce amnesic effects on certain tests of memory retrieval (Bustos, Maldonaldo, & Molina, 2009). Furthermore, the high-level expression of a fusion protein containing both *c-fos* and GFP (Barth, Gerkin & Dean, 2004) may have unknown physiological repercussions. Finally, employing a relatively short training

protocol (ten days) with only four imaging sessions may not be sufficient to capture the dynamics and maturation of the cortical memory representation. For all the above reasons, it is apparent that there is still need for further investigation of the retrosplenial spatial memory engram.

3.1.8 Aims of the current study and experimental hypotheses

The motivation for the current study was the search for the retrosplenial spatial memory engram. It was attempted to relate learning on a spatial memory task with changes in the pattern of *c-fos* expression in the retrosplenial cortex. The experimental subjects were transgenic mice expressing enhanced GFP (EGFP) under the control of the *c-fos* gene promoter, developed by the Mayford group (Kim et al., 2015; Liu et al., 2012; Matsuo & Mayford, 2008; Reijmers et al., 2007). Mice received craniotomies over the midline to allow for longitudinal tracking of the *c-fos* engram cells. A spatial task, adapted from Jarrard (1983), was used to test the mice' ability to memorise the arrangement of a maze and the positions of rewards within. Keeping the reward position constant over the course of all sessions allowed for separating the reference memory from the working memory components of the task. Animals were tested on consecutive days during a training phase of the task and then at two later sessions introduced to provide a measure of long-term memory retrieval. While these final two maze re-exposure sessions are referred to as 'retrieval' tests, they did involve reconsolidation of memory as animals were allowed to complete a full session of five trials each time. Nevertheless, for simplicity's sake, the term 'retrieval' is used hereafter. Behavioural sessions were followed by *in-vivo* 2-photon imaging of retrosplenial neuronal ensembles in awake animals. Additionally, three control sessions were interlaced into the study design to provide contrast with the testing sessions. Two negative control sessions involved placement in the dark while a positive control session involved exploration of a novel environment.

It was hypothesised that the spatial memory task would elicit an increase in *c-fos* expression following testing sessions and a comparably lower level of expression during negative control sessions while a positive control session

58

(novel environment exploration) would lead to the highest level of *c-fos* activity. Further, it was hypothesised that the *c-fos* expression pattern would exhibit gradual stabilisation over the course of training, that it would remain stable when tested at retrieval sessions and that it would show little similarity with the pattern induced by control sessions. Finally, it was hypothesised that the consolidation of the memory engram, as measured by the stability of the *c-fos* expression pattern, would show an inverse relationship with the number of reference memory errors made during retrieval of remote memory.

3.2   Methods

3.2.1 The experimental mouse line

The animals in the study were B6.Cg-Tg(Fos-tTA,Fos-EGFP) mice derived from two breeding pairs received from a collaborator (Stéphane Baudouin) who had himself obtained his line from The Jackson Laboratory (JAX stock #018306). The line carry two independent Fos-tTA and Fos-EGFP transgenes which allow for the detection of fluorescence in *c-fos*-positive neurons as well as for the conditional expression of a gene-of-interest in the same cells, respectively. More specifically, the Fos-EGFP transgene drives the expression of a short half-life (2 hours) green fluorescent protein (shEGFP) in *c-fos*-positive neurons (Kim et al., 2015). Conditional expression of an exogenous gene was not utilised in the current study.

The mouse colony was established with two hemizygous females and two wild-type males (C57/BL6). The first generation (F1) of offspring for both breeding pairs were genotyped for the detection of the EGFP gene using the supplier's PCR protocol and hemizygous carriers were further outbred with wild-type mice to yield the F2 generation. Hemizygous F2 mice were then crossed across the two linages to produce litters with a higher likelihood of carrying the desired allele, which, following genotyping, were employed in the study.

3.2.2 Experimental subjects

Seven adult mice (6 male) took part in the experimental protocol; they were 8-10 weeks old at the time of surgery. The animals were housed with their littermates under a 14h/10h dark-light cycle and food and water were available *ad libitum* (except for during behavioural testing, see below). Each cage contained a UFO hamster wheel (Pets At Home, Handforth, UK). The craniotomy procedure was identical to that described in **Chapter 2** except that the cranial windows were round with a 3 mm radius and 0.4 mm thick (Harvard Apparatus

Ltd, UK). Following surgery, mice were re-united with their littermates and allowed to recover.

3.2.3 Radial-arm maze apparatus

The central platform of the radial maze was a regular wooden octagon with 8 wooden arms attached, each measuring 9 by 36 cm. The walls of the arms were made of clear Perspex panels 17 cm high. The joining of the maze was made of black 3D-printed components. Each arm was separated from the central platform by an upside-down guillotine door (made of clear Perspex) pulled close via strings threaded through an arrangement of pulleys mounted to the underside of the platform. In this way, the experimenter could control access to the individual arms. At the end of each arm there was mounted a black 3D-printed element containing a 50 µL reward well. There were also numbered 3D-printed plaques atop each of the outermost arm walls to aid arm identification. The maze was elevated at 100 cm above ground and evenly illuminated by ambient light. The position of the maze remained fixed throughout the study. The maze was situated in the corner of a room that contained various furniture items and laboratory equipment.

3.2.4 Behavioural Procedure

Figure 3.2.1 depicts the progression of stages in the study with reference to the first day of radial-arm training (day 1). Following surgery, animals were habituated to the experimental procedures in 4 stages: habituation to handling (days -20 to -16), habituation to head-fixation (days -15 to 10), habituation to imaging (days-9 to -6), and finally, habituation to the radial-arm maze (days -5 to day -3). There were two additional days of habituation to imaging (days -2 to -1) before training in the maze commenced. Radial-arm maze training lasted nineteen days. Two negative control sessions were carried out on days 22 and 40 and a positive control session, novel environment exploration, was carried out on day 28. The retrieval of memory acquired during radial-arm maze training was tested on days 25 and 43. The mice were imaged on the last day of maze

habituation (day -3), seven out of the nineteen radial-arm maze sessions (days 1, 4, 7, 10, 13, 16, 19), the two negative (days 22 and 40) and positive (day 28) control sessions and on the two retrieval sessions (days 25 and 43). Animals were also subject to the habituation to imaging procedure for two days prior to any imaging session (including during the radial-arm maze training stage). Finally, the mice were sacrificed following imaging on day 43.
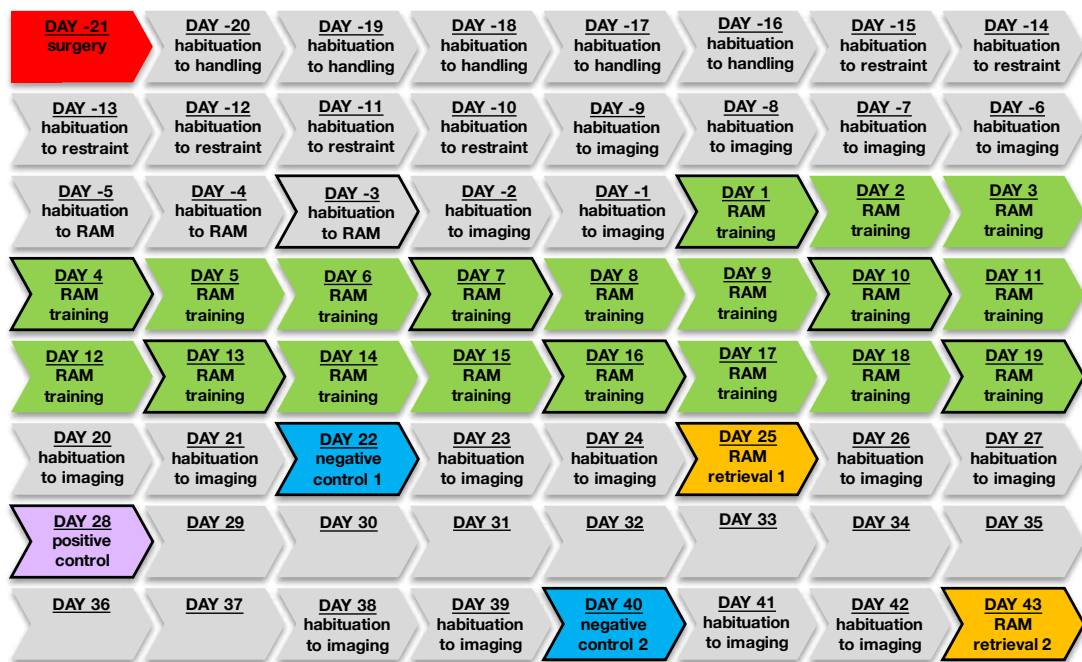
Figure 3.2.1. The overview of the experimental schedule. Each element of the flowchart represents one experimental day numbered with reference to the first day of radial-arm maze (RAM) training (day 1). Imaging sessions are indicated by the outlined elements.

3.2.5 Habituation

The first stage of habituation lasted five days and simply involved handling the animals during daily post-operative care. Over the next six days, mice were gradually habituated to head-fixation by being immobilised for short intervals (1-5 min) with the use of forceps. Following this, the mice were introduced to the 2-photon imaging set-up. Mice were head-fixed and placed on top of a UFO hamster wheel (mounted beneath the microscope objective), in the darkness, for 10 min. The same procedure was repeated on the three following days with running durations of 45 min, 60 min and 60 min. The level of animal stress was

qualitatively assessed by monitoring the number of faecal boli produced on each session (Moennikes, H., Schmidt, B. G. & Tache, Y., 1993), which showed a marked reduction over the course of the habituation sessions. Immediately before and after running on the wheel, each mouse was placed in its individual 'experimental cage' in the dark for 30 minutes. The 'experimental cage' was a standard small rodent cage with standard bedding but without access to food or water.

Next, the mice were habituated to the radial-arm maze where they were allowed to freely explore for 30 minutes (all arms open). While in the maze, animals were also exposed to strawberry milk (Yazoo, FrieslandCampina, The Netherlands) for the first time. On the first day of maze habituation, strawberry milk droplets were evenly scattered around the maze and inside the reward wells at the end of each arm. On subsequent days, the number of strawberry milk droplets was gradually reduced such that on the final habituation day, rewards were only present inside and immediately around the reward wells. Following the three days of maze habituation, all mice were given two further days of exposure to imaging procedures.

The animals' liquid intake was reduced at this stage of the study. Each mouse was allowed as many strawberry milk droplets as were available on a given day and was further supplemented with water up to a volume of 1 mL of total daily liquid intake. Water was made available only after all experimental procedures on a given day were completed.

3.2.6 Radial-arm maze training

Mice were subsequently trained on a reference memory task in the radial-arm maze. The animals' task in the radial-arm maze was to retrieve four strawberry milk rewards located in reward wells at the end of four out of the eight arms. The rewarded arms (arm numbers 2, 3, 4 and 8) were consistent across training and across animals. Each testing day consisted of five trials. At the start of each trial, the animal was placed under a cardboard box on the central platform of the

maze. The box was lifted and after a delay of 10 seconds, the arm doors were open. The animal was allowed to visit any of the arms to look for rewards. Arm visits were manually recorded for each trial. Upon return to the central platform, the guillotine doors were closed again for 10 seconds until the next run began. In total, animals were allowed either up to eight attempts or up to 5 minutes to retrieve all four rewards. The trial also ended if the animal successfully retrieved all four rewards before eight attempts had been made. The mice were confined to the central platform underneath a cardboard box in-between the trials while the experimenter wiped the maze with 70% ethanol and replenished the consumed rewards. In total, an experimental session lasted up to 30 minutes (5 x 5 minutes for each trial plus 5 minutes for cleaning/replenishing rewards). The mice were placed in their 'experimental cage' in the dark for 30 minutes prior to testing and returned to the 'experimental cage' after testing was over. Training on the radial-arm maze task lasted for nineteen consecutive days.

3.2.7 Negative control condition

The mice underwent two negative control sessions (on day 22 and day 40). Under the negative control condition, mice first spent 30 minutes in the 'experimental cage' as they would before the radial-arm testing sessions. They were then briefly handled and returned to the 'experimental cage' together with a plastic weighing boat filled with 20 droplets of strawberry milk (equivalent to the maximum reward available on testing days) for a further 30 minutes in the dark. Finally, the weighing boat was removed, the mice handled briefly again and returned to the 'experimental cage'.

3.2.8 Positive control condition (novel environment exploration)

For the novel environment exposure session (day 28), mice first spent 30 minutes in the 'experimental cage' in the dark, as under the testing and negative control conditions. After that, they were transferred to a white Styrofoam box equipped with various visual, tactile and odorant stimuli (Figure 3.2.2). The interior dimensions of the box were 26 by 31 by 26 cm. The box contained two

explorable levels: the floor level and a raised platform accessible via a ramp. The ramp was a smooth black plastic bar with an affixed ribbed rubber band to provide grip. The floor and the walls of the box were covered with black and white geometric patterns. The box also contained movable small weighing boats (on its floor and attached to the wall), a plastic string suspended between two of the walls, two glass electrode filaments mounted against the walls (Harvard Apparatus Ltd, Cambridge, UK) and two dental cotton rolls (one on the floor, one on the wall) infused with vanilla and lemon extracts (FoodCare, Poland) respectively. Finally, the box also contained four reward wells moved from the radial-arm maze: three on the ground level and one on the level of the raised platform.

Figure 3.2.2. A photograph of the novelty condition (positive control) environment. The picture shows a mouse on the ground floor of the two-level novelty chamber.

Mice were placed in the box five times for 5 minutes, mimicking the five test trials on radial-arm maze sessions, and were provided with strawberry milk in the four reward wells on each run. They were confined under a cardboard box in-between runs. Following the procedure, animals were returned to their 'experimental cages'.

3.2.9 Regions of interest for 2-photon imaging

The regions of interest (ROIs) for imaging were chosen based on the appearance of the cortex under brightfield illumination and then refined based on the visibility of fluorescence under the 2-photon microscope. Brightfield images were collected on day -5 (the first day of radial-arm maze habituation) under the ISI set-up (described in **Chapter 2 Methods section**). This helped to identify areas devoid of large blood vessels and post-surgery debris such as dental cement as well as revealed a set of landmarks useful in ROI re-alignment. On the same day, mice were also briefly imaged under the 2-photon microscope to identify a region displaying the best quality of fluorescence and possibly the greatest number of visible neurons. After a region had been selected, another brightfield photo of the pial surface was taken under the 2-photon set-up to aid the re-alignment of the ROI on subsequent days.

Following animal perfusion on day 43 of the study, another set of images was taken to assess the position of the cranial window in relation to gross anatomical landmarks. This allowed for the subsequent alignment of the 2-photon, ISI and post-mortem brightfield images and made it possible to mark the precise position of the imaging ROI for each animal.

3.2.10 The 2-photon set-up

Mice were imaged under a custom-built 2-photon microscope (MOM, Sutter Instruments, USA) with a Ti:Sapphire laser (MaiTai DeepSee, Newport SpectraPhysics, UK) using a 20×, 1.00 NA Olympus (N20X-PFH) water immersion objective. During imaging, mice were placed on top of a UFO hamster wheel and head-fixed. The design of the wheel allowed the mice to decide whether they wanted to remain stationary or to move and thus helped to minimise stress. Imaging was performed in the dark with the set-up tightly covered with a black opaque curtain. The laser was tuned to 940 nm and maintained within the power range of 35.0-35.3 mW.

3.2.11 The timeline of imaging

Imaging began exactly 90 minutes from the time of radial-arm maze entry or start of the control conditions. The imaging timeline therefore consisted of the following stages: 30 minutes in the dark in the 'experimental cage' (1), radial-arm maze testing/control session lasting up to 30 minutes (2), return to the 'experimental cage' until 60 minutes from the beginning of stage 2 had elapsed (3), placement under the 2-photon microscope and the alignment of the region of interest with reference (4) and, finally, at precisely 90 minutes from the onset of stage 2, imaging. Fluorescent images were taken for 2 hours at 15 minute intervals (90 mins, 105 mins, 120 mins, 135 min, 150 min, 165 min, 180 min, 195 min). Following imaging, mice were returned to their cages and given water if they have not already consumed 1 mL of liquid that day. The imaging schedule is summarised in Figure 3.2.3 below.

Figure 3.2.3. The timeline of the imaging procedure. The experimental schedule involved five stages culminating in imaging starting at 90 minutes following the beginning of radial-arm maze (RAM) testing or control.

3.2.12 Imaging parameters

At each imaging timepoint, a stack of 70 16-bit images was acquired. The stack was of the following dimensions: 400×400 µm wide (corresponding to 1024×1024 pixels) and 140 µm deep (70 pixels). The z-position of the first image in the stack lay between 100-130 µm under the pial surface, corresponding to the outer border of cortical layer 2. The acquisition of each stack lasted around 8 minutes and mice were left undisturbed in-between the imaging timepoints unless the objective water required topping-up.

3.2.13 Perfusion of the animals

Immediately after imaging on day 43, mice were terminally anaesthetised with a 1 mL intraperitoneal injection of sodium pentobarbitone (Euthathal; Merial Animal Health, UK). They were then intracardially perfused with a solution of 1% paraformaldehyde/PBS and stored in the fixative at 4°C until cut. Brains were incubated in 25% sucrose in PBS overnight prior to cutting and sliced in the coronal plane at 30 μm with a sliding microtome (Jung SM, Leica, Germany), followed by cryopreservation in a glycol/sucrose solution at -20°.

3.2.14 Immunohistochemistry for the detection of *c-fos* and EGFP

For each animal a 1:4 series of brain slices was processed for the detection of *c-fos*, EGFP and NeuN. The slices were first thoroughly rinsed in PBS solution (Oxoid, UK)(first overnight and then 4×15 minutes) and then incubated in blocking solution (PBST: 0.3% Triton-X in PBS (Fisher Scientific UK Ltd, UK) and 2% normal goat serum (Merck, Germany)) for 1 hour. After that, they were transferred into the first primary antibody cocktail containing a 1:5,000 concentration of rabbit anti-*c-fos* polyclonal antibody (Synaptic Systems GmBH, Germany) in the blocking solution at 4°C for 72 hours. The slices were then washed 4×15 minutes in PBST and incubated in a solution of 1:1,000 goat anti-rabbit AlexaFluor-405-IgG antibody (Abcam, UK) in the blocking solution for 2 hours at room temperature. The slices were then again washed 4×15 minutes in PBST and incubated in the second primary antibody cocktail. This was a solution of 1:2,500 rabbit anti-NeuN-AlexaFluor647 (Abcam, UK) and 1:2,500 rabbit anti-GFP-AlexaFluor488 (Fisher Scientific UK Ltd, UK) monoclonal antibodies in the blocking solution. The incubation was again at 4°C and over 72 hours, after which the slices were washed 4×15 minutes in PBST and mounted on gelatine-coated glass slides (Fisher Scientific UK Ltd, UK). The slices were protected with an aqueous mountant solution (Fluoromount; Merck, Germany) and a glass coverslip (Fisher Scientific UK Ltd, UK) and sealed with nail varnish (Dazzle Nail Polish; USA).

3.2.15 Imaging of the fixed tissue

Brain slices were imaged under a Zeiss LSM 880 upright confocal microscope with Airyscan equipped with a Plan Apochromat 20×/0.8 air objective (Zeiss, Germany). NeuN, *c-fos* and EGFP were detected with the HeNe 594 nm, Diode 405 nm and Argon multi-line 458/488/514 nm laser lines, respectively. The wavelength filtering was set to default software values indicated for the imaged fluorophores. The images were stitched in Fiji and lightly filtered (2D anisotropic diffusion, 20 iterations), followed by background subtraction.

3.2.16 Analysis of performance on the radial-arm maze task

Learning of the spatial task was assayed by tracking the mean number of errors per session. Total errors were split into two categories to reveal the working-memory (WM) and reference memory (RM) components of the task. A WM error was defined as re-entry into an arm previously visited during the trial whilst an RM error occurred when the animal visited a non-baited arm (that is arms 1, 4, 5 and 7).

3.2.17 Pre-processing of 2-photon image stacks

The pre-processing of image stacks was carried out in a semi-automated way in Fiji (Schindelin et al., 2012) and is summarised in Figure 3.2.4**.** The first step involved indexing of files from across all animals and all conditions. Then, the xy drift along the z axis was corrected with the StackReg plugin (Rigid Registration, (Thevenaz, Ruttimann & Unser, 1998)) for each stack. At this stage, images were also lightly filtered (Kuwahara filter, sampling = 3; followed by median, radius = 2). The next step involved precise manual alignment of stacks across days in the z axis as well as a coarse alignment in the xy plane. All stacks were then truncated to only include the 60 best overlapping z planes. This was followed by the reduction of the z dimensionality from 60 images to 12 images per stack. In this way, each image in a stack now corresponded to 10 µm in the z axis. The reduction in dimensionality was carried out by first filtering the images using the built-in 3D Gaussian filter (x, y, z = 2) and then obtaining maximum intensity projection images for every 5 images in the stack.

The next stage involved pooling together all corresponding z planes from stacks across the days and timepoints and creating 12 superstacks of 104 images (8 timepoints×13 sessions) for each animal. These were then aligned in the xy plane using the StackReg (Rigid Registration) and Template Matching (default parameters)(Tseng et al., 2011) plugins. The next step utilised the bUnwarpJ plugin (Sorzano, Thévenaz, & Unser, 2005) to correct for non-linear distortions in the xy plane. First, the histograms of all images in the superstack were equalised by using the Bleach Correction (Histogram Matching) option from the Adjust menu. Then, from each superstack, a reference image was created by running a maximum intensity projection and used as template for the bUnwarpJ transformations. The transformations were run iteratively starting with coarse parameters (Registration mode: Accurate; Initial Deformation: Coarse; Final Deformation: Fine, remaining parameters: default) and progressing to finer parameters (Registration mode: Accurate; Initial Deformation: Fine; Final Deformation: Very Fine, remaining parameters: default). The resulting images were then manually cropped to only include a ROI region with non-NaN pixels and maximum intensity projections of these images were combined into a stack for each case. These were then aligned using the Template Matching plugin and cropped to exclude NaN pixels. The x and y translation values from the Template Matching plugin were manually inputted to translate stacks 1-12 for each animal which were further cropped to display the same xy dimensions across all 12 stacks.

3.2.18 Detection of fluorescent cells

The 12 cropped and aligned superstacks were then combined using the montaging option. For each animal, a montage of all images from across all stack levels and conditions was created such that it consisted of 104 rows (temporal order of images) and 12 columns (the 12 z levels). These were then turned into a single stack of 1248 images and their histograms were equalised across the stack (Adjust->Bleach Correction->Histogram Matching). The stack was then converted into a new stack of 104 images, each containing the 12 z

levels in a row and saved for further analysis (measurement stack). A standard deviation image projection was carried out on the measurement stack.
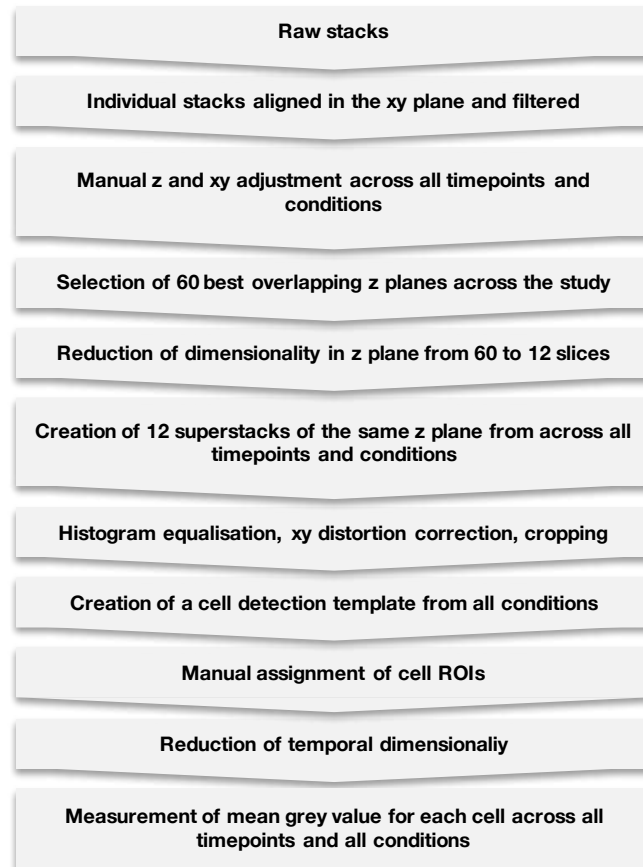
Figure 3.2.4. A flowchart of processing steps in the analysis of fluorescent image stacks.

The standard deviation projection was used for the masking of fluorescent cells. For each identified neuron, the z plane with the largest cross-section was sought and a round (7 μm radius) ROI mask was assigned to it at that position. The temporal dimensionality of the measurement stack was then reduced. For each pair of adjacent timepoints (e.g. 90 min and 105 min, 120 min and 135 min), a mean stack was created and filtered with a Gaussian filter (x,y=2). From this point onward, the following timepoints were used: (1) : 90 min to 120 min; (2), 120 min to 150 min;, (3),150 min to 180 min; and (4) 180 min to 210 min. The ROI masks were then applied throughout the stack so that a mean grey value per timepoint and condition could be measured.

3.2.19 Analysis of fluorescence and cell numbers

The cell density was calculated by dividing the number of detected cells by the volume of tissue present in the final measurement stack for each animal and expressed as number of cells per mm^3.

Cell fluorescence values were measured on an 8-bit scale and used in this format for analyses. The change in fluorescence during an experimental session was calculated by subtracting the fluorescence intensity at timepoint 1 from the value at timepoint 4 for every cell. Values calculated across sessions were pooled to derive a single standard deviation measure for each animal. A cell was considered 'active' if its change in fluorescence value was positive and exceeded 1.5 times the standard deviation of the pooled distribution of fluorescence change for each animal. The 'percentage' active cells index was calculated by dividing the number of 'active' cells on a given session by the total number of detected cells for each animal and multiplying it by 100.

The analysis of the timecourse of fluorescence in the total cell pool and the 'active' and 'inactive' cell pools was conducted with normalised values (z-scores) due to large differences in the absolute fluorescence intensity values measured.

For certain analyses, values were collapsed across a number of sessions by taking an arithmetic mean (such as for the radial-arm maze days 1-19, which were collapsed into a single experimental block: 'training').

3.2.20 The calculation of the Jaccard index and hierarchical clustering

The Jaccard index (**J**) was calculated for each pair of conditions based on the following equation: $J = \dfrac{c}{a+b-c}$ where **c** represents the number of cells which 'co-activated' between session n and n+1, **a** represents the number of 'active' cells in session n and **b** represents the number of 'active' cells in session n+1.

Heatmaps for individual animals were created in Microsoft Excel by applying conditional formatting with the same parameters across all animals (the colour scale is the same across cases). A compound Jaccard index heatmap was calculated by taking the arithmetic means of Jaccard values across cases and it was presented along with the standard error of the calculated means.

A dendrogram revealing the clustering of conditions was derived by using the 'Hierarchical Cluster Analysis' function in SPSS executed via the Syntax Editor window. The input data were the mean Jaccard indices and the cluster method chosen was 'between-group linkage'. For display purposes, the cut-off 'rescale distance combine' value was set at 20/25 (meaning that clusters with similarity distance lower than 20/25 were not considered as clusters).

3.2.21 Calculation of Jaccard index *p*-values

The probabilities of the occurrence of Jaccard values by chance were calculated in RStudio 2 (version 1.0.153). The probability of the occurrence of a Jaccard value (P_J) for the set of inputs *a* (number of cells 'active' on session n), *b* (number of cells 'active' on session n+1), *c* (number of cells 'co-active' on sessions n and n+1) and *t* (number of cells in the 'active cell pool') was derived from the following equation:

$$P_J = \frac{C_c^a * C_{b-c}^{t-a}}{C_b^t},$$

where *a*, *b* and *t* are fixed parameters associated with each observed Jaccard index and *c* is a hypothetical value sampled from the set of all its possible values: <0, min(*a*,*b*)). C_c^a represents all possible unique arrangements of overlapping cells among all cells which activated on session n. C_{b-c}^{t-a} represents all possible unique arrangements of active cells on session n+1 which did not

overlap with session n. C_b^t represents all possible unique arrangements of active cells on session n+1 unrestricted by the overlap term **c**.

The obtained values were then expressed in the form of a probability distribution function and the probability of the observed Jaccard index being greater than the chance Jaccard values was calculated. This was done by subtracting from 1 the sum of the probabilities of all chance Jaccard indices ≤ observed Jaccard index. The calculated *p*-value therefore represents the probability of the observed Jaccard index being greater than all the possible Jaccard indices for a given **a**, **b** and **t**. The family-wise multiple-comparison error was corrected for using the Bonferroni adjustment for each animal. Finally, compound *p*-values across all animals for each pair of conditions were calculated by employing Fisher's method in RStudio 2 ('metap' package).

3.2.22 Relationship between Jaccard index and performance at task re-exposure

The relationship between Jaccard index and memory performance at task re-exposure was calculated by feeding four variables into a partial correlation in SPSS. Two confounding variables were controlled for: the mean Jaccard index per animal (calculated as the mean of all Jaccard values for each heat map) and Jaccard index between session C2 and R1. The correlated variables were the Jaccard index between sessions R2 and R1 and the RM error ratio between session R2 and session R1.

3.2.23 Statistical analyses and figures

The comparisons of behavioural scores, fluorescence values and the percentage of 'active' cells were performed in SPSS (IBM, Armonk, USA) using the repeated-measures general linear model function while Jaccard index probability was modelled in RStudio2 (described above). Violations of sphericity were corrected for with the Greenhouse-Geisser adjustment of degrees of freedom. The family-

wise error for multiple comparisons was corrected for by employing the Bonferroni adjustment of p-values. For all tests, the null hypothesis was rejected for $p < 0.05$.

3.3   Results

3.3.1 Positioning of regions of interest

All ROIs were found to be confined to the anterior two-thirds of the retrosplenial cortex and were located within 0.35-2 mm anterior from lambda. All ROIs also lay within the mediolateral boundaries of the dysgranular retrosplenial cortex (Figure 3.3.1).
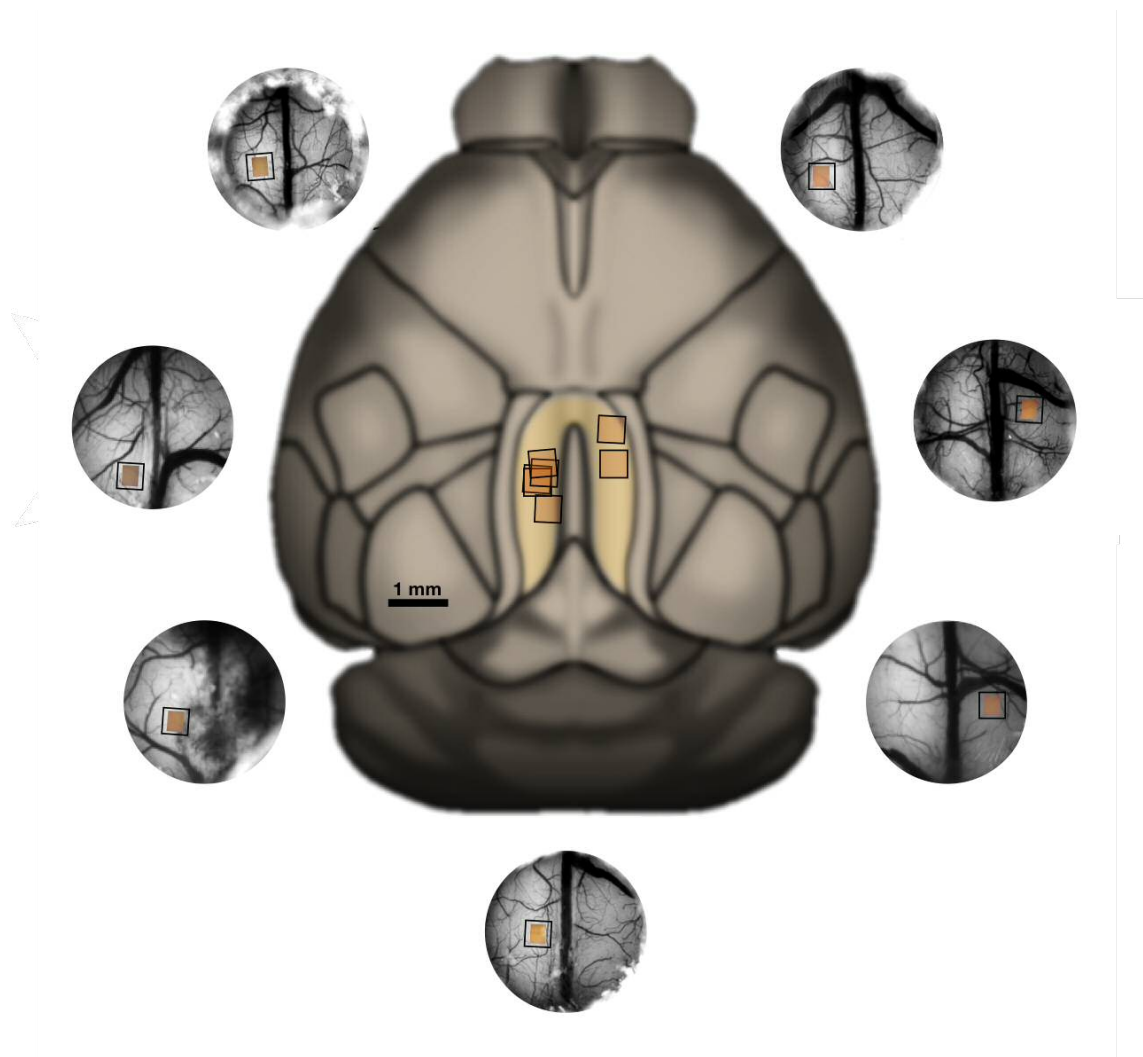
Figure 3.3.1. The location of regions of interest (ROIs) for the seven animals in the study. The round pictures are wide-field images of cranial windows with superimposed ROIs captured under the 2-photon set-up. The central image is a mouse brain template based on the Allen Institute Brain Explorer 2 tool with superimposed ROIs over the dysgranular retrosplenial cortex (highlighted in yellow).

3.3.2 Immunohistochemical confirmation of *c-fos* and EGFP co-localisation

The expression of *c-fos* in EGFP-positive neurons was examined by means of immunohistochemistry (Figure 3.3.2). A qualitative assessment revealed that *c-fos*-positive cells constituted a large proportion of all NeuN-positive cells and that EGFP-positive cells were a subset of NeuN+*c-fos*+ cells. Crucially, no *c-fos*-negative EGFP-positive cells were detected. The highest density of triple-positive cells was observed in layer 2/3 of the dysgranular RSC, the region targeted in the in-vivo experiments. Quantitative assessment of signal co-localisation is pending.
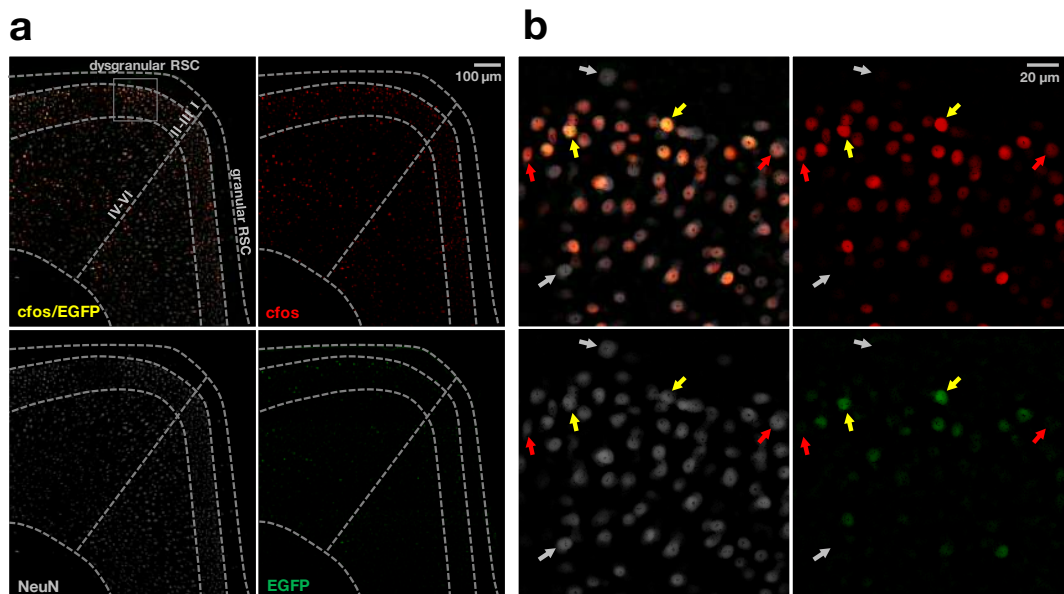
Figure 3.3.2. Fluorescence staining for NeuN, cfos and EGFP. Panel a displays an image of the stained retrosplenial cortex and panel b shows a magnified area of panel a (indicated by a grey square). The colours used are all pseudocolours with grey showing all detected neurons (NeuN), red showing cfos-positive cells and green showing EGFP-positive cells. The arrows in panel b denote three categories of identified neurons: grey – NeuN+cfos− EGFP−, red – NeuN+cfos+EGFP− and yellow – NeuN+cfos+EGFP+.

3.3.3 Performance on the radial-arm maze task

The animals showed an overall improvement in performance over the nineteen days of training with a mean decrease in total errors of 56±9% (F(18, 108) = 7.64,

p < 0.001) (Figure 3.3.3). This improvement was particularly evident when only reference-memory errors were considered, revealing a mean error decrease of 82±4% from 3.42±0.28 to 0.60±0.15 (F(18, 108) = 18.58, p < 0.001). Conversely, working-memory errors remained at a constant level with a mean decrease of 31±14%, which was not statistically significant (F(18, 108 < 1, p > 0.05).

Next, the performance on retrieval sessions one (R1) and two (R2) was compared with the scores on the final day of training (19). While total errors did not significantly change (F(2, 12) = 2.34, p > 0.05), a significant increase in reference-memory errors was observed (F(2, 12) = 4.98, p = 0.027), revealing forgetting. Finally, the level of working-memory errors remained unchanged between training and retrieval (F(2, 12) < 1, p > 0.05).
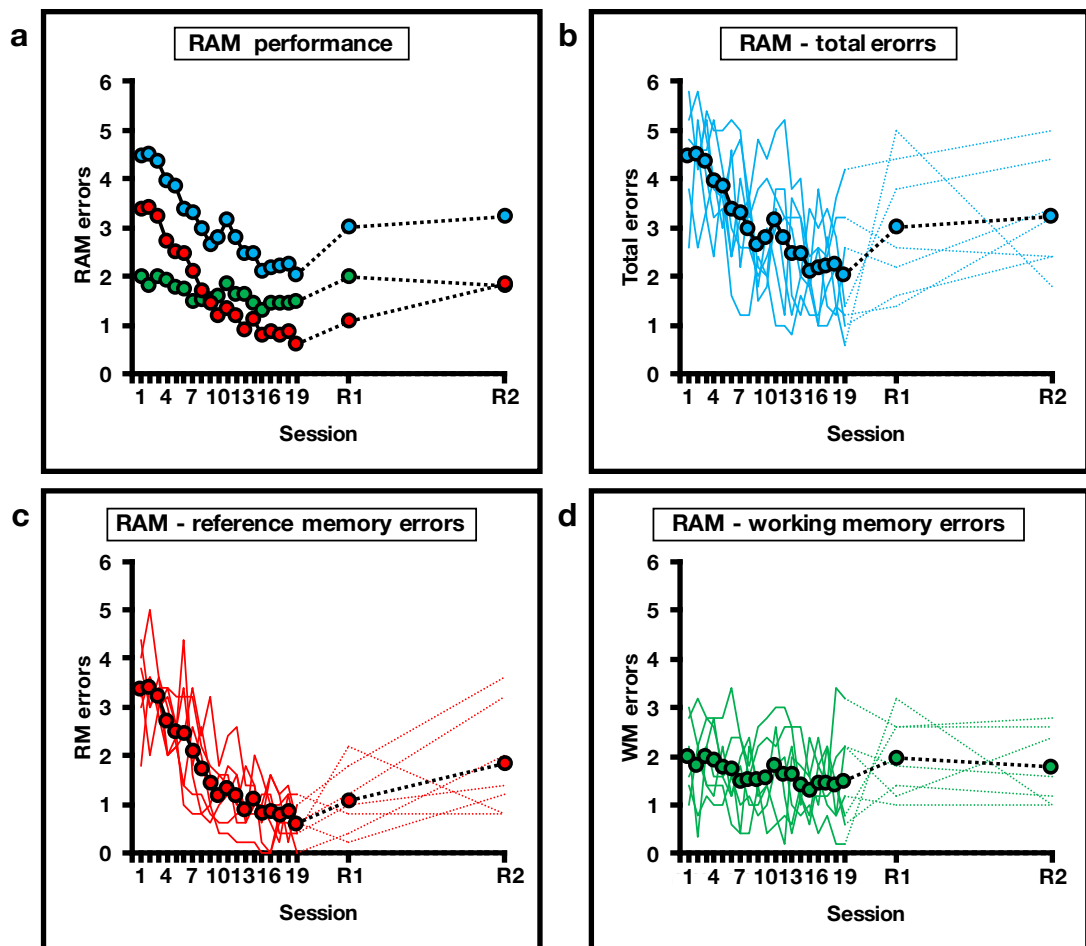
Figure 3.3.3. Performance on the modified radial-arm maze (RAM) task. Panel a displays the mean values for total (blue), reference-memory (RM, red) and working-memory (WM,

3.3.4 The characteristics of EGFP-positive cells *in-vivo*

A total of 5,584 EGFP-positive cells were detected across all animals in the study. Importantly, following the pre-processing spatial transformations of the raw images, it was possible to track the same cells throughout all experimental conditions (Figure 3.3.4). The mean density of fluorescent cells reached 9.23×10^4 cells/mm^3 (range $7.69\text{-}11.93 \times 10^4$) consistent with previously reported estimates for neuronal cell density in layer 2/3 of the mouse brain (Schuz & Palm, 1989). It is therefore plausible that the cell detection protocol employed in this study captured virtually all cells that were available for detection.
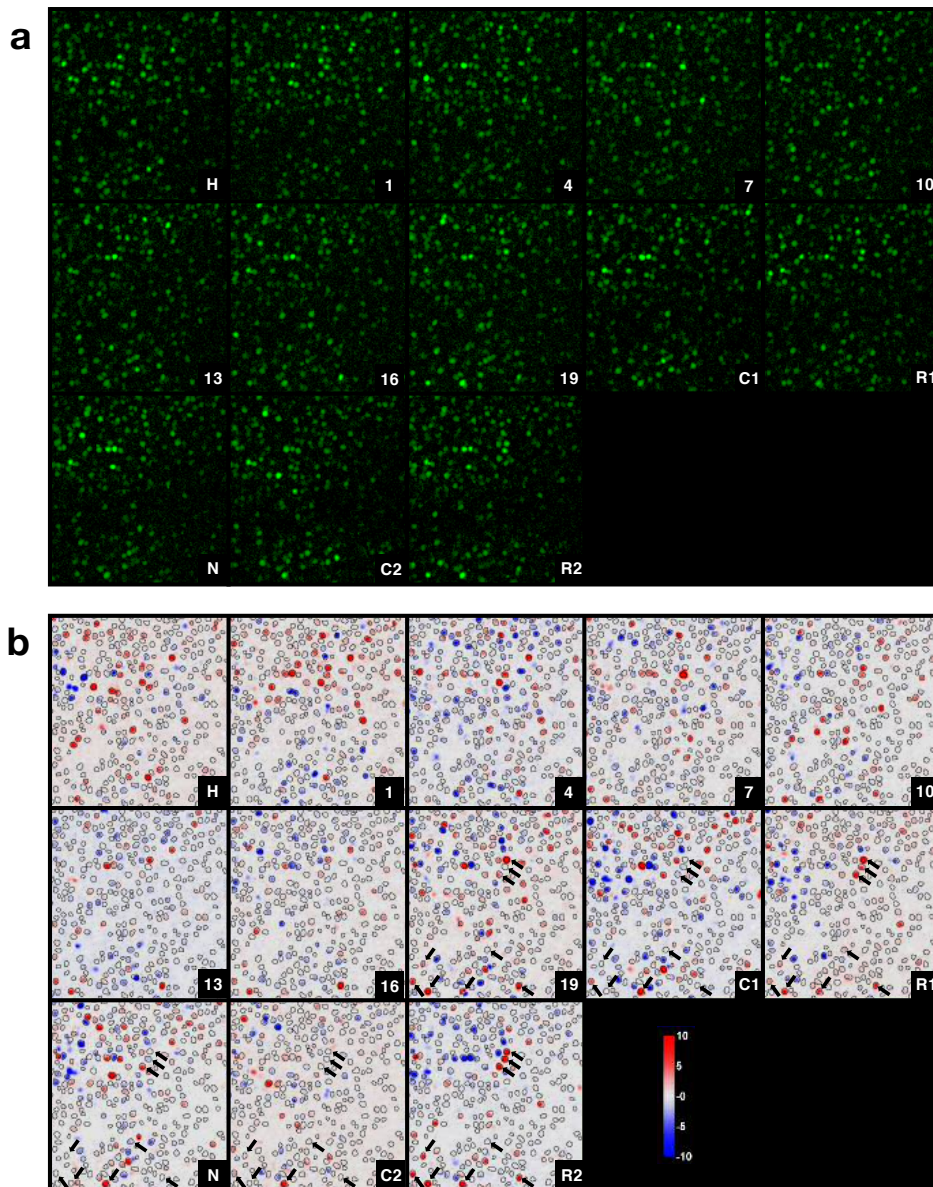
Figure 3.3.4. The appearance of fluorescence and the change in fluorescence for a representative z-stack level. Panel a displays the same z-stack level across all thirteen imaging sessions following all image pre-processing stages. Panel b displays the change in fluorescence values (timepoint 4 minus timepoint 1) for the same z-stack level as in a. The black outlines were added to aid the identification of detectable cells. Black arrows point to a subset of cells which show a condition-dependent pattern of activity. The calibration bar shows the change in fluorescence value scale. H – habituation, 1-19 – radial-arm maze training sessions, C1 – negative control session 1, R1 – retrieval session 1, N – novelty session (positive control), C2 – negative control session 2, R2 – retrieval session 2.

Individual cells presented as evenly-sized spheroids (distended in the z-plane) with a uniform fluorescent fill, save for a small dark punctum near the centroid of each cell, most likely the nucleolus (Figure 3.3.4). The signal-to-noise ratio (cell fluorescence versus background) visibly differed between animals,

presumably due to varying levels of window quality and/or the imaging angle. Nevertheless, the overall characteristics of the distribution of cell fluorescence intensity values were consistent across the mice. In each case, cell values assumed a unimodal, strongly-positively skewed distribution (Figure 3.3.5a). As such, it was not possible to unequivocally designate any cell 'active' or 'inactive' and an alternative strategy was explored.

Since previous publications (Y. Kim et al., 2015) reported an overall time-dependent, task-induced, fluorescence increase in fixed, EGFP-expressing cells, it was also investigated in the current study. In contrast to what has been reported using fixed tissue, however, cell fluorescence intensity showed a relationship with neither time ($F_{timepoint}(3,18) < 1$, $p > 0.5$) nor experimental condition ($F_{condition}(3.45, 20.72) = 2.91$, $p = 0.053$)(Figure 3.3.5c).

Due to the lack of global changes in fluorescence, it was next asked whether there existed a separate sub-population of cells exhibiting a time-dependent fluorescence intensity increase. For each cell, the difference in fluorescence intensity was taken between the last and the first imaging timepoints and plotted on a frequency histogram (described in Methods). The resulting frequency distribution of the calculated values assumed a largely symmetrical double-exponential shape with a mode around 0 (Figure 3.3.5b) for each animal and under any of the experimental conditions. In other words, the vast majority of the cells were seen to show relatively minor departures from baseline while a minority of the cells showed both positive and negative fluorescence changes. Since a decrease in fluorescence is unlikely to constitute a biologically-meaningful signal (see discussion below), the focus was placed on the cells displaying increased intensity values.

Considering the lack of an obvious dichotomy among the cells exhibiting positive fluorescence changes, an arbitrary threshold of 1.5 × the standard deviation of the distribution (see Methods for clarification) was posited to reveal the properties of the cells with the highest levels of activity. Each cell designated

as 'active' at least once upon any of the thirteen imaging days was placed in the 'active cell pool'. Together, 'active' cells constituted 27% of all detected cells (range 20-32% of all cells per animal (Table 3.3.1).

Table 3.3.1. Numbers of all detected cells and the 'active' cells among them.

CASE	CELLS DETECTED	'ACTIVE' CELLS (% ALL)
1	564	140 (25%)
2	727	195 (27%)
3	634	138 (22%)
4	872	175 (20%)
5	925	246 (27%)
6	1162	382 (33%)
7	701	227 (32%)
SUM	5,584	1,503 (27%)

The arbitrary fluorescence cut-off point therefore identified cells which showed a large fluorescence increase between the first timepoint and the last timepoint. It did not, however, necessarily presuppose the overall shape of the time-fluorescence relationship. Plotting change in fluorescence for the 'active' and 'inactive' cell pools showed largely linear and inverse patterns of time-dependency (Figure 3.3.5d) with an overall increase and decrease, respectively. Furthermore, 'active' cells displayed a timepoint × condition interaction ($F_{interaction}(4.86, 29.17) = 3.51$, $p = 0.014$) while 'inactive' cells showed the main effects of time ($F_{timepoint}(3, 18) = 192.43$, $p < 0.001$) and condition ($F(3.12, 18.72) = 3.52$, $p = 0.034$) but no interaction ($F_{interaction}(3.87, 23.25) = 1.58$, $p = 0.220$) between the factors.

To further examine the relationship between the timecourse of fluorescence change and experimental condition, the thirteen experimental sessions were collapsed into five categories for both cell pools: habituation, training (RAM day

1-19), negative control (negative control sessions 1 and 2), positive control (novelty session) and retrieval (retrieval sessions 1 and 2).
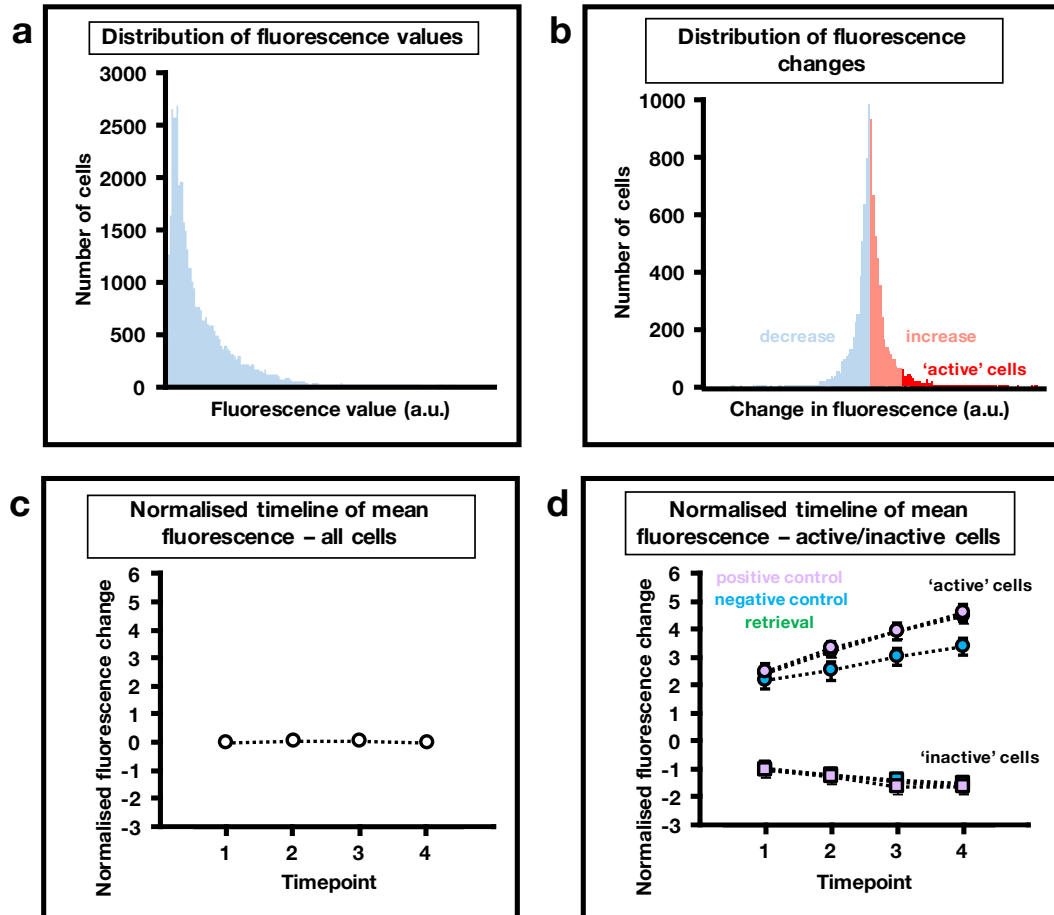
Figure 3.3.5. The characteristics of cell fluorescence values. A – a representative frequency distribution of measured fluorescence values across all thirteen imaging sessions. B – a representative frequency distribution of the change in fluorescence values (time point 4 minus time point 1) across all thirteen sessions. Blue bars show cells which saw a decrease in fluorescence while the other bars show cells which saw an increase in fluorescence. Pink bars represent fluorescence intensity increases below the 1.5×standard deviation criterion while red bars show cells above the criterion – i.e. the 'active cell pool'. C – a mean of the mean normalised population fluorescence intensity values across all mice plotted against the imaging time points. The error bars are buried within the symbols. D – means of the mean normalised 'active' and 'inactive' cell pools' normalised fluorescence intensity values for the positive control (novelty), negative control and retrieval experimental blocks. The retrieval data points are obscured by the novelty condition symbols. a.u. – arbitrary units

The analysis again revealed an interaction between time and condition for the 'active cell pool' ($F_{interaction}(3.05, 18.31) = 6.08$, $p = 0.005$) but not for the 'inactive cell pool' ($F_{interaction}(3.76, 22.54) = 2.15$, $p = 0.111$). Moreover, collapsing the

conditions preserved the main effect of time ($F_{timepoint}$(3, 18) = 270.09, p < 0.001) for the 'inactive cell pool' but removed the main effect of condition ($F_{condition}$(2.03, 12.18) = 1.29, p = 0.311).

Among 'active' cells, Bonferroni-corrected pairwise comparisons revealed significant differences between negative control and training (p = 0.013) and between negative and positive control (p = 0.007) categories with the negative control exhibiting the lowest fluorescence increase among all categories.

3.3.5 Cell activation and experimental condition

The next question asked was whether there was a relationship between the experimental conditions and the percentage of cells activated. An ANOVA revealed a main effect of condition (F(12, 72) = 4.65, P < 0.001)(Figure 3.3.6). To further probe the differences between the conditions, the six training sessions, two control sessions and two retrieval sessions were collapsed into three experimental blocks and analysed along with novelty and habituation. A main effect of experimental block was found (F(4, 24) = 16.75, p < 0.001) and a number of Bonferroni-corrected pairwise comparisons were conducted. The comparisons of training versus control, control versus novelty and habituation versus novelty revealed significant differences (p = 0.004, p = 0.004, p = 0.036, respectively) while the comparison of training versus novelty showed a trend (p = 0.053).
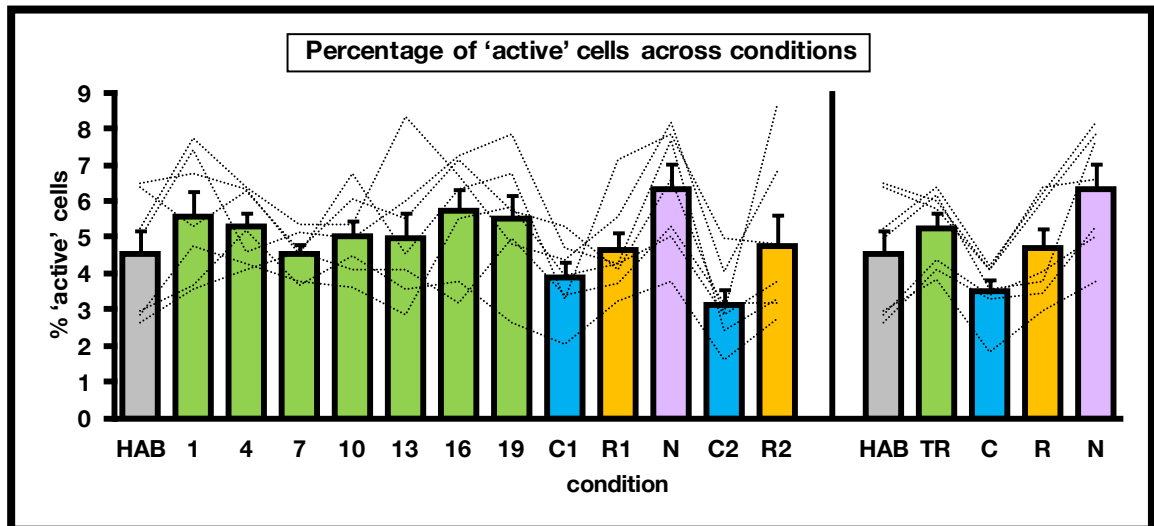
Figure 3.3.6. Figure 2.10. Percentage of 'active' cells across conditions. The left-hand side of the graph shows mean % 'active' cells values across the thirteen imaging sessions while the right-hand side of the graph presents mean data for the experimental blocks. Dotted lines connect data points for individual mice. HAB – habituation, 1-19 – RAM training sessions, C1 – negative control session 1, R1 – retrieval session 1, N – novelty (positive control), C2 – negative control session 2, R2 – retrieval session 2, TR – RAM training experimental block, C – negative control experimental block, R – retrieval experimental block.

3.3.6 Jaccard similarity index and cell co-activation

While differences in cell population activity observed across the experimental conditions suggest the RSC responding differentially to the level of saliency of the experimental stimuli, they do not provide proof for the existence of a memory engram. On the other hand, considering the degree of similarity in the pattern of cell activation throughout the study may reveal whether the observed neurons activated at random or in a context-dependent manner, indicating the presence of an engram.

The similarity of activation patterns was assessed by means of the Jaccard index (Jaccard, 1908). Indices were calculated for each pair of conditions and represented graphically in the form of similarity heat maps (Figure 3.3.7c). Figure 2.11a displays the mean Jaccard similarity index values for the experimental cohort. A visual inspection of the graph reveals a trend towards higher similarity scores as training progresses, reaching the top mean index value of 0.26±0.03 between days 16 and 19. The two retrieval conditions also show a high level of

similarity with the final days of training and between each other. Conversely, the two negative control conditions and novelty show low similarity with the rest of the experimental days.

Another way of graphically representing the similarity between conditions is via a dendrogram calculated based on the Jaccard similarity matrix. The dendrogram (Figure 3.3.7b) clearly reveals the presence of four distinct clusters of conditions: (1) habituation with training day 1, (2) training days 4-19 plus the two retrieval sessions), (3) the two control conditions, and (4) the novelty condition on its own.
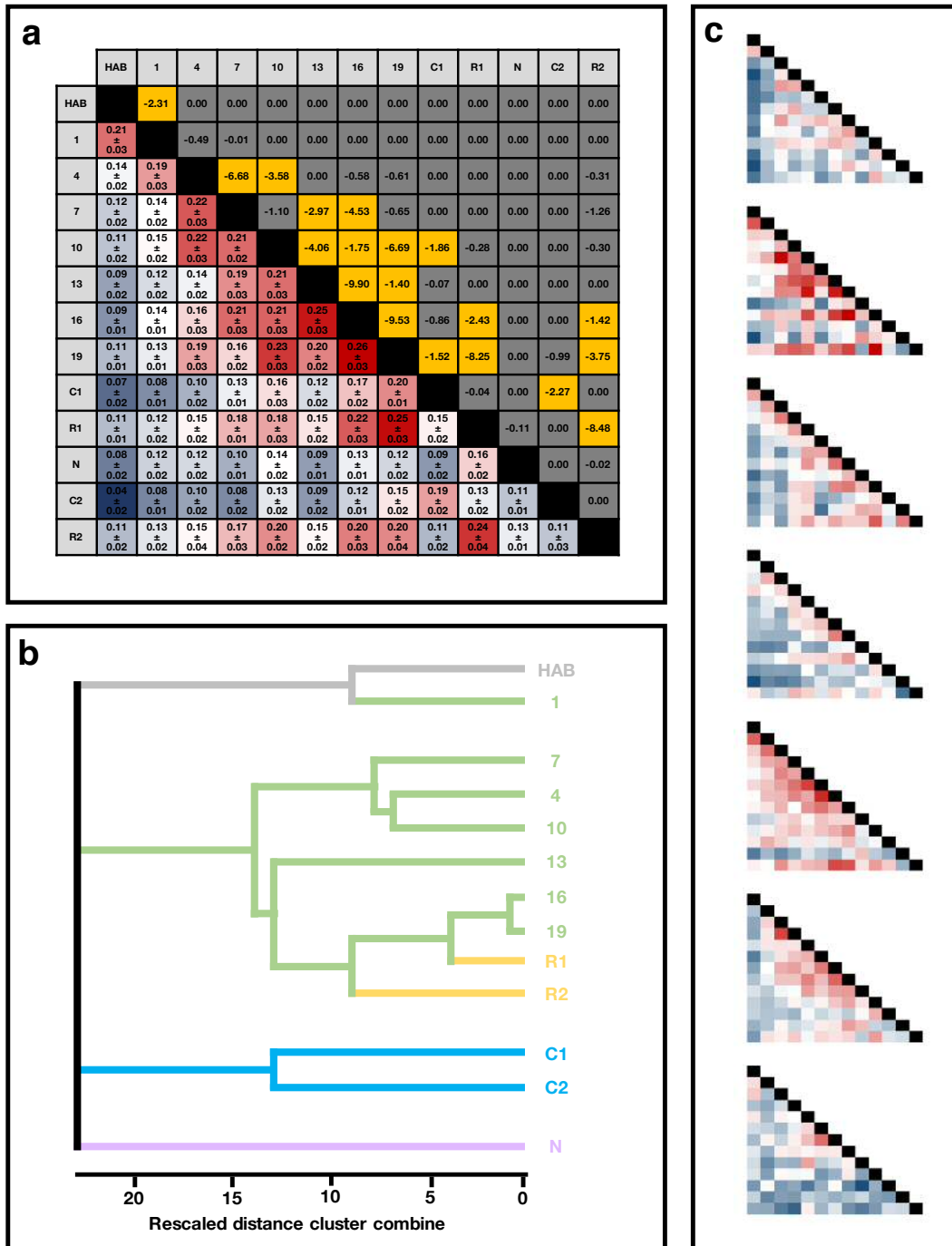
Figure 3.3.7. Jaccard index measurements. A – A heat map of mean Jaccard index values ± standard error of the mean under the diagonal and corresponding $\log_{10}$ p-values above the diagonal. The mean Jaccard values are colour-coded from lowest (dark blue) to highest (red) while significant p-values (lower than 0.05) are highlighted in yellow. **B** – a dendrogram revealing the clustering of the mean Jaccard index values. The scale represents the distance between clusters. **C** – Jaccard index heat maps for all seven mice. The arrangement of condition pairs is the same as for the mean heat map. HAB – habituation session, 1-19 – RAM training sessions, R1 – retrieval session 1, R2 – retrieval session 2, C1 – negative control session 1, C2 – negative control session 2, N – novelty (positive control) session.

It was also investigated whether the observed Jaccard index values were likely to have arisen due to chance. For each set of values t, a, b where t is the size of the 'active cell pool' and a and b represent the number of cells 'activated' on any two days for which the Jaccard index was calculated, a theoretical exact probability distribution function was calculated. In other words, all possible overlap values and their probability of occurrence were calculated for each pair of days. *P*-values for observed Jaccard indices were calculated as 1 minus the sum of probabilities equal to or greater than the likelihood of the occurrence of the observed Jaccard value. As such, the *p*-value represents the (one-sided) likelihood of the observed Jaccard index greater than the expected theoretical distribution of values. It was not possible to obtain an overall, study-wise compound p-value due to the unknown mutual non-independence of Jaccard values.

Overall, compound p-values revealed that only the highest observed Jaccard indices were unlikely to have resulted from chance arrangement of 'active' cells (Figure 3.3.7a). Significant results were found for the Jaccard indices of the following combinations of days: habituation and day 1, day 4 and days 7-10, day 7 and days 13-16, day 10 and days 13-19 plus control session 1, day 13 and days 16-19, day 16 and day 19, day 16 and retrieval sessions 1 and 2, day 19 and control session 1 and retrieval sessions 1 and 2, control session 1 and control session 2, retrieval session 1 and retrieval session 2. There were no significant p-values for any of the combinations with novelty.

3.3.7 Relationship between 'active' cells, Jaccard index and behaviour

The true demonstration of the functional importance of a putative retrosplenial spatial memory engram would be showing its link to the expression of memory upon re-exposure to the task after an extended period of time. The performance of mice on the final retrieval session (R2) exhibited the greatest variance across the entire study, presenting the best experimental window for finding a relationship with neuronal activity.

It was first investigated whether the percentage of 'active' cells on the retrieval session R2 (Perc_R2) displayed a relationship with RM errors (RME). Since the mean percentage of 'active' cells across all sessions (Perc_mean) and Perc_R2 were positively correlated ($r = 0.86$, $p = 0.014$), Perc_mean was designated as a confounding covariate. The relationship between R2 and mean values most likely reflects the dependence of Perc_mean on the overall signal-to-noise ratio of fluorescence. Perc_mean also showed a moderate negative trend with the rostro-caudal position of the ROI (with caudal ROIs displaying lower Perc_mean; $r = -0.67$, $p = 0.103$). Another variable chosen to control for was the percentage of 'active' cells present on the negative control session C2 (Perc_C2), which represents the activity elicited by task-independent stimulation. A partial correlation with the dependent variables of RME and Perc_R2 and with the confounding covariates of Perc_mean and Perc_C2 revealed a strong, positive linear trend ($r = 0.84$, $p = 0.077$)(Figure 3.3.8a). In other words, there was a trend for animals exhibiting high error scores to show a high percentage of 'active' cells when other variables were controlled for.

It was then explored whether the performance of mice on session R2 showed a relationship with the stability of the engram between session R2 and the preceding radial-arm maze session, R1. More specifically, it was investigated whether the R2-R1 Jaccard index (J_{R2-R1}) correlated with the ratio of RME between sessions R2 and R1 (the higher the ratio, the greater the degree of forgetting between the R1 and R2 sessions). A visual inspection of individual animals' heat maps (Figure 3.3.8c) reveals that while the relative pattern of Jaccard index values was similar across cases, the absolute scale of Jaccard indices substantially varied from animal to animal. This is presumed to reflect the signal-to-noise ratio across cases and may be related to the rostro-caudal position of the ROIs (similar trend to that of percentage 'active' cells, $r = -0.59$, $p = 0.16$). A strong, positive correlation was found between mean Jaccard index values (J_{mean}) and the R2-R1 Jaccard index (J_{R2-R1}) ($r = 0.81$, $p = 0.029$). Next, it was explored whether the Jaccard index between control session C2 and session R1 (J_{C2-R1}) displayed a relationship with J_{R2-R1}. This was motivated by the

hypothesis that a possible link between J_{C2-R1} and J_{R2-R1} would reflect the task-independent component of overlap in neuronal activity. Again, a strong, positive correlation was found ($r = 0.81$, $p = 0.028$). Finally, controlling for J_{mean} and J_{C2-R1} in a partial correlation model between J_{R2-R1} and R2-R1 error ratio produced a very strong, negative correlation ($r = -0.9$, $p = 0.04$)(Figure 3.3.8b). In other words, eliminating the influence of signal quality and the non-specific engram component revealed that animals which performed best on session R2 were those which showed the highest degree of task-specific engram stability.

Finally, it was checked whether the percentage of 'active' cells showed a relationship with the Jaccard index. A simple correlation was performed as both variables share common confounds. No dependence of Jaccard index on 'percentage' active cells was found ($r = 0.265$, $p = 0.565$), suggesting that the divergent patterns observed are likely independent.
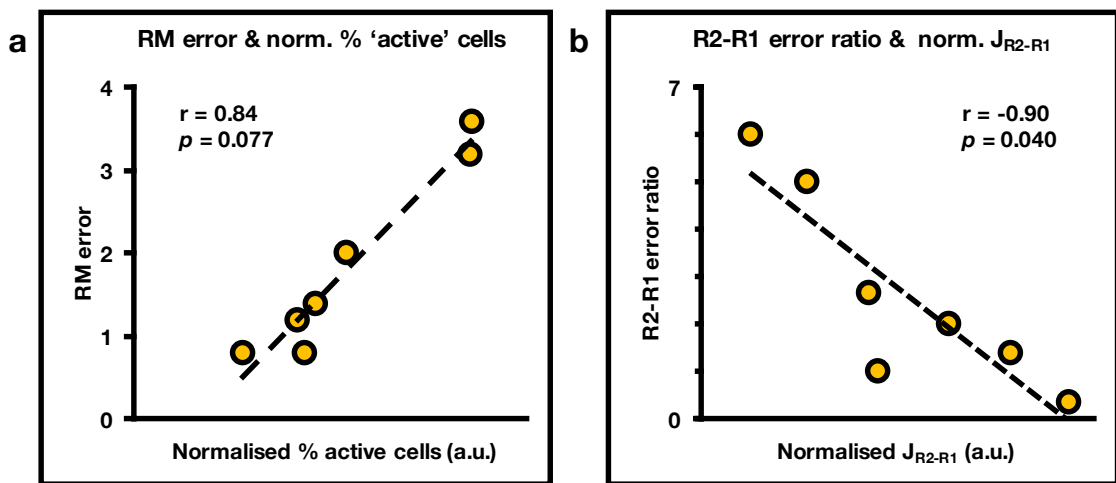
Figure 3.3.8. Partial correlations between percentage 'active' cells and Jaccard index with performance on final retrieval day R2. A – corrected correlation between Perc_R2 and RME. The x axis represents Perc_R2 after normalisation for Perc_mean and Perc_C2. B – corrected correlation between J_{R2-R1} and RME ratio. The x axis represents the J_{R2-R1} after normalisation by J_{mean} and J_{R2-R1} and J_{C2-R1}. a.u. – arbitrary units.

3.4 Discussion

The main finding of the current study is the demonstration of the existence of spatial memory engram cells in the mouse retrosplenial cortex. It was shown that spatial learning is accompanied by the gradual emergence of a context-specific pattern of neuronal activity which is re-instated upon retrieval. Furthermore, the stability of the re-activated engram displayed a relationship with the degree of forgetting, providing, for the first time, direct evidence for the interdependence of spatial memory consolidation and retrosplenial engram formation. Although purely observational, all experimental findings are consistent with theory-driven hypotheses laid out before the onset of the study. Consequently, this work advances our understanding of retrosplenial involvement in spatial memory processes and suggests tools for its further investigation.

3.4.1 Reference and working memory performance on the partially-baited radial-arm maze task

Spatial working memory (SWM) is the ability to temporarily retain limited amounts of spatial information in a readily-accessible manner while spatial reference memory (SRM) is the long-term storage of information pertaining to the fixed spatial arrangement of the environment (Nadel & Hardt, 2010). In the context of the current study, SWM error was defined as re-entry to previously-visited arms while SRM error was defined as entry to non-baited arms (similar to Olton & Papas, 1979). SWM did not show improvement over the course of training and did not differ between training and retrieval. This result was somewhat unexpected as other studies show a clear decrease of SWM errors with training on versions of this task (Gökçek-Saraç, Wesierska, & Jakubowska-Dogru, 2015; He et al., 2002; Jarrard, 1983; Poirier et al., 2008; Pothuzien et al., 2004). Nevertheless, the design employed in the current study was distinctive in at least two ways. First, no highly-salient intra- or extra-maze cues were employed and, consequently, animals had to solely rely on laboratory furniture

for allocentric cues. Second, the task likely exposed the mice to a considerable level of proactive interference (Pothuzien et al, 2004) as they were required to complete five trials in quick succession (1 min inter-trial interval). In contrast to SWM, SRM showed clear improvement over training and remained above naïve performance levels in the two retrieval sessions, this time in line with previously published literature.

The retrosplenial cortex shows immediate-early gene activity during SWM tasks such as the standard of the radial-arm maze (Vann, Brown & Aggleton, 2000) or the Morris water-maze (Shires & Aggleton, 2008); furthermore, both permanent lesions and temporary inactivation of the RSC produce impairments on selected tests of spatial and non-spatial working memory, showing this region is necessary for aspects of working memory (Nelson et al., 2015a; Vann & Aggleton, 2002; Whishaw et al., 2001). The RSC has been proposed to aid the translation between egocentric and allocentric world views (Vann et al., 2009) and recent findings have begun to elucidate the mechanisms which may underlie this function. Proprioceptive inputs carried via the Papez circuit are thought to elicit activity in head-direction and other self-motion-sensitive neurons in the RSC (Alexander & Nitz, 2015; Chen et al., 1994; Cho & Sharp, 2001; Vedder et al., 2016) thereby providing the egocentric navigational frame. The activation of place cells and other more complex allocentric-cue related neurons has also been reported in the retrosplenial cortex (see Chapter 4) (Alexander & Nitz, 2015; Cho & Sharp, 2001; Mao et al., 2017; Smith, Barredo, & Mizumori, 2011) and presumably relies on visual cortico-cortical and pulvinar projections as well as hippocampal and entorhinal inputs carrying scene and body-in-space information, respectively (see **Chapter 1**). A more in-depth account of the importance of the retrosplenial cortex for working-memory processes can be found in the following chapter while its contribution to reference memory will be discussed below along with imaging data.

3.4.2 Regions of interest

The cortical regions of interest were selected based on the fluorescence signal-to-noise ratio and were predominantly located around the mid-point of the rostrocaudal axis of the dysgranular retrosplenial cortex. Whether this was coincidental or reflects a genuine sub-anatomical specialisation of the retrosplenial cortex remains unknown (see Chapter 2 for a more in-depth discussion of the topology and function of the retrosplenial cortex). It is likely that the quality of fluorescence was simply affected by the convexity of the cortex (the degree of orthogonality of the window to the surface of the brain). A modification of the imaging protocol allowing for surveying a larger cortical area might help to resolve this issue in future experiments.

3.4.3 The confirmation of EGFP cell identity as *c-fos*-expressing neurons

Immunohistochemical assessment of the overlap between EGFP, *c-fos* and NeuN confirmed that all EGFP-positive cells were also cfos-positive and NeuN-positive. Although only qualitative in nature, these results are in line with data published by other authors who reported *c-fos*-tTA-driven expression of shEGFP in 59-93% of all cfos-positive neurons (Kim et al., 2015; Liu et al., 2012)(the varying degree of overlap between the two signals most likely arises from the use of different anti-cfos antibodies). While the expression of *c-fos* has been observed in inhibitory neurons (Mainardi et al., 2009; Staiger et al., 2002), it appears that the mouse line used in this study expresses EGFP exclusively in excitatory cells (Liu et al., 2012; Yoshii, Hosokawa & Matsuo, 2016). Finally, all cfos-positive, EGFP-positive cells were also NeuN-positive, indicating no glial involvement, in agreement with previous reports (Herrera & Robertson, Harold, 1996).

3.4.4 *In-vivo* characteristics of the EGFP-positive cells

Previous studies have typically measured *c-fos* levels at 90 minutes following experimental manipulations whereas the current study's imaging time window was set between 1 and 3 hours after behavioural testing (corresponding to 90-210 minutes from the onset of testing). This timeframe was chosen to more

accurately capture the dynamics of the EGFP signal, which is only an indirect readout of true *c-fos* expression levels. No pre-testing imaging was conducted to avoid the effect of imaging itself on the expression of *c-fos*. The maximum fluorescence level observed in the *c-fos*-tTA-EGFP mouse was previously reported at 3 hours post-training (Kim et al., 2015), which likely reflects different patterns of cfos and EGFP protein build-up. This may be due to the short half-life of the fluorophore expressed by mice in this study; the level of fluorescence is a function of not only *c-fos* expression but also the breakdown of EGFP (Xie et al., 2014), apparently reaching the highest ratio at around 3 hours post-training.
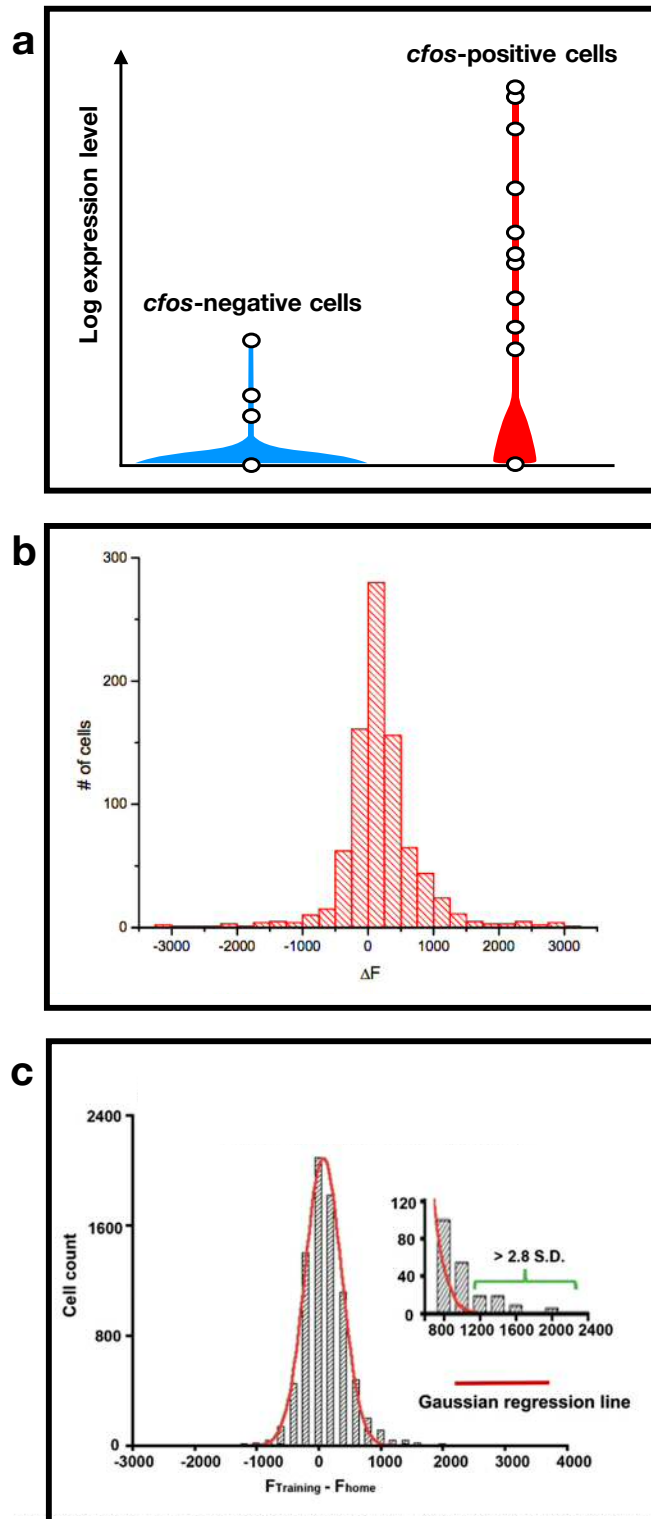
Figure 3.4.1. The continuous distributions of absolute and relative IEG-driven fluorescence signal. A – mRNA-seq cfos expression profiles of 36 cells isolated from the hippocampus of a mouse exposed to a novel environment. Both the cfos-positive and cfos-negative groups of neurons identified via fluorescence-activated cell sorting show a range of cfos expression levels. Modified from (Lacar et al., 2016). B and C – histograms of change in fluorescence in neurons expressing fluorophores driven by cfos (b) (Czajkowski et al., 2014) or Egr1(c) (Xie et al., 2014), following IEG-inducing protocols. There was no evidence for the existence of obvious dichotomy between 'active' and 'inactive' cells in either study.

EGFP-positive cells observed *in-vivo* exhibited a continuum of fluorescence values, suggesting that *c-fos* expression is not binary, as many immunohistochemical studies would imply, but rather graded. mRNA profiling of hippocampal cells confirms this notion (Figure 3.4.1a) (Lacar et al., 2016). Furthermore, two other studies employing transgenic mice expressing IEG-driven fluorophores also observed continuous distributions of changes in fluorescence with no discernible peaks for 'active' neurons (Figure 3.4.1b-c) (Czajkowski et al., 2014; Xie et al., 2014).

Nevertheless, it was still decided in this study to analyse changes in *c-fos* expression based on the classification of cells as 'positive or 'negative'. The reason for that was the need to simplify the very complex data set derived from thousands of individual neurons. A cut-off point of 1.5 × the standard deviation of positive fluorescence change identified a similar proportion of 'active' cells as that described by other authors (Kitamura et al., 2017; Liu et al., 2012; Lux et al., 2016) and was close to that employed by Xie et al. (2014) (a 2.8 × standard deviation threshold in Xie et al. would be equivalent to a 1.4 × standard deviation as calculated in the current study; the current study's threshold is marginally more stringent).

The current study focused its analyses on the population of 'active' cells based on the assumption that fluorescence decrease was not of interest. There were several reasons for that. First, a genuine change from high to low *c-fos* expression levels would be indicative of the engagement of the imaged neurons in processes preceding the behavioural manipulations since *c-fos* activity is thought to be otherwise low at baseline (Kaczmarek & Chaudhuri, 1997; Swank, 2000). Moreover, *c-fos* acts as an autorepressor at its own promoter region and, accordingly, neurons have been described to enter a refractory period of *c-fos* non-inducibility following an initial burst of activity (Morgan et al., 1987), which would here result in fluorescence decrease. Finally, as mentioned above, the EGFP protein is rapidly degraded (Xie et al., 2014) and subject to substantial photobleaching by femtosecond 2-photon laser stimulation (Graham et al.,

2015). Consequently, the increase in the fluorescent signal is indicative of active *c-fos* transcription while a decrease is difficult to interpret and likely an aftermath of task-independent processes.

3.4.5 Task-induced changes in the fluorescent signal

No global stimulus-induced changes in fluorescence were observed in the current study. A possible explanation is that the ROIs for individual cells were based on all thirteen sessions. While this allowed for the reliable tracking of all possible cell activations throughout the study, it may have led to non-active cells being overrepresented when considering mean changes. For instance, a cell which showed high fluorescence levels on session one would be included in all subsequent analyses even if it was not visible on any other session. Since cells with low values of fluorescence were most numerous, global changes were likely predominantly affected by signal noise rather than by changes among cells which were task-relevant.

Nevertheless, the analysis of the time course of fluorescence for 'active' cells revealed a difference between negative control sessions, training and novelty. This distinction was not present in the 'inactive' cell pool, demonstrating that separating cells into these two categories was useful in extracting the meaningful component of the signal.

The proportion of 'activated' neurons across imaging sessions appeared to reflect the level of salience of the sessions with highest values following novelty, intermediate values at training and retrieval and the lowest values at the two negative control sessions. The difference between the positive (novelty) and negative controls demonstrates the actual experimental window for task-specific *c-fos* activation under the protocol employed in this study (which was around 80%). While most human imaging studies have shown that the RSC is preferentially involved when presented with familiar rather than with novel environments (for review see: Epstein, 2008), BOLD and *c-fos* signals represent different physiological processes and show correlations in only some regions of

the brain (Stark et al. 2006). Furthermore, rat data supports the notion that novel environment exploration does induce greater *c-fos* expression than re-exposure to a familiar environment (Jenkins et al., 2002). A recent human functional imaging study demonstrated the preferential engagement of the retrosplenial cortex in encoding novel environmental features (Auger, Zeidman & Maguire, 2015). Finally, the novel condition in the present study was deliberately designed to elicit maximal *c-fos* expression by targeting multiple sensory modalities (visual, tactile, odorant) and the level of neuronal activity may thus reflect not novelty *per se* but the summation of multimodal inputs, which were less abundant in the radial-arm maze.

c-fos activity at retrieval did not differ from training in the current study. By contrast, Maviel et al. (2004) and Barry, Coogan & Commins (2016) demonstrate a positive relationship between retrosplenial *c-fos* expression and time to spatial memory retrieval, with highest levels of activity at 30 days from training. Retrieval of contextual fear-memory has also been shown to follow a similar trend in the retrosplenial cortex (Tayler et al., 2013). It remains unclear why the current study produced different results. One possibility is that the degree of retrosplenial engagement depends on the perceived degree of novelty of the environment the animal is re-exposed to. While other publications typically employ a single training session, followed by retrieval at different time points, in the current study, mice were repeatedly trained for a long period of time and likely became well-familiarised with the testing environment. Consequently, the subsequent retrieval sessions might have induced a low perceived level of novelty. Additionally, repeated training leads to repeated re-consolidation of memory (Dudai, 2012) and updating of engrams. Therefore, the comparison of *c-fos* levels at training and retrieval in this study is not directly equivalent to the comparisons undertaken by other authors. Poirier et al. (2008) reported equal *Zif268* cell counts in the retrosplenial cortex of rats after 2 or 5 sessions of spatial training (equivalent to that used in the current study) while mouse parahippocampal cortex was shown to exhibit a similar, low level of activity at

early fear-memory retrieval (1 day and 30 days) but greatly enhanced activity at very remote time points (6 months and 12 months)(Lux et al., 2016).

3.4.6 The emergence and persistence of the *c-fos* spatial memory engram

Learning of the spatial task was paralleled by the emergence of a stable pattern of neuronal activation. The sensitivity of the engram to context is best illustrated by the presence of four distinct clusters of experimental sessions generated by hierarchical clustering. The first cluster contained the final day of habituation and RAM session number 1, likely reflecting the component of activity associated with the spatial environment itself. The remaining training sessions and retrieval sessions, during which mice showed evidence of learning, formed cluster number 2. This cluster likely reflects the component of the engram linked to the association of the features of the spatial environment with reward, such as that described here (Vedder et al., 2016). The two negative control sessions showed a degree of overlap but were distinct from other sessions (cluster 3) while novelty formed a cluster on its own (4). There did not seem to exist a relationship between the overall level of activation (percentage 'active' cells) and the Jaccard index values since all control conditions, which among them exhibited the lowest and highest activity levels throughout the study, failed to elicit substantial re-instatement of the RAM-associated pattern. Furthermore, the Jaccard index between sessions R2 and R1 did not correlate with the percentage of active cells on session R2.

3.4.7 Relationship between neuronal activation, engram stability and performance at remote memory retrieval

The percentage of 'active' cells on retrieval session R2 showed a positive linear trend with the number of reference memory errors when mean 'active' cells and 'active' cells on negative control session C2 were controlled for. A similar result was reported for rats on an equivalent task (Poirier et al., 2008). The authors found a positive correlation between retrosplenial *Zif268* cell counts and

reference memory error in animals which reached asymptotic performance (5 training sessions) but not in animals which received shorter training (2 sessions). A positive correlation between *c-fos* cell counts and escape latency of rats (higher escape latency indicates poorer learning) on the Morris water-maze task has also been reported (Sherstnev et al., 2013). On the other hand, no correlation between performance on the same water-maze task and *c-fos*—driven fluorescence was found by Czajkowski et al. (2014). The inverse relationship between spatial task mastery and *c-fos* expression levels in the RSC highlights the importance of sparse coding for efficient information storage and retrieval, which has strong theoretical basis and has been experimentally demonstrated in certain brain regions (Han et al., 2013; Palm, 2013; Tonegawa et al., 2015). Moreover, there appear to exists inhibitory mechanisms which serve to actively constrain the size of engrams, at least in subcortical areas (Morrison et al., 2016).

In contrast to overall *c-fos* activity, memory engram stability showed a negative relationship with errors. Since it was the degree of similarity of neuronal representations between sessions R2 and R1 that was of interest, it was the ratio of R2/R1 performance rather than raw error scores that were employed in the analysis. A partial correlation between the error ratio and R2-R1 Jaccard index controlling for mean Jaccard index and C2-R1 Jaccard index revealed a strong, negative correlation. The apparent relationship of successful reference memory retrieval with the sparsity and fidelity of reinstatement of the retrosplenial engram fits well with current opinion on the requisites of efficient neuronal coding (Han et al., 2013).

The reinstatement of the neuronal pattern of activity established during encoding has been shown to be critical for the expression of fear-memory upon retrieval (Kitamura et al., 2017; Tanaka et al., 2014). Moreover, training (Shakhawat et al., 2014) as well as simply passage of time (Kitamura et al., 2017) have been shown to lead to the strengthening of cortical engrams. It is impossible to conclude whether the maturation of the spatial reference memory engram observed in the current study resulted from training, time or both factors. This could be

addressed for example by carrying out a between-subjects design with one group of animals undergoing repeated training and another group only exposed to a single radial-arm session before retrieval. Lesion and chemogenetic inactivation studies have also implied the role of the retrosplenial cortex in the long–term storage of emotionally-charged auditory information (Todd et al., 2016). Lesions of the retrosplenial cortex following encoding was shown to affect remote but not early memory retrieval.

Human functional imaging studies indicate that the retrosplenial cortex is involved in long-term storage of memory. The level of retrosplenial activity increased with increased performance on a spatial task requiring participants to memorise a map (Wolbers & Buechel, 2005)(this is not necessarily equivalent to higher levels of IEGs, as described above).

3.4.8 Limitations of the current study and future directions

Despite important new insights into the role of the retrosplenial cortex in the storage of spatial memory, the current study has some limitations. First, *c-fos* imaging is an indirect method of assessing activity in neuronal ensembles. Other techniques such as electrical recordings or calcium imaging offer much more detailed information about the dynamics of cortical signals and would undoubtedly complement the current results. It would also be of interest to investigate whether *c-fos*-positive cells differ from their neighbours in terms of basic electrophysiological properties and connectivity with other brain regions. This could be studied using *in-vitro* patch-clamp methods as well and tract-tracing, respectively. Next, conducting a complex multistage study makes it difficult to include many experimental cases and the 7 mice employed here may not have provided enough power for uncovering more subtle phenomena as well as inter-animal differences. Many studies have shown that both humans and rodents often fall into two categories of good versus poor learners (e.g., Auger et al., 2015), especially when assessed at long delays from task acquisition. It was not possible to address this in the current study. Moreover, all results presented in this report are purely observational. Further support for the role of

the retrosplenial cortex in engram formation could come from appropriate controls such as yoked animals and animals with disturbed retrosplenial activity (for example by means of chemogenetic or optogenetic manipulations). Additionally, the small cortical areas sampled in the current study may not adequately reflect retrosplenial function across its many subdomains, including the distinction between posterior and anterior regions and superficial versus deep layers. Nevertheless, the current study remains a valuable addition to the growing body of evidence implicating the retrosplenial cortex in memory processes.

4 Retrosplenial cortex in a model of Diencephalic Amnesia

4.1   Introduction

As discussed in **Chapter 1**, the processing of memory requires the interaction between multiple brain sites. While the overwhelming focus over recent years has been placed on the hippocampal formation, the retrosplenial cortex and the medial diencephalon (i.e. the mammillary bodies and anterior thalamic nuclei) also play a key role in memory. Damage to the medial diencephalon can produce diencephalic amnesia, which presents primarily as the inability to form new episodic memories (anterograde amnesia) and, in some cases, also difficulty with remembering events prior to the onset of amnesia (retrograde amnesia)(e.g., Hunkin & Parkin, 1993). Patients with diencephalic amnesia are also particularly poor at remembering the temporal order of events (Downes et al., 2002). In contrast, other types of memory, such as working memory (e.g., digit span) and procedural memory are left relatively intact (Fama, Pitel & Sullivan, 2012).

Medial diencephalic damage may occur in a number of conditions, including stroke (Yoneoka et al., 2004), penetrating brain injury (Squire et al., 1989), colloid cysts in the third ventricle (Denby et al., 2009), schizophrenia (Bernstein et al., 2007) but also neurodegenerative disease such as Alzheimer's Disease (Aggleton et al., 2016) and Korsakoff's Syndrome (an encephalopathy induced by thiamine deficiency)(Kopelman, 1995). It is, is therefore, an important goal to understand how and why damage to this region has such devastating effects on memory.

4.1.1 Animal models of diencephalic amnesia

Although there are numerous patient studies that have implicated the medial diencephalon in memory, their limitation is that damage is often nonspecific and includes additional brain regions. Korsakoff's Syndrome, which is the most extensively researched form of diencephalic amnesia, produces widespread grey and white matter changes (Shimamura et al., 1988), consequently making it difficult to assign importance to any one of the involved brain regions. By using

animal models, it is possible to selectively lesion structures within the medial diencephalon in order to determine their precise contributions. Findings from animal models have confirmed the importance of the anterior thalamic nuclei and mammillary bodies in many aspects of memory. Lesions to the mammillary bodies, anterior thalamic nuclei and the white matter pathway connecting these two structures (the mammillothalamic tract) have repeatedly been shown to impair performance on spatial memory tasks (Mitchell & Dalrymple-Alford, 2006; Vann, 2013; Vann & Aggleton, 2003). Consistent with findings from patients, lesions to both the mammillothalamic tract and anterior thalamic nuclei also disrupt temporal memory (Dumont & Aggleton, 2013; Nelson & Vann, 2017). This suggests that the memory impairments in diencephalic amnesia are most likely due to damage to the anterior thalamic nuclei and mammillary bodies and also validates the use of animal models for studying diencephalic amnesia.

4.1.2 Diencephalic amnesia and distal hypoactivity

While the medial diencephalon has been implicated in memory since the late 19th century (Gudden, 1896), it is still not clear why damage to this region produces amnesia. One possibility is that disruption to this region results in a disconnection syndrome. The medial diencephalon is thought to be an important route via which the hippocampus may exert its influence on the cingulate cortex (Papez, 1937) and also a vital relay of midbrain projections to both the hippocampal formation and the retrosplenial cortex (Vann, 2013). The loss of the projections carried via the medial diencephalon could, therefore, produce hippocampal and retrosplenial dysfunction. Given the importance of the hippocampus and retrosplenial cortex for memory (see **Chapter 1**), it is possible that this diaschisis (secondary impairment caused by distal lesions) could contribute to the memory impairments following diencephalic damage.

Support for this disconnection model has come from imaging studies as patients with diencephalic amnesia show reduced functional activity in the hippocampus and retrosplenial cortex (Caulo et al., 2005; Reed et al., 2003). However, these

studies involved patients with Korsakoff's Syndrome, so these distal changes could in fact reflect pathology outside of the medial diencephalon.

Again, animal models are able to address some of the limitations of patient studies by looking at the effects of more discrete lesions. There is evidence that medial diencephalic damage can affect both the retrosplenial cortex and hippocampus in rats. Anterior thalamic lesions reduce *c-fos* expression in both the hippocampus and retrosplenial cortex (Jenkins et al., 2002; Poirier & Aggleton, 2009) (but see: Dalrymple-Alford et al., 2015). Anterior thalamic also disrupt a number of other activity markers in retrosplenial cortex including cytochrome oxidase (Mendez-Lopez et al., 2003), phosphorylated-CREB and *Zif268* (Dumont et al., 2012) and a number of transcription factors including *brd8, fra-2, klf5, nfix, nr4a1, smad3, smarcc2 and zfp9* (Poirier et al., 2008).

At present, it is still not clear why these distal functional changes occur following anterior thalamic lesions. Since the anterior thalamic nuclei have dense bilateral connections with the retrosplenial cortex (see **Chapter 1**) and also directly innervate the hippocampus, it is possible that distal changes observed following anterior thalamic damage simply reflect deafferentation. Lesions of the mammillothalamic tract disconnect the mammillary bodies from the anterior thalamic nuclei and so would only indirectly affect the retrosplenial cortex and hippocampus. Assessing the distal effects of mammillothalamic tract lesions could, therefore, determine the extent to which hypoactivity following anterior thalamic lesions reflects direct deafferentation.

There is preliminary evidence to suggest that retrosplenial and hippocampal changes following diencephalic damage are not simply due to deafferentation and in main, reflect the loss of the mammillary body projections to the anterior thalamic nuclei. This is because mammillothalamic tract lesions produce a very similar pattern of *c-fos* changes to that seen after anterior thalamic nuclei lesions. However, it is not known whether mammillothalamic tract lesions have an impact beyond this immediate-early gene. An important goal would be to

determine more comprehensively the pattern and extent of distal changes following mammillothalamic tract lesions. The previous mammillothalamic tract lesion studies are also limited as they only looked at *c-fos* changes once animals had undergone behavioural training and were not able to assess changes over time within the same animal, highlighting the need to use a technique that would enable a longitudinal assessment of changes. This was the aim of the present study and the approaches used will be described below.

4.1.3 Diffusion tensor imaging

Magnetic resonance imaging has the benefit of non-invasiveness, allowing for the collection of structural and functional scans in living animals. As such, it enables multiple scans to be acquired for the same animals and so providing a longitudinal assessment of brain-wide changes following lesion. Using *in vivo* scanning with animal models provides the unique opportunity to look at within-animal changes following selective brain lesions which can then be assessed histologically.

The present study made use of diffusion tensor imaging (DTI) to assess the effects of mammillothalamic tract lesions by imaging animals both before and after surgery as well as before and after behavioural training on a spatial memory task. DTI is a structural magnetic resonance method which relies on the magnetic properties of water molecules in order to study their movement along applied magnetic field gradients. Since random Brownian motion of water is limited by the presence of local diffusion barriers, such as the neuropil, axon fibres and cell bodies, measuring water movement can reveal information about the microstructural architecture of the brain. Multiple diffusivity metrics can be derived from DTI data. Among them, mean diffusivity (MD) represents the degree to which water molecules can freely move in all directions while fractional anisotropy (FA) is a measure of the directionality of water movement. MD has most extensively been applied to the study of grey matter while FA is most commonly used to measure the integrity of white matter (Bihan et al., 2001) and can be employed in tractography, that is modelling of the distribution of white

matter fibres in the brain. FA can also be useful in the study of grey matter microstructure (Hansen et al., 2013; Komlosh & Basser, 2007; Nguyen et al., 2015). Specifically, FA may reflect the abundance and complexity of cell processes (including dendrites) under high-resolution imaging.

DTI can be employed to measure learning-induced brain plasticity. In human participants, a virtual navigational task was shown to decrease MD and increase FA values within multiple grey matter regions, most consistently, the left hippocampus (Sagi et al., 2012; Tavor, Hofstetter & Assaf, 2013). These changes were found to be transient and most likely reflect short-term structural plasticity as opposed to overt changes to white matter organisation. Similar changes in DTI measures were also found in rats performing a version of the Morris Water Maze where they were required to learn the fixed location of a hidden platform upon multiple trials within the same session (Hofstetter & Assaf, 2017; Sagi et al., 2012). Specifically, training led to a decrease in hippocampal MD values while, in another study, hippocampal and posterior cingulate (retrosplenial) FA values were reported to diminish following training (Blumenfeld-Katzir et al., 2011).

Importantly, studies in rodents may offer some explanation as to what changes in DTI measures actually represent. Decreases in MD in the hippocampus were found to be paralleled by enhanced staining for the glial-fibrillary acidic protein (GFAP), synaptophysin and brain-derived neurotrophic factor (BDNF) (Sagi et al., 2012) as well as the elaboration of astrocytic processes and their cellular volume (Blumenfeld-Katzir et al., 2011). Together, these results suggest a link between changes in water diffusivity and many known correlates of neuroplasticity.

4.1.4 DTI and disease

Diffusivity of water in the brain drastically changes following stroke (Gregory et al., 1996; Lythgoe et al., 1997) and physical trauma (Akpinar, Koroglu & Ptak, 2007) as a result of cavitation, extravasation of blood and tissue oedema. DTI is considered a more sensitive diagnostic measure of the extent of damage than

traditional magnetic resonance imaging and, for that reason, it has found widespread use in the clinic (Benedict et al., 2013; Feldman et al., 2014). In the present study, DTI imaging of grey matter may therefore provide a particularly sensitive measure of tissue disruption following lesion.

In addition to measuring the dysfunction of grey matter areas, DTI has also been extensively used to track changes to white matter fibres. It was found that the FA of white matter shows an increase during the maturation of the brain (Klingberg et al., 1999), reaching peak values in healthy adults. On the other hand, ageing leads to a progressive loss of white matter anisotropy, which correlates with cognitive deterioration (Grieve et al., 2007). Overly high FA values may, however, also signify pathology such as in the neurodevelopmental Williams syndrome characterised by intellectual and visuospatial processing deficits (Hoeft et al., 2007).

Moreover, altered FA has been reported in a neurodegeneration rat model of thiamine deficiency (Dror et al., 2009). Specifically, the thalamus showed a decrease in FA while the cortex exhibited an increase in FA values. These results are particularly relevant to the current study as thiamine deficiency leads to the pathogenesis of Korsakoff's Syndrome and, consequently, constitutes one of the causes of diencephalic amnesia. It would be of interest to observe changes to thalamic and cortical FA values following lesion of the mammillothalamic tract in the present study as it could help to answer whether the FA alterations observed in the thiamine deficiency model reflect physiological disruption of overall brain activity or, perhaps, are specifically linked to medial diencephalic damage.

In conclusion, DTI imaging may prove particularly useful in revealing the interaction between mammillothalamic tract lesions and learning-induced brain-wide plastic changes as well as lesion-induced microstructural damage.

4.1.5 Cytochrome oxidase as a marker brain metabolism

A second cohort of rats in the present study was investigated for the expression of cytochrome oxidase. Cytochrome oxidase is the final component of the mitochondrial electron transport chain and, as such, its levels control the amount of energy available to neurons. The relationship between cytochrome oxidase and neuronal activity has been successfully studied by means of 3,3'-diaminobenzidine(DAB) staining, which accounts for both the abundance and enzymatic activity of cytochrome oxidase (Wong-Riley, 1989). A decrease of cytochrome oxidase has been demonstrated in the brains of Alzheimer's Disease (AD) patients (Kish et al., 1992; Mutisya et al., 1994) and, in the retrosplenial cortex, in individuals in prodromal stages of AD (Valla, et al, 2001).

Employing cytochrome oxidase staining in this study may help to establish whether retrosplenial hypoactivity following lesions of the medial diencephalon simply reflects the effect of deafferentation, as may be the case following anterior thalamic damage, or perhaps, more generally, the loss of functional inputs arising from the mammillary bodies. Moreover, optical imaging of immunohistochemical staining provides better anatomical resolution than magnetic resonance imaging and may therefore deliver complementary insights into the pathogenesis of diencephalic amnesia by enabling specific subregions to be assessed within the retrosplenial cortex and hippocampus.

4.1.6 Design of the present study

In the present study, two cohorts of rats were subject to either lesions of the mammillothalamic tract or control surgery and subsequently tested on a working-memory task in the radial-arm maze to provide a measure of memory impairment.

Lesions were assessed using the appearance of fixed tissue, stained for Nissl bodies and calbindin. Calbindin is a calcium-binding protein (Chard et al.,1993) which is prominently expressed by projection neurons of the mammillary bodies.

Strong calbindin staining is also present in the neuropil of the ventrolateral portion of the anteroventral thalamic nucleus, which is one of the main outputs of the mammillary bodies (Rogers & Reisiboi, 1992). Consequently, the degree of loss of calbindin immunoreactivity in the anterior thalamus following lesions of the mammillothalamic tract is indicative of the completeness of the lesion (incomplete lesions would lead to partially-spared staining for calbindin).

Cohort 1 underwent four DTI (diffusion tensor magnetic resonance imaging) scanning sessions to reveal microstructural tissue changes induced by lesions and by training on the working-memory task. The use of magnetic resonance imaging (MRI) offered the ability to study the progression of changes in the entire rodent brain, in an unbiased manner, and has an added translational benefit as results reported here may guide future studies of diencephalic amnesia patients.

The mammillothalamic tract was hypothesised to exhibit decreased fractional anisotropy and increased mean diffusivity following lesion. Furthermore, it was also hypothesised that DTI would reveal differential fractional anisotropy and mean diffusivity levels in areas of the brain previously associated with 'covert' pathology in diencephalic, including the anterior thalamus, retrosplenial cortex and dorsal hippocampus. For the retrosplenial cortex, it was expected that differences between sham and lesion cases would be most apparent in the context of task acquisition.

In **Cohort 2**, fixed tissue was examined for the presence of cytochrome oxidase staining, a marker of metabolic activity, in the retrosplenial and dorsal hippocampal areas. These two regions were selected as they had previously been shown to exhibit signs of 'covert' pathology in rodent models of diencephalic amnesia, which might be linked to altered metabolism. Furthermore, cytochrome oxidase staining might complement findings derived from the DTI study, first, because it represents metabolic rather than structural changes, and second, because it could be studied with much better anatomical precision. This is of importance as distinct domains within the hippocampus and

the retrosplenial cortex exhibit distinct connectivity patterns and are believed to contribute to different aspects of memory processing.

4.2 Methods

4.2.1 Experimental animals

The experimental subjects were 27 male Lister Hooded rats (Envigo, UK) (**Cohort 1**) and 23 male Dark Agouti rats (Harlan, UK)(**Cohort 2**). The 27 rats in **Cohort 1** (DTI study) weighed 300-340 g at the time of surgery and the 23 rats in **Cohort 2** (cytochrome oxidase), weighed 226–252 g. All rats were housed in cages of 2-4 animals under diurnal light conditions (14 h light/10 h dark) and behavioural testing was carried out during the light phase at a regular time of day. Rats were thoroughly handled before the study began and were given free access to water throughout the experiments. During the behavioural test period, the animals were food-deprived but their body weight did not fall below 85% of their free-feeding weight. All experiments were carried out in accordance with UK Animals (Scientific Procedures) Act, 1986 and associated guidelines.

4.2.2 Stereotaxic surgery

Animals in each cohort were divided into two groups: one received bilateral MTT lesions (**Cohort 1**: MTTx1, n=16; **Cohort 2**: MTTx2, n=13), while the other group underwent control surgery (**Cohort 1**: Sham1, n=11; **Cohort 2**: Sham2, n=10).

Before surgery, rats in each cohort were deeply anaesthetised with either 5% isoflurane in medical air (100% O_2; Cardiff University stocks) (**Cohort 1**) or by intraperitoneal injection of sodium pentobarbital (60 mg/kg pentobarbital sodium salt; Sigma–Aldrich, United Kingdom)(**Cohort 2**) and then positioned in a stereotaxic head-holder (David Kopf Instruments, USA). Rats in **Cohort 1** were further maintained under anaesthesia with 1.5-2% isoflurane in medical air while rats in **Cohort 2** were provided with medical air only. At the start of surgery, rats received a subcutaneous injection of an analgesic (Meloxicam; Boehringer Ingelheim, Germany). The position of the incisor bar of the stereotaxic frame was set at -3.3 mm to the interaural line for **Cohort 1** and +5.0 mm for **Cohort 2**. A

midline incision was made on the top of the scalp to expose the dorsal skull, which was drilled at the point of the lesion. An electrode (0.7mm tip length, 0.25mm diameter; Diros Technology Inc., Toronto, Canada) was lowered vertically and its tip temperature was raised to 72°C at 5 W of power for 1:15-1:25 min for **Cohort 1** and 70°C for 22 s at 25 W for **Cohort 2** using an OWL Universal RF System URF-3AP lesion maker (Diros Technology Inc., Canada). The stereotaxic coordinates were: AP -2.5 mm in **Cohort 1** and -2.0 mm in **Cohort 2** (relative to bregma), LM ±0.9 mm in both cohorts (relative to bregma), and DV -6.9 mm for **Cohort 1** and -6.2 mm for **Cohort 2** (from the top of the cortex). For the surgical controls, in each cohort, the electrode was positioned at the same AP and LM coordinates but was only lowered to a DV position of +1.0 mm above the lesion site to avoid damaging the tract and left *in situ* without raising the temperature of the tip. The different lesion parameters are a reflection of the refinement of the procedure (**Cohort 2** surgeries took place several years before **Cohort 1** surgeries; **Cohort 1** surgeries were carried out by Michal Milczarek and James Perry and **Cohort 2** were carried out by Seralynne Vann). After surgery, the skin was sutured, an antibiotic powder applied (Acramide: Dales Pharmaceuticals, UK) and animals received 5 ml of glucose saline subcutaneously. They were then placed in a temperature-controlled recovery box until they awoke from the aesthetic. Animals were allowed 2–3 weeks to recover before starting any behavioural training during which time all animals had recovered their preoperative weight.

4.2.3 Radial-arm maze testing (Cohorts 1 and 2)

4.2.3.1 *Testing timeline*

Cohort 1 was run on a total of 32 trials over 16 testing sessions (2 trials/session) spaced every other day. As rats had been operated on in groups of four over the course of 7 days and each rat began training at exactly 13 weeks after surgery, it was possible to run all animals in parallel and to subject them to magnetic resonance scanning (in groups of four) on the second and on the final session of the task. **Cohort 2** was run on a total of 18 trials taking place on consecutive

114

days, at 11 months after surgery. Prior to that, rats in **Cohort 2** had also participated in a number of other behavioural tasks reported elsewhere (Nelson & Vann, 2014).

4.2.3.2 Apparatus

The eight-arm radial maze consisted of a wooden central platform (diameter 34 cm) and eight equally spaced wooden radial arms (each 87 cm long and 10 cm wide); the walls of the arms were made of clear Perspex panels (height 12 cm). A clear Perspex guillotine door (height 24 cm) attached to a pulley system was placed at the beginning of each arm so that access from the central platform to each arm could be controlled by the experimenter. There were food-wells at the end of each arm into which the sucrose reward pellets could be placed.

Two identical radial-arm mazes (one referred to as the 'familiar room' and one as the 'unfamiliar room', see below) were placed in two rooms easily discriminable for size (Room 1: 295 cm by 295 cm by 260 cm; Room 2: 255 cm by 330 cm by 260 cm), shape, lighting and with distinct visual cues on the walls to help animals to orientate in the maze (e.g., high-contrast stimuli and geometric shapes).

4.2.3.3 Pretraining

Animals in **Cohort 1** were naïve to behavioural training and therefore received 4 habitation sessions prior to testing while animals in **Cohort 2**, which had been tested on multiple other tasks, required only 2 habituation sessions. Habitation involved unrestricted exploration of the eight arms of the maze, each containing a scattering of sucrose pellets (45 mg; Noyes Purified Rodent Diet, U.K.) for 5 minutes.

4.2.3.4 Working memory version of the radial-arm maze task

The working memory version of the radial-arm task involved the retrieval of sucrose pellets from each of the eight arms of the maze. At the start of the trial, all arms were baited with either one (**Cohort 1**) or two (**Cohort 2**) sucrose pellets. The animal was placed on the centre platform of the maze and allowed to make an arm choice. After returning to the centre platform, all doors were shut for 10 s before being re-opened and the animal could then make another arm choice. This procedure continued until all arms had been visited or 10 min has elapsed. As opposed to the reference-memory radial-arm maze task described in **Chapter 3**, this version of the task taxes only the working-memory ability of the animals as pellets are placed in all arms of the maze; the success on this task requires only remembering which arms have been visited within each session.

4.2.3.5 *Forced-run version of the radial-arm maze task*

Prior to perfusion, animals in both cohorts were also subject to a forced-run version of the radial-arm maze task. The forced-run task differs from the working-memory task in that animals have no choice over arm visits. Arm doors are opened one-by-one by the experimenter, in a pseudorandomised order, until all arms have been visited. Consequently, each rat is forced to visit all eight arms on each trial. This task was used because MTT-lesioned rats are normally impaired on the standard working memory version (Vann and Aggleton, 2003; Nelson and Vann, 2014). In this way, lesioned and control animals could be matched for motor responses and the number of rewards received.

Rats in both cohorts were run on the forced version of the task shortly after completion of the working-memory stage. They were first introduced to the forced-run version of the task during one (**Cohort 1**) or two (**Cohort 2**) sessions in the familiar room where working memory had been tested. This was followed by a final forced-choice session in the unfamiliar room. Each rat was placed in a dark and quiet room for 30 minutes before running the task and then for 90 minutes after task completion, which was followed by perfusion. The 90 min time-window was chosen to match other studies where immediate-early gene

(**see Chapter 3**) or cytochrome oxidase (Mendez-Lopez et al., 2013) were assessed through immunohistochemistry.

Animals in **Cohort 1** were run by Michal Milczarek, Heather Phillips and James Perry while animals in **Cohort 2** were run by Moira Davies and Heather Phillips.

4.2.4 Diffusion Tensor Imaging (Cohort 1)

Animals received four magnetic resonance scanning sessions: 6 weeks before surgery (**scan 1**), 9 weeks after surgery (**scan 2**), following the second session of radial-arm testing (13 weeks from surgery)(**scan 3**) and following the final session of radial-arm testing (17 weeks from surgery)(**scan 4**). The rats were placed in a dark and quiet room for 60 min before scanning, and on radial-arm test days, also for 30 min before testing.

Rats were scanned with a 9.4 Tesla MRI machine (Bruker, Germany) with a 72 mm, 500 W four-channel transmit coil. The protocol comprised first a multi-gradient structural T2 RARE scan (2 repetitions; 24 slices at 500 μm z-spacing and an xy resolution of 137 μm; duration: 10 min 40 s), followed by a DTI scan with a diffusion-weighted spin-echo echo-planar-imaging (EPI) pulse sequence and, finally, a resting-state functional MRI scan (not described here, duration: 5 min)). The DTI acquisition parameters were TR/TE=4000/23.38 ms, 1 EPI segment, 32 gradient directions with a single b-value at 1000 s/mm^2 and five images with a b-value of 0 s/mm^2 (B0). Each scan included 24 coronal brain slices of 500 μm thickness and an xy resolution of 273 μm. The duration of the EPI acquisition was 40 min.

During scan acquisition, rats were lightly anaesthetised with 1-1.5% isoflurane in medical air and placed on a heatmat. The heart rate, breathing rate and temperature of the animals was monitored throughout each scanning session. The entire scanning protocol lasted just over an hour and DTI images were

acquired between 80-100 minutes from the end of behavioural testing. All scans were carried out by Andrew Stewart.

4.2.5 Tissue processing

After completion of the final forced-run radial-arm session, animals in both cohorts were anaesthetised with sodium pentobarbital (60 mg/kg, Euthatal, Rhone Merieux, UK) and then transcardially perfused with 0.1M phosphate buffer saline (PBS) followed by 4% paraformaldehyde in PBS (PFA). The brains were then extracted and postfixed in 4% PFA for 4 h, and then transferred to 25% sucrose in distilled water overnight. On the following day, brains were cut in the coronal plane using a freezing microtome (slice thickness 40 µm).

For both cohorts, two series of sections were cryoprotected in an ethylene glycol/sucrose solution at -20°C. One series was subsequently processed for calbindin immunostaining for both cohorts. For **Cohort 2**, an additional series was processed for cytochrome c oxidase staining. A third series was mounted for both cohorts directly onto gelatin-coated slides and stained using cresyl violet (a Nissl stain) for verification of the lesion location and size.

4.2.5.1 Cresyl violet staining (Cohorts 1 and 2)

Mounted sections were rehydrated by placing them in decreasing concentrations of ethanol in distilled water and then submerged in the cresyl violet staining solution for 3-6 min until the desired level of staining was obtained. The sections were then washed in distilled water and dehydrated in a series of increasing ethanol concentrations. Finally, the sections were cleared with xylene, coverslipped and air-dried.

4.2.5.2 Cytochrome c oxidase staining (Cohort 2)

The sections were first washed six times in PBS (10 min each) to remove any residual cryoprotectant. The sections were then washed twice in 0.1M Tris buffer (5 min each). The incubation medium (30 mg DAB (Sigma D-5637), 15 mg

cytochrome c (Sigma C2506), 2.4 g sucrose; all in 0.1M Tris buffer) and the sections were then separately warmed to 37°C, and then combined and incubated for a further 30–60 min until a desirable level of staining was obtained. The reaction was stopped by washing with 0.1M Tris buffer three times (5 min each) and sections were stored at 4°C overnight. The following day, sections were again washed three times 0.1M Tris buffer (5 min each), mounted, air-dried and coverslipped. Tissue from the MTTx2 and Sham2 groups was processed together.

4.2.5.3 *Calbindin immunohistochemistry (***Cohorts 1 and 2***)*

The sections were washed six times in PBS to remove any residual cryoprotectant (10 min each). This was followed by an endogenous peroxidase activity block in 0.3% hydrogen peroxide solution (0.3% H_2O_2, 10% methanol, distilled water), after which the sections were washed three times in PBS (10 min each). To minimize non-specific binding, sections were incubated in 3% horse serum in PBST (PBS plus Triton X-100 at 500 µL/1L PBS) for 1 h and then incubated for 48 h with a primary anti-calbindin antibody (D-28 K, CB300, Swant, Switzerland) in 1% horse serum in PBST. Following this incubation period, sections were washed three times in PBST (10 min each) and incubated with a secondary antibody (in 1% horse serum in PBST) raised against the primary antibody molecule for 2 h (BA-2000, Vector Laboratories). This was followed by three PBST washes (10 min each) and incubation in an avidin–biotin-kit solution (Elite Kit, Vector Laboratories) for 1 h. Following four more washes (10 min each), the label was developed with the DAB kit according to the manufacturer's instructions (DAB Substrate Kit, Vector Laboratories). All incubations took place at room temperature and, except for the final incubation, on a shaker. The sections were then mounted on gelatine-coated glass slides, air-dried and cover-slipped. Perfusions and tissue processing was carried out by Michal Milczarek, Heather Phillips and James Perry for **Cohort 1** and Heather Philips and Moira Davies for **Cohort 2**.

4.2.5.4 Imaging of processed tissue

Imaging and subsequent analyses were carried out without knowledge of group assignment. Images were obtained with a Leica DMRB microscope used in combination with an Olympus DP70 camera.

4.2.6 Histological validation of lesion success

*4.2.6.1 Cresyl violet staining of Nissl bodies (**Cohorts 1 and 2**)*

For both cohorts, the success of the lesion was first qualitatively assessed with cresyl violet staining. This stain provides good contrast between the strongly-labelled cells of the grey matter and the lightly-stained fibres of the white matter. Several images of the mammillothalamic tract were taken for each animal at positions -2.5 mm to -3.6 mm posterior from bregma. Two investigators independently evaluated the presence of the mammillothalamic tract on both hemispheres of the brain. Cases where any sparing of the tract was apparent were denoted as incomplete lesions.

*4.2.6.2 Calbindin immunostaining analysis (**Cohorts 1 and 2**)*

For each brain, two to three images of the anterior thalamus were collected (at AP positions between -1.2 to -1.9 mm from bregma). Calbindin staining was assessed quantitatively for **Cohort 1** and qualitatively for **Cohort 2**. For quantitative analyses, the staining intensity was measured bilaterally in the anteroventral thalamic nucleus (AV) and normalised by dividing the values by the staining intensity in the adjacent periventricular anterior thalamic nucleus, which does not show lesion-induced staining alterations (data not shown). Two clusters of staining intensities were identified upon plotting the values for the Sham1 and MTTx1 groups. MTTx cases which showed AV staining (on either side) within the Sham cluster were denoted as incomplete lesions. For each case, a mean staining value for the two hemispheres was also calculated to be used in subsequent analyses. For **Cohort 2**, staining for calbindin was evaluated

independently by two investigators and cases where staining was present on either side of the brain were denoted as incomplete lesions.

4.2.6.3 Final classification of lesion cases (**Cohorts 1 and 2**)

The results of Nissl body and calbindin staining were compared and cases which were denoted as incomplete lesions with either method were subsequently excluded from the study. Three lesion cases were excluded form **Cohort 1** and three lesion cases were excluded from **Cohort 2**.

4.2.6.4 Cytochrome c oxidase densitometry analysis (**Cohort 2**)

For each brain, an average of six coronal sections were imaged in grey scale. Raw values were converted into optical density using a logarithmic function obtained by following guidelines from the National Institute of Mental Health website (Research Services Branch, National Institute of Mental Health, 2014). A normalisation procedure was carried out to minimise the effect of different levels of staining between sections, in which values for all regions of interest (as described in the following section) within each hemisphere of a coronal section were divided by the value measured from the remaining cortex (lying outside of the regions of interest) within the same hemisphere of the coronal section. As nonspecific background staining would give a value of 1, this value was subtracted from all normalized values so the final values represent a change from baseline. For each region of interest, within each subject, a single mean normalised value was calculated that represented the level of cytochrome oxidase activity, relative to the rest of the cortex.

4.2.6.5 Regions of interest for cytochrome c oxidase staining analysis (**Cohort 2**)

The regions of interest were identified in coronal sections. In the dorsal hippocampus, measurements were made within the three main subfields, i.e., dentate gyrus, CA1, and CA3, at -4.2 mm to -6.0 mm from bregma.

For the retrosplenial cortex, measures were taken from the caudal regions so that all three main subregions were present on the same coronal section. The three main subregions included granular b (Rgb), granular a (Rga), and dysgranular (Rdg) cortex (Wyss & Van Groen 1992). Measurements in the retrosplenial cortex were acquired from layer II (superficial) and layers V–VI (deep), so that a direct comparison could be made with a recent study by Mendez-Lopez et al. (2013). The identification/verification of the boundaries of these superficial and deep layers was aided by their noticeably darker staining.

4.2.7 Extraction of DTI metrics and normalisation procedures (Cohort 1)

All analyses were carried out according to protocols and Matlab scripts provided by a collaborator, Yaniv Assaf of Tel Aviv University, Israel, and using software written by Alexander Leemans (Explore DTI, Leemans et al., 2009).

4.2.7.1 Derivation of FA and MD

First, images were regularised and resampled to a resolution of 0.105 x 0.115 x 0.6 mm^3 by employing a B-cubic spline fitting algorithm. The tensor was then computed with a robust estimation algorithm. DTI images were also corrected for motion and eddy current distortions. FA and MD images were then derived from the transformed DTI maps.

4.2.7.2 Image normalisation

The next stage involved spatial normalisation of the images in SPM8 (version 8, University College London) to obtain FA and MD maps aligned with a single brain template. The template was provided by Yaniv Assaf and was derived from another study (Blumenfeld-Katzir et al., 2011).

First, for each rat, the four FA maps corresponding to the four scans in the study were registered with rigid-body transformations to the brain template.

Registered images were then averaged to create a mean FA map for each rat. The mean FA map for each rat was then used to normalise the original FA images of each rat using a 12-parametrer affine transformation. The same transformation matrix was also applied to the original MD images. Next, the normalised FA maps were again normalised but this time to the mean FA template obtained in this study (the same transformations were also applied to the MD maps). The images were then cropped to only include coronal slices present across all scans. The final anteroposterior range spanned 8.4 mm (14 slices), from +1.8 mm to -6.6 mm from bregma. Prior to statistical analyses, all images were smoothed using a Gaussian kernel of 0.6 mm.

4.2.7.3 Validation of the normalisation procedure

The success of the normalisation procedures was assessed by calculating the standard deviation of the normalised FA images and dividing it by the mean FA map.

4.2.8 Statistical analysis

4.2.8.1 Analysis of behavioural performance (**Cohort 1 and 2**)

Radial-arm maze performance was, for each cohort, evaluated with a mixed repeated-measures ANOVA with the between factor of group (Sham vs MTTx) and the within factor of block (1 block = 2 trials). The analyses were carried out using SPSS software (version 20, IBM Corporation). The alpha level was set at $p < 0.05$.

4.2.8.2 Multivoxel pattern analysis (**Cohort 1**)

The FA and MD values across the four scans were analysed on a voxel-wide basis. The values were fit into a mixed repeated-measures ANOVA model, using a Matlab script, with a between factor of group (Sham, MTTx) and the within factor of scan number (1, 2, 3, 4). Since the purpose of this study was to

specifically probe the effect of mammillothalamic tract lesions on DTI markers of structural plasticity and integrity, voxel-wide analyses output is only reported here for the interaction of group by scan number.

In addition to the 2-by-4 mixed ANOVA, simpler analyses were also performed to reveal the temporal progression of differences between the groups. The pre- and post-surgery (scans 1 and 2), post-surgery and beginning of radial-arm maze training (scans 2 and 3) and post-surgery and final radial-arm session (scans 2 and 4) timepoints were all analysed with 2-by-2 mixed ANOVAs. The results are presented as p-value maps overlaid on the mean FA template image thresholded at $p < 0.05$. No false-detection rate or multiple comparison adjustments were performed at this stage.

4.2.8.3 Region-based DTI analysis (**Cohort 1**)

Changes in FA and MD values were also tracked for specified regions of interest. This was done to inspect more closely how different areas responded to surgery and training as voxel-wide analysis produced very complex output given the four within-subject factor levels of scan. The regions of interest included the mammillothalamic tract (MTT), anterior thalamus (ATN), hippocampus (HPP) and retrosplenial cortex (RSC) based on the relevance of these structures for the pathogenesis of diencephalic amnesia (see **Introduction**). The hippocampus was further split into its dorsal (d_HPP) and ventral (v_HPP) portions while the retrosplenial cortex was split into granular (RSG) and dysgranular (RDG) portions. The outlines of the regions of interest are shown along with images of significant clusters in the **Results** section.

Mean FA and MD values in each region of interest were calculated for each animal and each scan timepoint. Three hypotheses were tested:

1) Does lesion affect the levels of FA and MD in behaviourally-naïve animals?
2) Does lesion lead to differential effects of training on FA and MD during the initial acquisition stage of the task?

3) Does lesion lead to differential effects of training on FA and MD during the final acquisition stage of the task?

The first hypothesis was tested by running a mixed repeated-measures ANOVA for each main region (MTT, ATN, RSC, HPP) with the between factor of Lesion (Sham vs MTTx) and the within factor of Scan (pre-surgery vs post-surgery; Scan 1 vs Scan 2).

The second hypothesis was tested by running a mixed repeated-measures ANOVA with the between factor of Lesion and a different within factor of Scan (pre-training vs initial training; Scan 2 vs Scan 3).

The third hypothesis was addressed by running a mixed repeated-measures ANOVA with the between factor of Lesion and another within factor of Scan (pre-training vs final training; Scan 2 vs Scan 4).

4.2.8.4 Relationship between calbindin, maze errors and DTI measures (**Cohort 1**)

To test the relationship between DTI metrics and performance on the radial-arm maze task, both measures obtained from scan number 4 were correlated with the number of errors made by the animals on the corresponding, final testing session. This was performed for all regions and subregions described above using Pearson's product-moment correlation in SPSS. The obtained *p*-values were corrected for family-wise error with a Bonferroni adjustment.

To investigate whether calbindin staining was predictive of behavioural outcome, final session errors and calbindin staining intensity were also correlated.

4.2.8.5 Cytochrome c oxidase densitometry (**Cohort 2**).

Analyses were carried out on normalised mean cytochrome oxidase optical density (O.D.) values. The means were derived by averaging the values obtained

for all the sections for each region of interest in each brain. The means were analysed using a mixed ANOVA design; different anatomical areas were grouped together, so that each ANOVA comprised related brain areas.

Analysis of the retrosplenial cortex was carried out with Lesion as between-subject factor (two levels: MTTx/Shams), while Region (three levels: Rga/Rgb/Rdg) and Layer (two levels: superficial/deep) were the within-subject factors. Analysis of the dorsal hippocampus was carried out with Lesion as a between-subject factor (two levels: MTTx/Shams), and Region as a within-subject factor (three levels: dentate gyrus/CA3/CA1). When the sphericity assumption was violated, a Greenhouse–Geisser correction was applied to the degrees of freedom. When significant interactions were found, the simple effects for each brain region were analysed as recommended by Winer (1971) using the pooled error term. Significant three-way interactions were followed up using multiple comparisons with a Bonferroni correction. The main effect of Region (and Layer in the case of the retrosplenial cortex) was not considered meaningful due to inherent differences between regions (e.g., staining levels and region size) but interactions with Lesion group are reported.

4.3 Results

4.3.1 Validation of lesion success

The success of the mammillothalamic tract lesions was assessed using Nissl-stained sections and calbindin immunoreactivity. Figure 4.3.1 displays examples of Nissl body staining while Figure 4.3.2 shows examples of calbindin staining for both cohorts. Successful lesions led to the ablation of the mammillothalamic tract at the level of probe insertion, as well as in the remaining tissue, owing to Wallerian degeneration (Coleman & Freeman, 2010). The lesions were discrete and left the nearby postcommissural fornix intact. The lesions also produced near-complete loss of calbindin immunoreactivity in the ventrolateral subdivision of the anteroventral thalamic nucleus, which was quantified for **Cohort 1** (Figure 4.3.1).
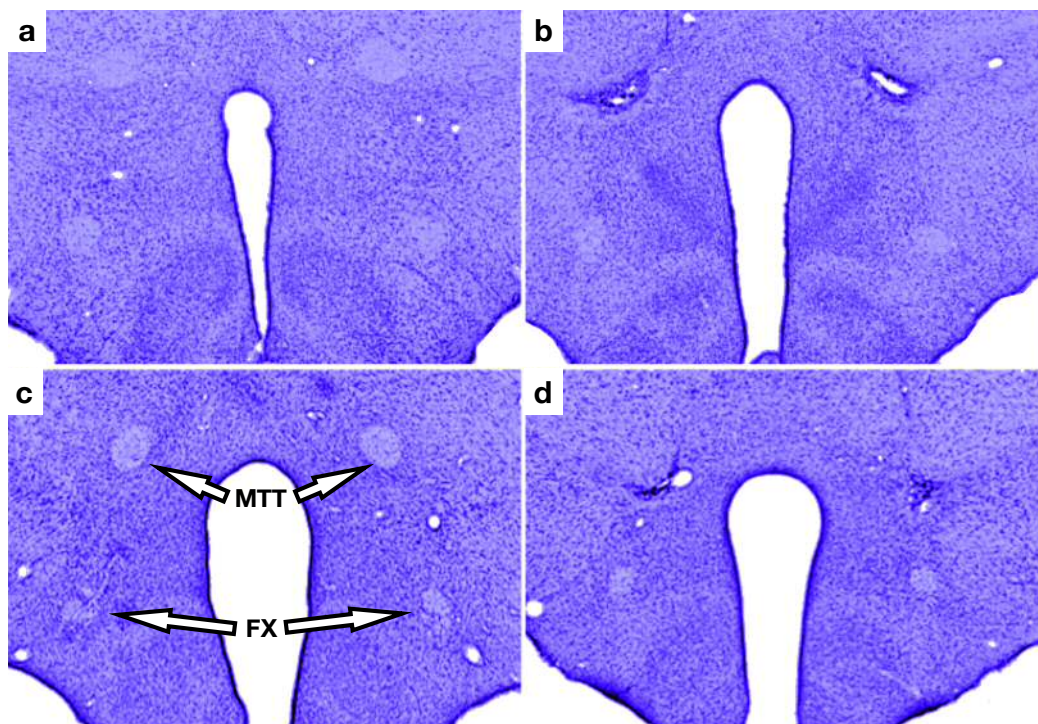
Figure 4.3.1. Nissl body staining of the ventromedial diencephalon. Panels a and c display staining in Sham cases from cohorts 1 and 2, respectively. The mammillothalamic tract (MTT) and fornix (FX) are easily discernible from the surrounding tissue. Panels b and d show examples of staining in MTTx cases from cohorts 1 and 2, respectively. Lesion led to a complete ablation of the tract, leaving a scar in its place. The adjacent fornix was left unperturbed.
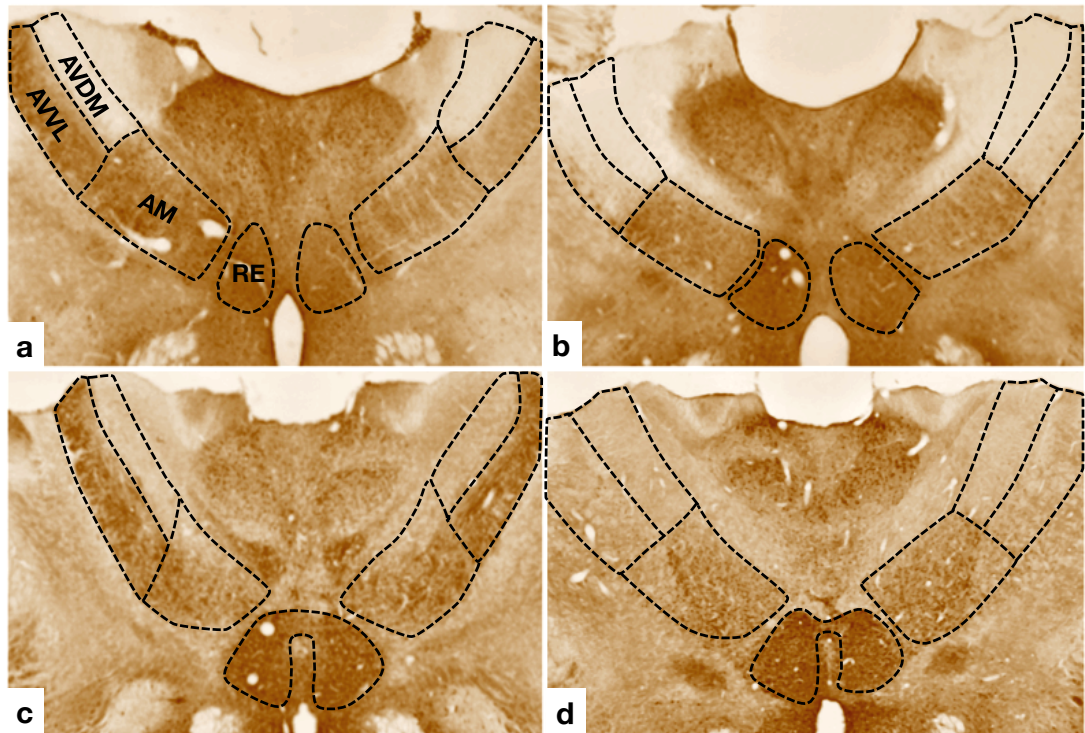
Figure 4.3.2. Calbindin immunostaining in the anterior thalamus. Panels a and c display staining in Sham cases from cohorts 1 and 2, respectively. The anteroventral thalamic nucleus shows strong staining for calbindin in its ventrolateral subdivision (AVVL) and no staining in the dorsomedial subdivision (AVDM). Panels b and d show the near-complete loss of calbindin immunoreactivity in AVVL of MTTx cases from cohorts 1 and 2, respectively. No change in calbindin staining was observed in the anteromedial (AM) and reuniens (RE) nuclei.
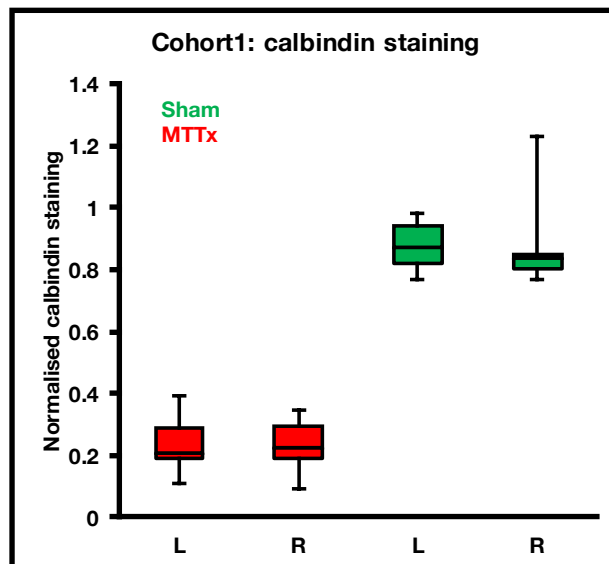
Figure 4.3.3. Box and whisker plot of normalised calbindin staining intensity in Cohort 1. The AVVL in Sham cases (in green) showed levels of staining comparable to those of the reuniens nucleus (hence normalised values just below 1). On the other hand, MTTx cases (in red) presented a near-complete loss of immunoreactivity for calbindin. The range of intensities may indicate very small amounts tract sparing in some subjects. L – left hemisphere, R – right hemisphere.

On the basis of both the Nissl and calbindin staining, 13 of the 16 lesions in **Cohort 1** and 10 of the 13 lesions in **Cohort 2**, were identified as successful, i.e., complete bilateral mammillothalamic tract lesions. The final group numbers were, in **Cohort 1**: 7 Sham cases (4 Sham cases were removed due to animal death and unrecoverable DTI data) and 13 MTTx cases; in **Cohort 2**: 10 Sham cases and 10 MTTx cases.

4.3.2 Radial-arm maze working memory performance

In both cohorts, lesioned animals made more working memory errors than control animals as reflected by the main effect of Lesion (**Cohort 1**: $F(1,18) = 29.97$, $p < 0.001$; **Cohort 2**: $F(1, 18) = 37.04$, $p < 0.001$)(Figure 4.3.4). Training led to improved performance in both cohorts (main effect of Block; **Cohort 1**: $F(15, 270) = 2.20$, $p = 0.007$; **Cohort 2**: $F(8, 144) = 8.31$, $p < 0.001$) with Sham animals showing a greater decrease in errors over time (Lesion by Block interaction; **Cohort 1**: $F(15, 270) = 2.15$, $p = 0.008$; **Cohort 2**: $F(8, 144) = 4.06$, $p < 0.001$).
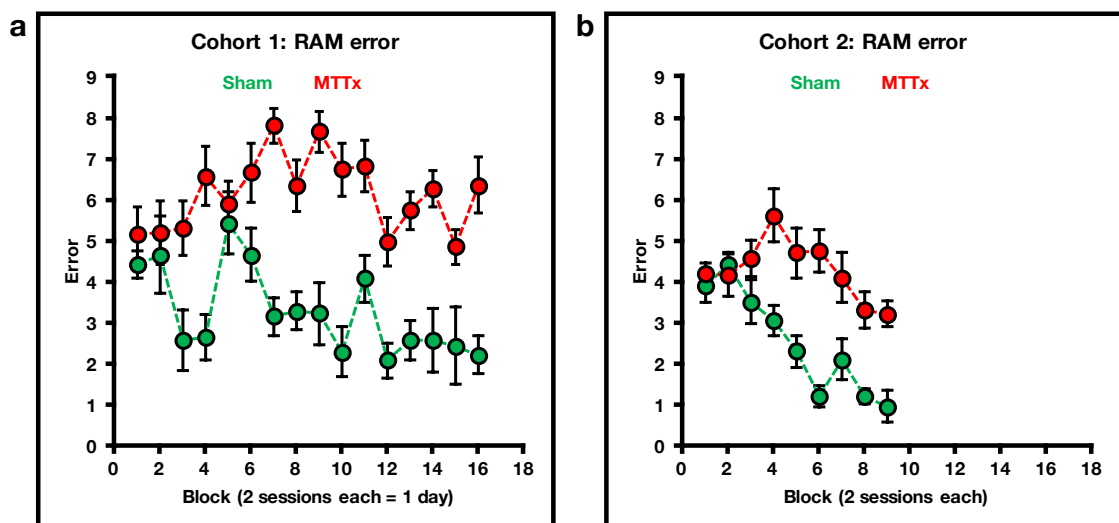
Figure 4.3.4. Radial-arm maze performance for Cohorts 1 (panel a) and 2 (panel b). Both cohorts showed higher error scores in lesioned animals (in red) and the rate of improvement on the task was greater for Sham animals (in green) in both cohorts.

4.3.3 Validation of DTI regularisation and normalisation procedures (Cohort 1)

Figure 4.3.5 displays maps obtained by dividing the standard deviation for all analysed fractional anisotropy voxels by their mean. Overall, very few voxels displayed substantial departures from mean, with highest standard deviation/mean ratio of 34% observed in parts of the dorsal hippocampus and in the amygdaloid complex.
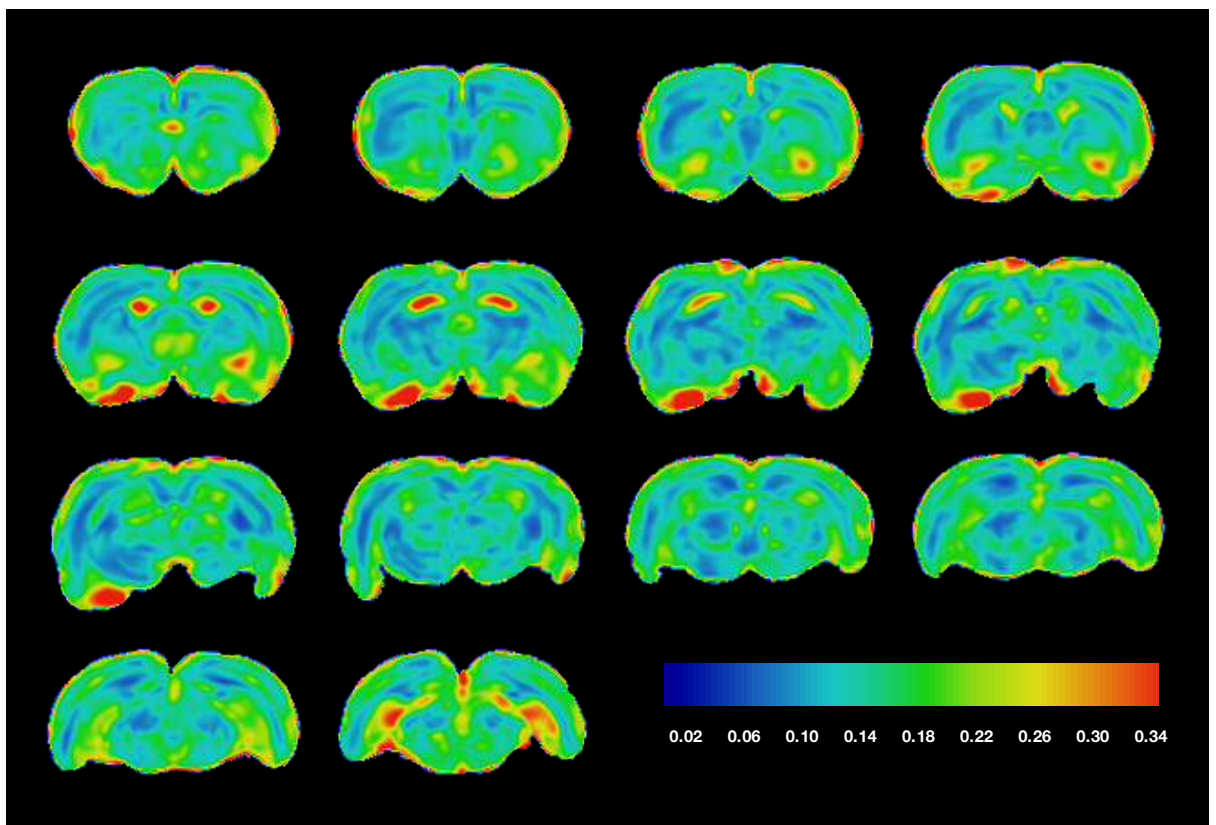
Figure 4.3.5. Validation of regularisation and spatial normalisation procedures. The images show standard deviation divided by the mean for all analysed fractional anisotropy voxels. It is apparent that for most of the brain, there was very little variability in voxel values.

4.3.4 Voxel-wide analyses of DTI measures (Cohort 1)

The results below are reported for the interaction of the Lesion and Scan number factors only. As such, they represent differential Lesion effects on FA and MD values induced by all conditions across the study (scans 1-4), surgery (scans 1 and 2), initial training (scans 2 and 3) or final training (scans 2 and 4). They do

not, however, indicate the overall pattern of FA and MD changes, which will be addressed for specified regions of interest in the subsequent section (**Region-based analyses of DTI measures**).

4.3.4.1 Fractional anisotropy

A 2-by-4 interaction of Lesion with four levels of Scan reached significance levels for many voxels throughout the brain (**Error! Reference source not found.**). These included, among large white matter fibres, the corpus callosum, cingulate bundle, fornical fimbriae and the mammillothalamic tract. Among cortical regions, differential values were found for example in the anterior cingulate, motor, somatosensory, visual and retrosplenial cortices. Other areas of prominent clusters included the anterior thalamus, dorsal hippocampus, the hypothalamic region, amygdaloid complex and certain midbrain areas.

Considering simpler analyses by 2-by-2 ANOVAs demonstrated the contributions of different stages of the study to the pattern observed for the compound 2-by-4 ANOVA. Following surgery, Sham and MTTx cases showed most striking interaction clusters in the anterior thalamus, dorsal hippocampus and the hypothalamic region, including the mammillothalamic tract. Upon initial radial-arm training, the pattern of clusters largely shifted toward cortical areas, especially the retrosplenial cortex. Finally, upon reaching the last training session, areas of differential FA values still included the retrosplenial cortex (to a lesser degree) but were most striking for the motor cortex, striatum and the sensory thalamus.

4.3.4.2 Mean diffusivity

Mean diffusivity showed fewer but larger interaction clusters compared to fractional anisotropy results (Figure 4.3.6). The 2-by-4 compound interaction revealed most notably the anterior thalamus, dorsal and ventral hippocampus, mammillothalamic tract and ventricular areas. The latter may simply reflect the shrinkage of brain tissue following lesion.

Subsequent analyses revealed that most differential changes between Sham and MTTx cases could be attributed to the pre-post-surgery comparison. On the other hand, remaining ANOVAs produced fewer, smaller and less significant interaction clusters, save for parts of the ventral hippocampus and the sensory thalamus upon the initial task acquisition stage.

4.3.5 Region-based analyses of DTI measures (Cohort 1)

Region-based analyses were carried out to reveal the overall progression of changes in the FA and MD values. Four main regions of interest were selected: the mammillothalamic tract (MTT), anterior thalamus (ATN), retrosplenial cortex(RSC) (including the distinction between its granular, RSG, and dysgranular, RDG, subdivisions) and the hippocampus (HPP) (including the distinction between its dorsal, D_HPP, and ventral, V_HPP, subdivisions).

4.3.5.1 Fractional anisotropy

The only analysed region which showed a main effect of Lesion was the mammillothalamic tract, with higher FA values in Sham ($F(1,18) = 20.61$, $p < 0.001$)(Figure 4.3.7). The effect of Lesion showed dependence on the stage of the study, as reflected by the interaction between Lesion and Scan number ($F(3, 37.93) = 6.54$, $p = 0.003$). FA values displayed a large decrease following surgery in MTTx but not in Sham animals (-15% in MTTx animals compared to -2% in Sham cases). On the other hand, the initial task acquisition scan saw a marked increase in the FA value for the Sham group, which remained high until the end of the study, and further widened the gap between the groups.
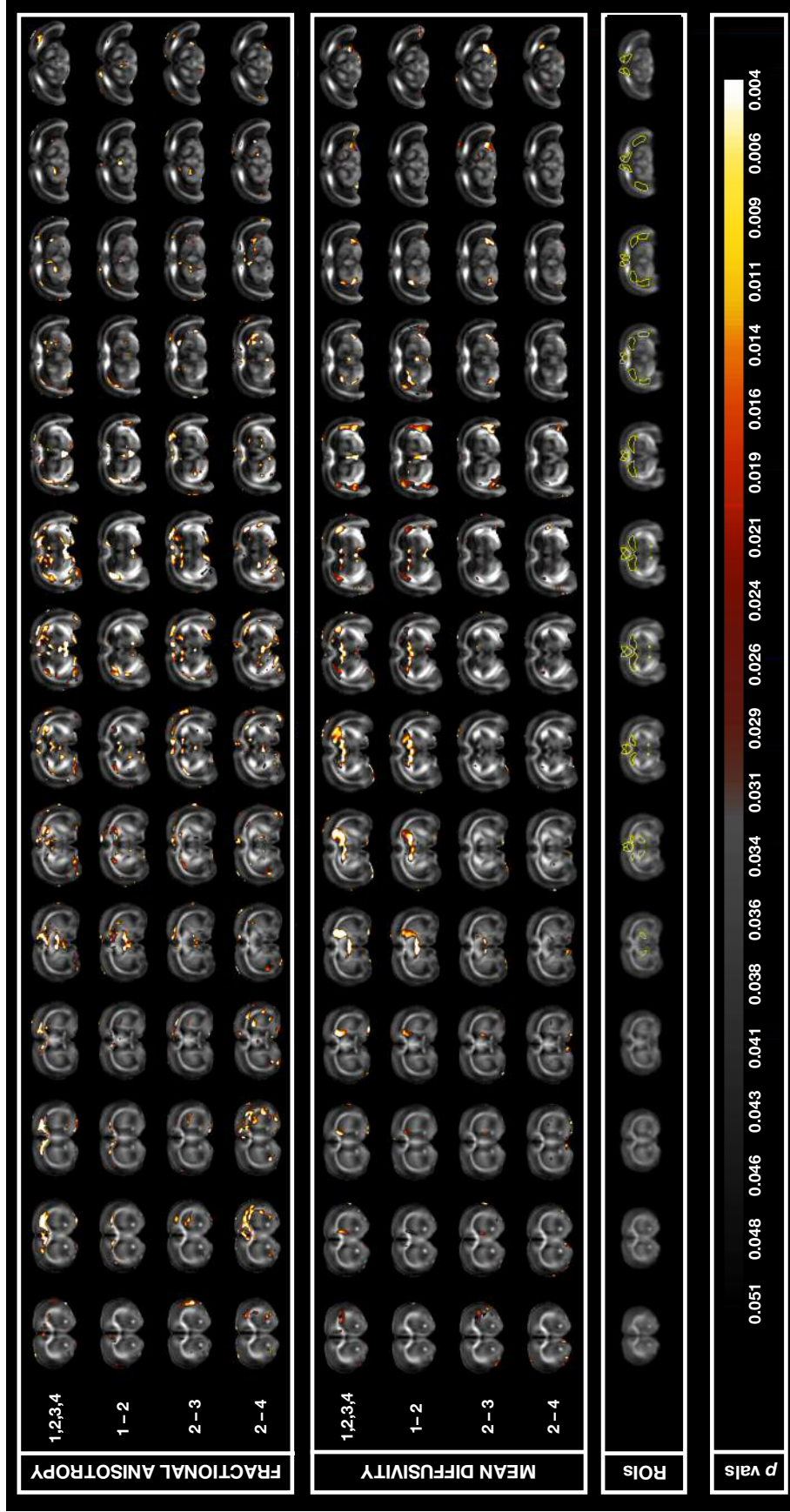
Figure 4.3.6. Result of voxel-wide ANOVA analyses for Sham and MTTx FA and MD values. The first two panels display *p*-values, thresholded to α = 0.05, overlaid on top of the mean FA template, for the FA and MD measures, respectively. The third panel shows the regions of interest (ROIs) employed in the regional analysis of changes in the DTI metrics. The final panel displays the colour-scale for p-values (p vals) in panels one and two. Within the first two panels, each row represents a different ANOVA procedure: the interaction between Lesion and Scan throughout the study (1, 2, 3, 4); the interaction between Lesion and Scan of pre- and post-surgery (1 – 2); the interaction between Lesion and Scan of post-surgery and initial training (2 – 3) and, finally, the interaction between Lesion and Scan for initial training and final training sessions (2 – 4).

The retrosplenial cortex and anterior thalamus displayed a main effect of Scan number (RSC: F(3, 54) = 31.17, p < 0.001; RSG: F(3, 54) = 27.16, p < 0.001; RDG: F(3, 54) = 21.84, p < 0.001; ATN: F(3, 54) = 21.19, p < 0.001) while the hippocampus did not show a significant effect of Scan (including when considered as dorsal and ventral hippocampal areas). Nevertheless, there appeared to be a trend for the initial training to induce higher FA values in the retrosplenial cortex (8% increase in Sham animals and a 3% increase in the MTTx animals) as well as in the hippocampus (7% in Sham animals and 0% in MTTx animals). The anterior thalamus displayed a steady decrease in FA values until the final scan timepoint in both groups, when Sham values returned to baseline whereas MTTx values showed no recovery (paired t-test between Scan 1 and Scan 4 values, $p = 0.026$).

4.3.5.2 Mean diffusivity

The pattern of mean diffusivity changes was similar across all regions analysed (Figure 4.3.8).In general, in both Sham and MTTx cases, surgery led to an increase in MD values. This was followed by a decrease in MD values throughout learning of the working memory task. All regions analysed displayed a main effect of Scan number (MTT: F(3, 54) = 7.22, $p < 0.001$; RSC: F(3, 54) = 9.72, $p < 0.001$; RSG: F(3, 54) = 4.32, $p = 0.008$; RDG: F(1, 54) = 19.14, $p < 0.001$; HPP: F(3, 54) = 23.98, $p < 0.001$; D_HPP: F(1.95, 35.07) = 25.30, $p < 0.001$; V_HPP: F(3, 54) = 14.03, $p < 0.001$; ATN: F(3, 54) = 24.23, $p < 0.001$).

Furthermore, in all regions but the retrosplenial cortex, MTTx animals showed higher overall MD values (main effect of Lesion; MTT: F(1, 18) = 9.33, $p = 0.007$; HPP: F(1, 18) = 15.00, $p = 0.001$; D_HPP: F(1, 18) = 16.22, $p < 0.001$; V_HPP: F(1,18) = 7.43, $p = 0.014$, ATN: F(1, 18) = 18.09, $p < 0.001$). Finally, Lesion showed an interaction with Scan number in the hippocampal and anterior thalamic areas (Lesion by Scan interaction; HPP: F(3, 54) = 3.01, $p = 0.38$; D_HPP: F(1.95, 35.07) = 3.43, $p = 0.045$; ATN: F(3, 54) = 3.81, $p = 0.015$).
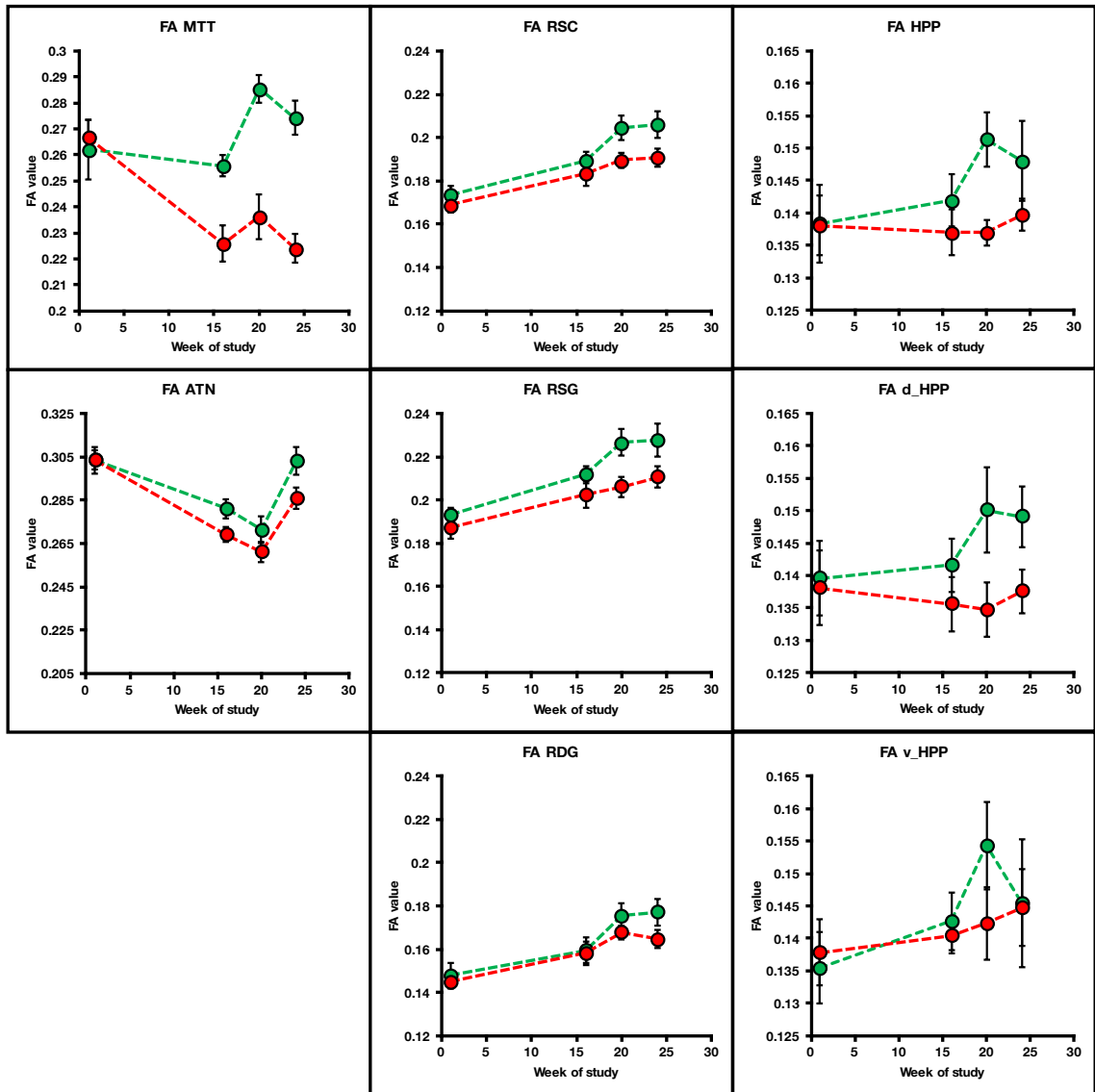
Figure 4.3.7. Changes in FA values among selected regions of interest. The x axis represents the timeline of the study with week 1 at scan number 1. Sham animals are shown in green and MTTx animals, in red. MTT – mammillothalamic tract, RSC – retrosplenial cortex, RSG – granular subdivision of the retrosplenial cortex, RDG – dysgranular subdivision of the retrosplenial cortex, HPP – hippocampus, D_HPP – dorsal subdivision of the hippocampus, V_HPP – ventral subdivision of the hippocampus.
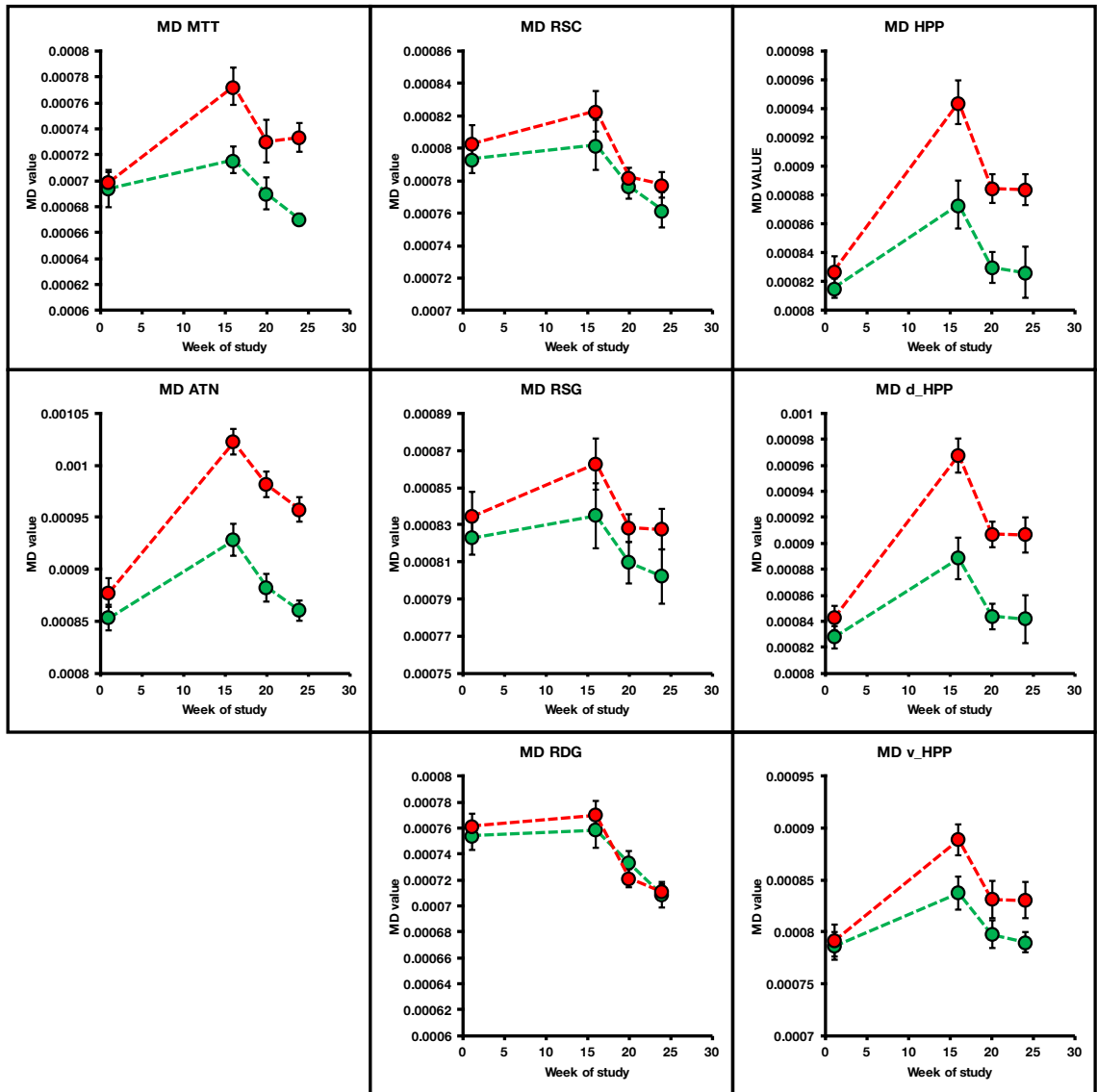
Figure 4.3.8. Changes in MD values among selected regions of interest. The x axis represents the timeline of the study with week 1 at scan number 1. Sham animals are shown in green and MTTx animals, in red. MTT – mammillothalamic tract, RSC – retrosplenial cortex, RSG – granular subdivision of the retrosplenial cortex, RDG – dysgranular subdivision of the retrosplenial cortex, HPP – hippocampus, D_HPP – dorsal subdivision of the hippocampus, V_HPP – ventral subdivision of the hippocampus.

.

4.3.5.3 Relationship between calbindin staining and the number of working memory errors

It was further investigated whether there existed a relationship between the level of calbindin staining and the number of working memory errors made on the final testing day. A moderate negative trend was found for MTTx animals (r = -0.49, p = 0.09) while no relationship was apparent for the Sham animals (Figure 4.3.9).
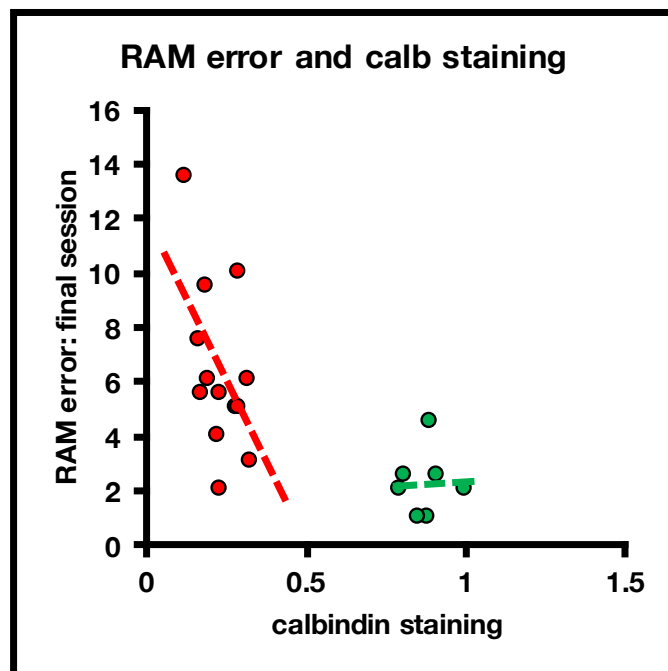
Figure 4.3.9. The relationship between errors on the final behavioural testing session and the level of calbindin staining in the anterior thalamus. A negative trend was observed for MTTx animals (in red) and no relationship was present for Sham animals (in green).

4.3.5.4 Relationship between working memory errors and FA and MD values

Multiple correlations were performed to probe whether FA and MD metrics were predictive of the performance of animals either during initial task acquisition (session 2, scan 3) or at the end of training (session 16, scan 4). Following family-wise error correction using the Bonferroni method, only one brain region displayed a link between a DTI measure and behaviour. A strong, negative relationship was found between the FA values in the retrosplenial cortex and maze errors for the MTTx group on the final testing session (Table 4.3.1 and Figure 4.3.10a)(r = -0.67, p = 0.04). Additionally, the hippocampus of Sham

animals showed a negative trend between the number of errors during initial task acquisition and MD (Table 4.3.1 and Figure 4.3.10b)(HPP: r = -80, *p* = 0.08; D_HPP: r = -0.79, *p* = 0.09).

Table 4.3.1. Multiple correlations between FA and MD values and working memory errors on the second and sixteenth sessions of radial-arm maze training. Only one correlation survived multiple comparison correction (highlighted in yellow) while two regions displayed a trend (highlighted in orange). r – Pearson's correlation coefficient, adj. p – p value after Bonferroni adjustment, RSC – retrosplenial cortex, RSG – granular subdivision of the retrosplenial cortex, RDG – dysgranular subdivision of the retrosplenial cortex, HPP – hippocampus, D_HPP – dorsal subdivision of the hippocampus, V_HPP – ventral subdivision of the hippocampus.

		Sham				MTTx			
		2nd SESSION		16th SESSION		2nd SESSION		16th SESSION	
		r	adj. *p*	r	adj. *p*	r	adj. *p*	r	adj. *p*
FA	RSC	-0.17	1.00	0.03	1.00	-0.22	1.00	**-0.67**	**0.04**
	RSG	0.02	1.00	0.06	1.00	-0.11	1.00	-0.59	0.12
	RDG	-0.38	1.00	-0.01	1.00	-0.37	0.83	-0.60	0.12
	HPP	-0.08	1.00	0.24	1.00	-0.23	1.00	-0.52	0.27
	D_HPP	-0.08	1.00	0.27	1.00	-0.37	0.81	-0.50	0.30
	V_HPP	-0.05	1.00	0.13	1.00	0.04	1.00	-0.29	1.00
	ATN	-0.23	1.00	-0.02	1.00	0.28	1.00	0.05	1.00
	MTT	0.06	1.00	-0.24	1.00	0.18	1.00	0.17	1.00
MD	RSC	0.13	1.00	-0.38	1.00	-0.54	0.22	0.31	1.00
	RSG	-0.07	1.00	-0.42	1.00	-0.42	0.59	0.20	1.00
	RDG	0.39	1.00	-0.14	1.00	-0.44	0.52	0.48	0.38
	HPP	**-0.80**	**0.08**	-0.28	1.00	0.12	1.00	-0.13	1.00
	D_HPP	**-0.79**	**0.09**	-0.33	1.00	0.15	1.00	-0.08	1.00
	V_HPP	-0.27	1.00	-0.14	1.00	0.01	1.00	-0.18	1.00
	ATN	-0.05	1.00	-0.67	0.33	-0.04	1.00	0.33	1.00
	MTT	0.08	1.00	0.02	1.00	-0.19	1.00	-0.13	1.00
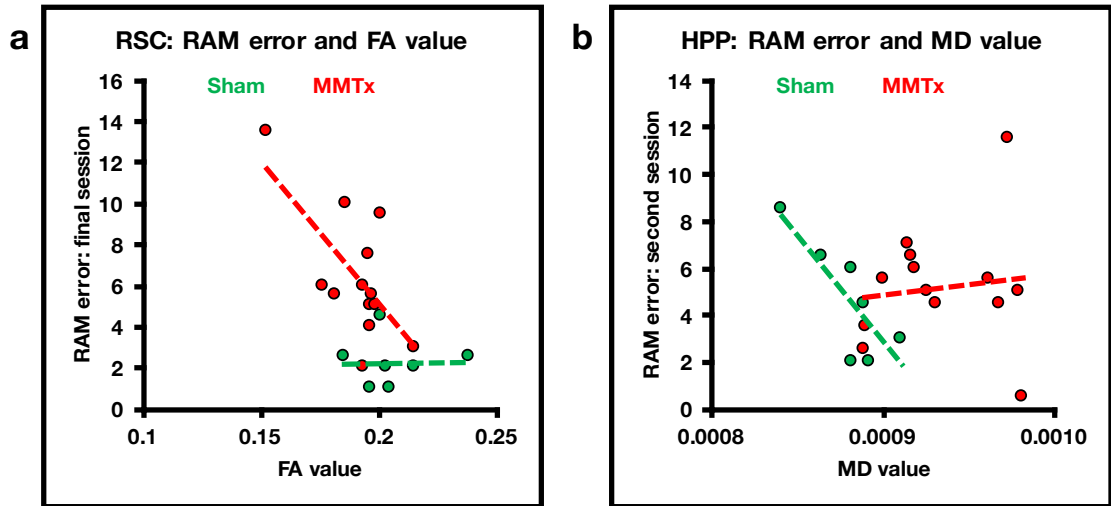
Figure 4.3.10. The relationship of maze errors and DTI measures. Panel a displays the errors on the final training session and FA values measured in the retrosplenial cortex (RSC) while panel b shows errors made on the second training session and the MD values measured in the hippocampus (HPP).

4.3.6 Cytochrome c oxidase staining (Cohort 2)

Within the gray matter, the cytochrome oxidase DAB reaction produced dark staining of the neuropil and, to a lesser extent, cell bodies. The retrosplenial cortex showed alternating bands of high and low intensity, which clearly delineated the borders between layers I, II, III–IV and V–VI; and generally a higher level of staining compared to the adjacent regions of the secondary visual cortex and the dorsal subiculum (Figure 4.3.11). The layers of the hippocampus also displayed an alternating pattern of high and low intensity staining with strong label in stratum oriens of CA1 and CA3 and the molecular layer of the dentate gyrus.

4.3.6.1 Dorsal hippocampus

The MTT lesions did not affect overall hippocampal cytochrome oxidase staining (F<1) and there were no significant regional differences in the effect of lesion (F(1.52, 27.37) = 3.30, p = 0.064) (Figure 4.3.12c).

4.3.6.2 Retrosplenial cortex

In the retrosplenial cortex, MTT lesions produced an overall reduction in cytochrome oxidase staining, reflected by a main effect of Lesion ($F_{(1,18)} = 8.11$, $p = 0.011$). Furthermore, there was a significant three-way Lesion-by-Region-by-Layer interaction ($F_{(2,36)} = 15.91$, $p < 0.001$). Subsequent analyses revealed significant decreases in the deep layers of the granular retrosplenial cortex (Rga and Rgb both $p < 0.001$) and the superficial dysgranular layer ($p = 0.027$; Figure 4.3.12 a&b).
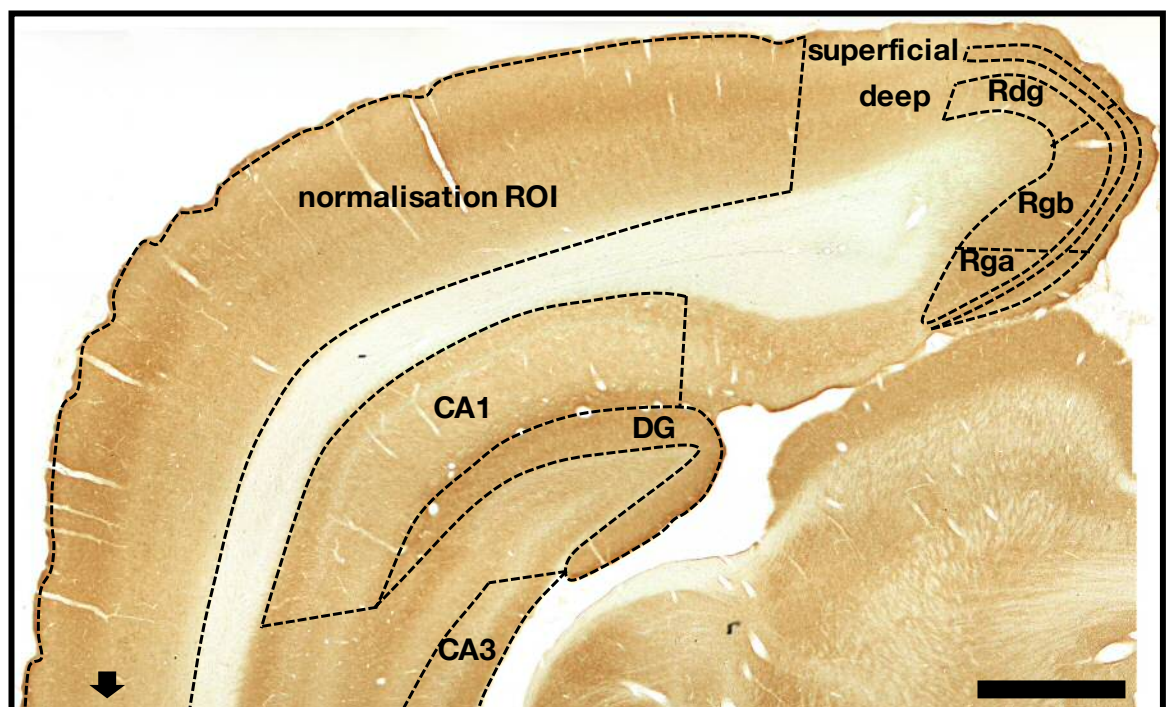
Figure 4.3.11. Representative image of cytochrome oxidase staining in coronal brain slices. Dashed lines denote the extent of the regions of interest based on Wyss & Van Groen (1992). Note that the normalization ROI extends beyond the border of the photograph. DG, dentate gyrus; Rga, retrosplenial granular a cortex; Rgb, retrosplenial granular b cortex; Rdg, retrosplenial dysgranular cortex; ROI, region of interest. Scale bar = 1 mm.
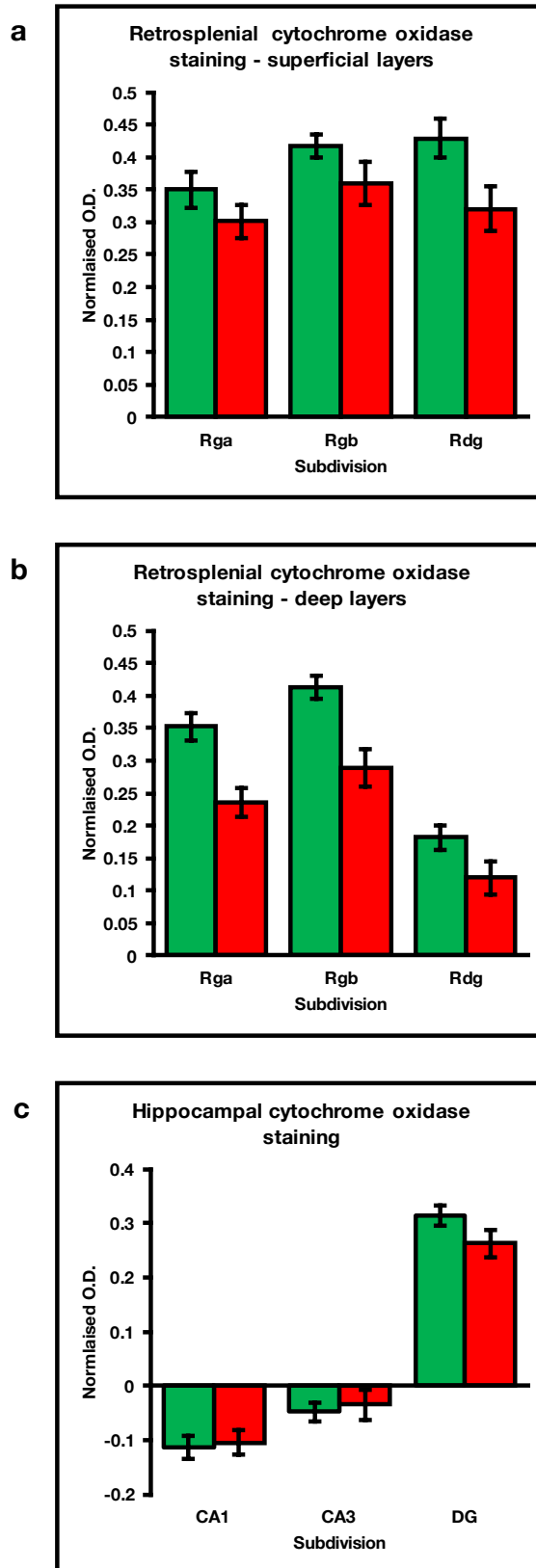
Figure 4.3.12. Quantification of cytochrome oxidase staining. A – staining within the superficial layers of the retrosplenial cortex, b – staining within the deep layers of the retrosplenial cortex, c – staining within the hippocampus. Green bars represent Sham cases and red bars, MTTx animals. The error bars are the standard error of the mean. Abbreviations as in the figure before.

4.4   Discussion

Mammillothalamic tract lesions produce memory impairments in both rodents and humans, yet it is still not clear why damage within this region is so disruptive. In the present set of experiments, mammillothalamic tract lesions in rats led to widespread alterations in water diffusivity as well as to reduced levels of the metabolic marker cytochrome oxidase in the retrosplenial cortex. Lesions also caused a similar degree of spatial working-memory impairment in both animal cohorts, replicating results of previous studies and reiterating the debilitating effects of disruption to the Papez circuit.

4.4.1   Widespread changes of DTI metrics following mammillothalamic tract lesions

Multivoxel pattern analysis of DTI metrics revealed alterations in many brain regions consistent with a network-level disruption following mammillothalamic tract lesions. Differences in FA values were most striking for large white matter bundles, including the mammillothalamic tract itself, the corpus callosum, cingulate bundle and fimbriae of the fornix. Grey matter differences were observed in the anterior thalamus, dorsal hippocampus, ventral diencephalon and at multiple cortical sites including the anterior cingulate, motor, somatosensory, visual and retrosplenial cortices. Differential MD values were found in fewer brain regions, predominantly the mammillothalamic tract, anterior thalamus and parts of the hippocampus. Overall, this widespread pattern of differential changes accords with the concept of 'covert' pathology affecting multiple components of the Papez circuit in models of diencephalic amnesia (Vann & Albasser, 2009)(also see below the discussion of immediate-early gene and cytochrome oxidase changes following lesions).

4.4.2 The effect of lesion and training on the differential patterns of FA and MD

To further understand the results it was necessary to consider the contribution of lesion and training to the observed differences. Differential FA and MD values due to lesion alone (pre-post lesion comparison) were present primarily within the anterior thalamus, hippocampus and the hypothalamic region, including the mammillothalamic tract. Training did not lead to major differences in MD values beyond those caused by lesion, except for parts of the ventral hippocampus and the sensory thalamus. On the other hand, the differential patterns of FA shifted toward cortical regions, including the retrosplenial cortex, following initial training, and the motor cortex, striatum and sensory thalamus upon the final testing session.

Taken together, it would appear that the MD metric was most sensitive to the effect of lesion while the FA metric showed sensitivity to lesion in subcortical areas and sensitivity to learning in parts of the cortex. Alterations following lesion may represent damage-induced restructuring of the tissue, such as deafferentation and reduced structural plasticity. Wallerian degeneration following transection of white matter fibres is characterised by cytoskeletal dissolution, tissue contraction, fragmentation of myelin and gliosis, all of which can, in principle, affect the overall (MD) and directional (FA) movement of water (Coleman & Freeman, 2010). In the clinic, transection of the mammillothalamic tract in amnesic patients can be detected using diffusion-weighted MRI imaging (e.g., Yoneoka et al., 2004), which is based on similar principles to DTI. Additionally, lesions of the anterior thalamus have been shown to produce reduced spine density in the CA1 and retrosplenial cortex (Harland et al., 2014) and mammillothalamic tract lesions may cause a similar effect (in the CA1 but not in the retrosplenial cortex)(Perry et al., unpublished results). The differential changes in cortical areas, striatum and sensory thalamus upon training may, on the other hand, reflect learning-induced plasticity (see **Introduction** to this chapter). The involvement of the retrosplenial cortex would be consistent with its role in navigation, and more broadly, spatial memory, which are known to rely

on short-term and long-term plastic changes (see the introduction to this chapter as well as **Chapters 2** and **3**). Conversely, differential FA values observed in the striatum, motor cortex and sensory thalamus may represent overall higher activity of lesioned animals, which made more arms visits than Sham animals (as they made more mistakes) at the end of training but not during initial task acquisition (when both groups were relatively naïve to the task).

4.4.3 Region-based analyses reveal the timecourse of FA and MD changes

Region-based analyses were carried out to track the temporal progression of FA and MD changes at brain sites previously identified in the pathogenesis of diencephalic amnesia. In both animal groups (Sham, MTTx), surgery produced higher MD values, which subsequently decreased during the course of learning. It is impossible to say whether this pattern reflects the effect of training or perhaps was simply dependent on time post-surgery. Significant differences between the two groups were found in all brain regions analysed save for the retrosplenial cortex.

On the other hand, the mammillothalamic tract was the only region displaying FA differences between Sham and MTTx animals. Lesion led to a large reduction in mammillothalamic FA while training led to its increase, which was much greater in Sham animals. At the end of the study, Sham FA values were higher than during the first scan while MTTx rats displayed a large depression of FA compared to baseline. The anterior thalamus saw a progressive decrease in FA values in both groups, which eventually returned to baseline for Sham animals but not for MTTx animals. Finally, the retrosplenial cortex and hippocampal area showed a trend towards higher FA values in Shams during initial training, which did not, however, reach significance.

The lack of statistically-significant region-level differences for the FA and MD values may be a genuine effect, however, voxelwise analyses suggest otherwise. It is possible that significant clusters described above (section **4.3.4**) identified

sub-anatomical differences, which were not explicitly tested in region-based analyses (as precise delineation of such sub-regions would have been difficult). Moreover, the small number of animals in the study (especially Sham cases) might have led to the issue of insufficient power.

4.4.4 Relationship between DTI metrics and behavioural performance

Among all regions analysed, only the retrosplenial cortex displayed a (negative) relationship between a DTI metric and the number of radial-arm maze errors. Furthermore, this was only the case for MTTx animals and only for the final testing session. The implication is that lower FA values were linked to worse behavioural performance, which may be both a reflection of the detrimental lesion-induced damage (see above) as well as an effect of the lack of emergence of 'positive' plastic changes required for the expression of memory (see **Chapter 2**). In contrast to other studies of spatial working-memory, however, Sham animals did not exhibit relationships with either of the metrics save for a (negative) trend between the MD value and radial-arm maze error in the hippocampus during initial task acquisition.

A possible explanation for the overall lack of the relationship between Sham performance and the FA and MD values could be that of methodological nature. While previous studies employed relatively short training protocols (Blumenfeld-Katzir et al., 2011; Hofstetter & Assaf, 2017; Sagi et al., 2012), radial-arm training in the current study lasted for a period of about a month. The long duration of training was motivated by the need to allow for behavioural differences between the groups to reach maximum levels. For that reason, scanning Sham animals at the beginning of training, when they were relatively naïve to the task (session number 2) and at the end of the study (when they reached asymptotic performance) might have led to ceiling and floor effects, respectively. On the other hand, MTTx animals never fully mastered the task and could therefore present a relationship between DTI metrics and behaviour.

4.4.5 Comparison of the observed changes in FA and MD with studies of other neurological conditions

Multiple studies have also identified widespread changes to white matter FA values, grey matter MD values and grey matter density within the limbic-diencephalic network of Alzheimer's Disease patients (Acosta-Cabronero & Nestor, 2014). Typically, white matter FA values are found to be decreased while MD values are found to be higher. For example, reduced FA values were found in the splenium of the corpus callosum concurrent with a reduction of retrosplenial volume and metabolic activity, which was predictive of the severity of memory impairment in patients (Pengas et al., 2012). A large multicentre MRI study of 137 Alzheimer's Disease patients and 143 healthy controls also identified widespread alterations in the two DTI metrics. It reported increased white matter MD values within the entire temporal lobe, corpus callosum, cingulate bundle and prefrontal areas. On the other hand, FA values were seen diminished in the corpus callosum, fornix, temporal lobe, precuneus and cingulate gyrus (Teipel et al., 2012). Other syndromic diseases, such as schizophrenia, also present widespread decreases in FA white matter associated with adjacent reduced grey matter volume (Douaud et al., 2007). The reduction of FA values in the fornix was shown to correlate with the degree of episodic memory impairment of schizophrenic patients (Nestor et al., 2007). Similar changes to fornical FA have also been reported in Korsakoff's Syndrome sufferers (Nahum et al., 2015).

4.4.6 What do FA and MD metrics reveal about disease?

Altogether, studies suggest that reductions in FA and increases in MD may be linked to pathological changes in a number of conditions. However, little is known about precisely what physiological changes underlie alterations in the DTI metrics. While experiments in rodents indicate a possible involvement of plasticity (see above), the overall picture remains clouded. Increases in FA of the grey matter were reported in animal models of traumatic brain injury and found to correspond to the development of gliosis (Budde et al., 2011)(hence increased

cortical FA would indicate pathology) while reduced callosal FA was found to correlate with the loss of white matter integrity. Similarly, radiation therapy in cancer patients transiently induces a decrease in MD and an increase in FA within the temporal lobe, which is thought to reflect tissue oedema, gliosis and mitochondrial swelling, potentially leading to memory dysfunction in patients (Wang et al., 2016). On the other hand, a thiamine deficiency model in the rat displayed decreased FA within the thalamus (one of the primary sites of pathology in Korsakoff's Syndrome) as well as increases in FA in the cortex (Dror et al., 2009). In the current study, both thalamic and cortical FA values were found to be slightly reduced for the MTTx animals, which did not reach significance in region-based analyses but was identified in the interactions of multivoxel pattern analysis. The temporal pattern of FA changes showed an overall effect of surgery leading to reduced FA values in the anterior thalamus and an overall increase in cortical FA values in both groups. It could, therefore, be the case that surgery itself, i.e. placement of the radiofrequency probe, produced FA alterations irrespective of lesion, which followed the pattern seen in the thiamine deficiency rat model.

4.4.7 Mammillothalamic lesions led to a decrease in retrosplenial cytochrome oxidase staining

Lesions of the mammillothalamic tract produced a decrease in the staining for cytochrome oxidase in the retrosplenial cortex but not in the dorsal hippocampus. Furthermore, changes were found both in the superficial and deep layers of the retrosplenial granular and dysgranular subregions. A very similar pattern was reported alongside these results for the immediate-early gene *Zif268* in our recent publication (Frizzati et al., 2016), despite the fact that staining for the two markers was carried out on tissue from two different cohorts of rats. Together, the results presented here and the complementary finding of *Zif268* reduction are consistent with changes in both markers reflecting underlying hypometabolism within the retrosplenial cortex. These findings further demonstrate the importance of ascending mammillary projections for retrosplenial function and reveal that retrosplenial dysfunction does not simply

reflect thalamic deafferentation as mammillothalamic tract lesions would only indirectly affect the retrosplenial cortex. The changes in the levels of cytochrome oxidase can be additionally compared to the expression of *c-fos* (Vann & Albasser, 2009), which was measured in the same cohort as *Zif268*. Lesions resulted in more pronounced changes in retrosplenial *c-fos* expression, especially in the more superficial layers; for example, *c-fos* expression was reduced by about 70% in the superficial layers of granular b (Vann & Albasser, 2009) compared to a 27% reduction in *Zif268* and a 14% reduction in cytochrome oxidase. The degree of change in the deeper retrosplenial layers was more comparable across the three different markers. However, in contrast to the *Zif268* and cytochrome oxidase findings, lesions also reduced *c-fos* expression in the dorsal hippocampus (see also Vann, 2013).

Similar to the results found with *c-fos*, mammillothalamic tract lesions (and more general diencephalic lesions) can also reduce the levels of hippocampal acetylcholinesterase (Savage et al., 2003; Winter et al., 2011). Therefore, it seems that although retrosplenial hypoactivity following mammillothalamic tract lesions appears constant across markers, the hippocampal effects are much more varied; some markers are reduced across all hippocampal subfields while other measures of activity indicate that the hippocampus is functionally "normal", despite animals showing clear memory deficits. The effect of diencephalic lesions on hippocampal function is clearly multifaceted and may well reflect both the activity marker under investigation (e.g., Barry, Coogan & Commins, 2016) and the sensitivity of the behavioural task.

4.4.8 Why do lesions of the mammillothalamic tract produce deficits in memory?

The mammillothalamic tract carries projections from the mammillary bodies to the anterior thalamic nuclei and nearly all neurons within the mammillary bodies are thought to contribute fibres to the mammillothalamic tract (Cruce, 1975; Takeuchi, Allen & Hopkins, 1985; Vann, Saunders & Aggleton, 2017). The mammillothalamic tract lesions in the present study disconnected the

projections from the medial mammillary nuclei to the anteromedial and anteroventral thalamic nuclei while leaving the projections from the lateral mammillary nuclei largely intact (Vann & Albasser, 2009). The use of anti-calbindin immunohistochemistry in the present study also confirmed that the medial mammillary projections to the anterior thalamic nuclei had been successfully disconnected. Moreover, in **Cohort 1** (DTI study), radial-arm maze errors on the final training session displayed a negative trend with the level of calbindin staining, indicating, the perhaps minute sparing of the tract allowed animals to preform slightly better (yet still at much lower levels than Sham animals). It has been proposed that there are at least two separate systems within the mammillary bodies, comprising the lateral and medial nuclei (Dillingham, et al., 2015). The lateral mammillary nuclei form part of a head-direction system whereas the medial mammillary nuclei are part of a proposed ''theta" system (Vann & Aggleton, 2004). It appears that the medial mammillary nuclei are more important for mnemonic function, with lateral mammillary nuclei lesions producing only mild and transient impairments on tests of spatial memory (Harland et al., 2015; Vann, 2005).

4.4.9 Comparison with lesions of the anterior thalamus

Given that the mammillothalamic tract lesion effects are most likely mediated via the anterior thalamic nuclei, and the anteroventral and anteromedial thalamic nuclei in particular, comparisons with findings from anterior thalamic lesions become especially pertinent. The effects of both unilateral and bilateral anterior thalamic lesions on retrosplenial and hippocampal activity have been assessed using a number of markers of activity, including *c-fos*, *Zif268* and cytochrome oxidase. Overall, the pattern is remarkably similar to what is found with mammillothalamic tract lesions. Expression of *c-fos* is typically reduced in both the retrosplenial cortex and hippocampus (Jenkins et al., 2002; Poirier & Aggleton, 2009) whereas *Zif268* changes are restricted to the retrosplenial cortex (Dumont et al., 2012; Poirier & Aggleton, 2009). In the same way, anterior thalamic lesions reduce the levels of cytochrome oxidase in the retrosplenial cortex but not in the hippocampus (Mendez-Lopez et al., 2003). Given the

similarity in changes following anterior thalamic and mammillothalamic tract lesions, it would appear that the anterior thalamic lesion effects are primarily being driven by their ascending inputs from the mammillary bodies; in contrast, fornix lesions that disconnect the hippocampal projections to the anterior thalamic nuclei and mammillary bodies have far less pronounced effects on retrosplenial immediate-early gene expression (Vann et al., 2000).

In the present experiment, there was a significant decrease in cytochrome oxidase expression both in the superficial and deep layers of dysgranular retrosplenial cortex and the deep layers of granular retrosplenial cortex. In contrast, an earlier study assessing cytochrome oxidase activity after bilateral anterior thalamic lesions only found a decrease in layer 2 of retrosplenial granular b (Mendez-Lopez et al., 2003). The apparent differences between the findings from anterior thalamic and mammillothalamic tract lesions may reflect indirect versus direct loss of innervations, given that changes in cytochrome oxidase can reflect trans-synaptic disconnection (Wong-Riley, 1989). Alternatively, methodological differences, e.g., time post-surgery, the extent to which the lesions encompass the anteromedial and anteroventral thalamic nuclei, and the length and type of behavioural training used, may have contributed to the different pattern of changes. There is some evidence that retrosplenial hypoactivity is affected by the post-surgery interval in anterior thalamic-lesioned animals, with only superficial granular being affected initially and more widespread hypoactivity, including deeper granular layers and dysgranular cortex, found months after surgery (e.g., Jenkins et al., 2002). However, a separate study found widespread retrosplenial changes a month after surgery (Poirier & Aggleton, 2009) i.e., within the same time-frame used in the Mendez-Lopez et al. Study (2013). Time since surgery appears to have very little effect when considering the distal effects of mammillothalamic tract lesions as very similar patterns of *c-fos* changes are found both 3 weeks and 9 months post-surgery (Vann & Albasser, 2009; Vann, 2013). To determine whether there is a genuine difference between mammillothalamic tract and anterior thalamic nuclei

lesions in the time-frame of changes to the deeper retrosplenial layers, the lesion effects would need to be compared directly within the same study.

4.4.10 Hypoactivity of the retrosplenial cortex in diencephalic amnesia

The retrosplenial cortex hypoactivity following mammillothalamic tract and anterior thalamic lesions appears to be a robust finding across markers of activity. Furthermore, pathology within the medial diencephalon in patients has also been also associated with retrosplenial hypoactivity (Reed et al., 2003). In rats, the hypoactivity does not appear to be task-dependent as changes have been found across a number of behavioural tasks and retrosplenial hypoactivity (as measured by *c-fos*) has even been reported in home-cage animals with anterior thalamic lesions (Jenkins et al., 2002) perhaps reflecting an underlying hypometabolic state. To understand how retrosplenial cortex dysfunction may contribute to subsequent spatial memory impairments, a comparison of lesion effects becomes particularly relevant. In rats, mammillothalamic and retrosplenial lesions typically produce very similar profiles of impairment, with the clearest deficits found on spatial memory tasks (Vann & Aggleton, 2002). While both structures appear important for path integration (Winter et al., 2011), the spatial memory impairments cannot simply be attributed to an inability to navigate; retrosplenial cortex lesions and mammillothalamic tract lesions impair performance on a location discrimination task and an object-in-place task, which both tax aspects of spatial memory but lack a navigational component (Hindley et al., 2014). To date, there have been no direct comparisons of animals with retrosplenial and mammillothalamic tract lesions within the same study; however, when comparing across studies, it would appear that on certain tasks, mammillothalamic tract or mammillary body lesions can be more disruptive than retrosplenial cortex lesions (e.g., Vann, 2013). Thus, it is unlikely that retrosplenial dysfunction alone is sufficient to explain all mammillothalamic tract-lesion induced memory impairments but it may, nevertheless, exacerbate the lesion effects. The retrosplenial cortex appears to be particularly sensitive to damage within the Papez circuit and is one of the first brain regions to show hypoactivity in Mild Cognitive Impairment and early Alzheimer's disease (e.g.,

Valla et al., 2001). Understanding why this structure is so severely affected by distal pathology and whether this hypoactivity contributes to any cognitive impairments are important next steps for future research.

5 General discussion
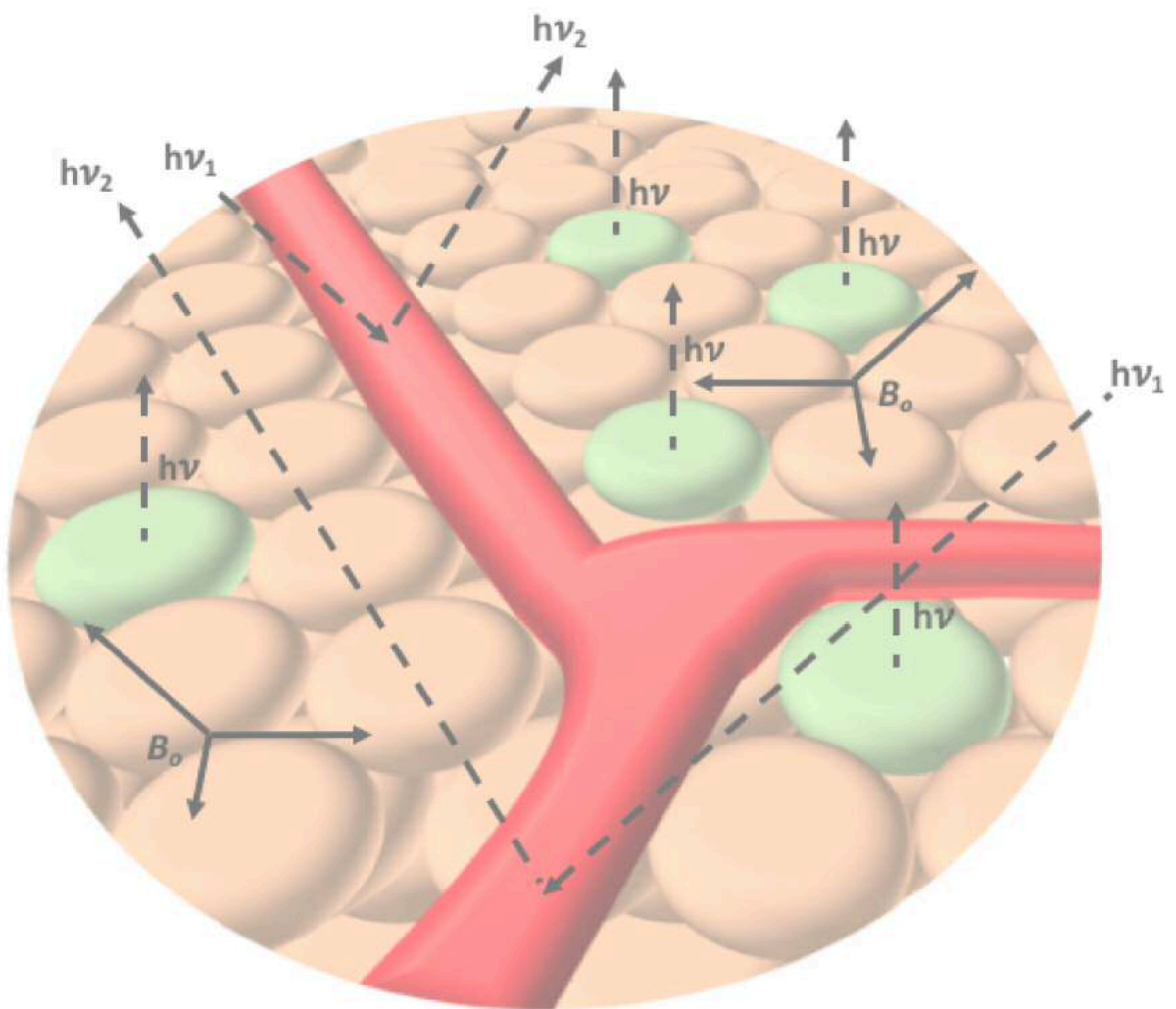
The goal of the project described in this thesis was to further the understanding of the role of the retrosplenial cortex in health and disease. Such broad a task required a multifaceted approach, especially given the complex nature of retrosplenial interactions within several functional networks. For that reason, it was deemed most appropriate to employ a multimodal *in-vivo* imaging paradigm suitable for probing the dynamics of visual and visuospatial processing and the accompanying plastic changes. Work presented here affirmed the involvement of the retrosplenial cortex in basic visual processing, demonstrated the formation of stable spatial memory representations and showed retrosplenial dysregulation at a microstructural level in a model of diencephalic amnesia. Furthermore, as all three imaging methods were put to test in novel experimental paradigms, this project also evaluated their utility in studying the interaction between cortical physiology and behaviour, paving the way for more complex future investigations.

5.1.1 Summary of the main findings and future directions

The contribution of the retrosplenial cortex to basic visual processing was investigated in **Chapter 2**. Craniotomised mice were subject to intrinsic signal imaging upon repeated presentations of drifting gratings. The locations of craniotomies allowed for surveying the retrosplenial cortex or the visual cortex and caudal barrel cortex areas. As such, it was possible to make the comparison between retrosplenial and visual cortex responses and to indirectly answer the question of the specificity of the signal (by analysing somatosensory responses). Moderately anaesthetised animals displayed anatomically defined and stimulus-locked intrinsic signals, which, in the retrosplenial cortex, reached a third of the amplitude observed in the visual cortex. In mildly anaesthetised animals, much of the intrinsic signal was occluded by a non-specific haemodynamic response, which proved too strong for the recovery of signal in fully awake mice. Nevertheless, retrosplenial signals under moderate anaesthesia appeared specific to that region as crossmodal stimulation elicited very weak responses of the sensory cortices and because retrosplenial tuning curves slightly differed from those observed in the visual cortex. Specifically, the retrosplenial cortex

exhibited preference for low spatial frequencies and a small bias towards cardinal versus non-cardinal orientations. While these results contrasted with a previous report utilising calcium-imaging methodology (Murakami et al., 2015), they did accord with the placement of the retrosplenial cortex in the dorsal visual stream, as seen in human neuroimaging studies (Bar, 2004; Vuilleumier et al., 2003; Watson et al., 2016). While informative, intrinsic signal imaging of the retrosplenial cortex proved challenging and prone to much noise, especially in weakly-anaesthetised mice. Consequently, it was deemed unsuitable for investigating visually-guided behaviour, which had been the goal of the intended follow-up study.

An increasingly popular approach to studying visually-evoked responses in the cortex is calcium imaging and preliminary data from the Sengpiel laboratory indicate the presence of responsive neurons in the caudal portion of the dysgranular retrosplenial cortex, similar to what has been observed in the currently discussed study. Since calcium imaging can be carried out in awake, moving mice, it appears more suited for the study of visually-guided behaviour. It still does, however, present certain challenges. Virally-delivered constructs produce high expression in infected cells but require several weeks to reach appropriate levels and eventually lead to signal oversaturation, effectively restricting the experimental window to only 2-3 weeks. On the other hand, mouse lines expressing calcium indicators show stable levels of fluorescence, which does, however, come at the cost of lower signal intensity. Another technique, multi-array electrode recordings, offers good signal levels with exceptional temporal resolution, even in moving animals, and can be implanted for many weeks. The downside of electrode recordings is that they do not allow for recovering the identity of individual cells and require very sophisticated analytic approaches.

Chapter 3 provides evidence for the formation and maintenance of spatial memory representations (memory engrams) in the dysgranular retrosplenial cortex. Active cells were visualised via craniotomies, similar to those described

in **Chapter 2**, in mice expressing the green fluorescent protein under the control of the *c-fos* promoter. Putative memory engrams were assessed by tracking the identity of fluorescent cells during the training phase of a spatial reference memory task and at two tests of memory retention. Crucially, animals were also imaged under control conditions: exposure to a dark cage (negative control) or a novel environment. The mice reached asymptotic performance after 19 days of training and showed gradually impoverished memory after the intervals of 6 24 days. *c-fos* levels were found to be sensitive to the experimental conditions as retrosplenial activity was lowest after exposure to the dark, intermediate following placement in the radial-arm maze and highest after exposure to novelty. Moreover, the pattern of active neurons showed gradual stabilisation during the acquisition of the task and the two retention sessions displayed a good degree of overlap with the final day of training but not with control sessions. This was reflected by the presence of four clusters identified by hierarchical cluster analysis: one encompassing habituation and initial training, another – subsequent training sessions and retention tests, next – the two negative controls, and finally – novelty on its own. Since the degree of forgetting and the overlap of the neuronal representations between the two retention sessions were related, it was concluded that the dysgranular retrosplenial cortex was indeed involved in the expression of long-term spatial memory.

While the presented results are merely correlative in nature, they provide some persuasive evidence for the retrosplenial cortex as one of the loci of spatial memory. First, the pattern of overlap between experimental conditions was remarkably similar across animals. Next, the fidelity of the putative engram was not merely time-dependent as control conditions close in time to the final training session elicited lower overlap scores than the final retention test (24 days from last training session). Finally, the apparent relationship between engram stability and memory retention on the final testing session demonstrate that even a very small snapshot of retrosplenial activity contains information predictive of animals' performance. One can only speculate that capturing a richer dataset would have allowed for more accurate predictions to be made. As the

experimental paradigm used in this study proved well suited for its intended purposes, it could be extended to allow for testing mechanistic hypotheses such as whether the presence of the retrosplenial engram is necessary and sufficient for the expression of memory. This could be achieved by means of optogenetic and chemogenetic tools, which allow for selective activation or inactivation of engrams (e.g.: Tanaka et al., 2014; Tayler et al., 2013). Moreover, future experiments could also be combined with post-mortem slice patch-clamp to establish whether engram cells exhibit differentiating electrophysiological properties such as higher excitability and more frequent/larger miniature excitatory postsynaptic potentials. It could also be hypothesised that engrams form distinct connections from those of their neighbouring cells, which could be tested by viral trans-synaptic tracing (Wickersham et al., 2007). A specific prediction would be that they receive stronger top-down inputs originating from other cortical areas such as the visual and frontal cortices.

Chapter 4 describes the use of diffusion tensor imaging (DTI) to track the progression of changes in fractional anisotropy (FA) and mean diffusivity (MD) in rats subject to mammillothalamic tract (MTT) lesions and in control cases. The success of lesions was assayed by a spatial working-memory task and confirmed in post-mortem tissue. Animals were scanned at four timepoints: before surgery, after surgery, and at the beginning and the end of behavioural testing (which lasted 16 days). Consistent with earlier work (e.g. Vann & Aggleton, 2003), lesioned rats displayed a greater number of spatial working memory errors. Multivoxel pattern analysis revealed that lesions led to differential MD values across many brain sites, including the MTT, anterior thalamus and dorsal hippocampus. On the other hand, differential FA values were predominantly associated with behavioural training, and affected a number of cortical sites, including the retrosplenial cortex. Region-based analyses revealed that lesions produced elevated MD values and attenuated training-induced increases in FA values. Consistent with this, higher retrosplenial FA values were found to be associated with fewer errors in lesion cases but not in shams, indicating that FA may be a sensitive metric reflecting plasticity. Taken

together, DTI proved a useful tool in tracking lesion-induced microstructural changes and displayed sensitivity to the behavioural task.

Yet, further experiments are required to elucidate the physiological basis of the observed DTI patterns as it remains largely unknown what they represent. As discussed in **Chapter 4**, it has been postulated that fluctuations in grey matter FA and MD metrics reflect altered synaptic connectivity and glial proliferation. It is therefore intended to stain tissue from the current cohort for a number of gutamatergic and GABAergic vesicular transport markers as well as for Homer1a, a component of the postsynaptic density, to reveal whether different classes of retrosplenial synapses were altered by lesions. The tissue will also be processed for glial fibrillary acidic protein, brain-derived neurotrophic factor and luxol blue (a histochemical stain of white mater) and analysed in an unbiased way mirroring multivoxel pattern analysis, followed by region-based analysis at higher magnification.

In conclusion, the observed DTI changes revealed the extent of microstructural alterations upon disconnection within the circuit of Papez, involving many subcortical and cortical sites, such as the retrosplenial cortex. In light of this, it would appear that despite their limited connectivity, the mammillary bodies might exert far-reaching influence over much of the brain. One intriguing possibility is that they are not merely a relay system for vestibulospatial information but also a site involved in off-line processing. This notion will be explored in future work by examining their contribution to memory formation within the theta oscillome. Of course, an alternative explanation for the widespread pattern of DTI changes is that lesion-based approaches inevitably trigger compensatory mechanisms. This would be consistent with the observed range of retrosplenial FA values in lesion cases, which were related to behavioural performance, therefore suggesting the use of strategies not relying on an intact Papez circuit. Learning more about what these strategies and compensatory mechanisms could be might one day benefit the sufferers of diencephalic amnesia. It can be imagined that patients could be trained to utilise

brain pathways unaffected by damage or perhaps that these pathways could be pharmacologically or electrically potentiated.

5.1.2 The retrosplenial cortex as a vital node for memory processes

As discussed previously, the retrosplenial cortex can be positioned within at least three interconnected networks: the dorsal visual stream, the default-mode network and the extended memory system. It is astonishing that a structure of such small a size in the human brain (0.3% cortical surface) appears to feature in so many different cognitive processes. Still, the roles ascribed to each of these networks do converge in the context of visuospatial and autobiographical memory, faculties showing decline following retrosplenial damage and affected in a number of syndromic neurological conditions displaying retrosplenial dysfunction. It remains plausible, however, that the scope of retrosplenial function in the rodent brain exceeds that of the primate brain. This is because primate brains show much more developed visual areas as well as sites without obvious homologues in the rodent brain, such as the posterior cingulate (Brodmann areas 23 and 31)(Vogt & Paxinos, 2014). It is thus conceivable that rodent retrosplenial cortex supports a broader spectrum of function than that of the human brain. Conversely, mouse and rat retrosplenial cortex is also limited in its scope since they lack what is understood as autobiographical memory in humans. Although certain attempts have been made to tease out aspects of 'episodic memory' in rodents (e.g. Eacott & Norman, 2004), these cannot be equated to anything close to the conscious recall of memory.

Nevertheless, a growing body of evidence collected in human subjects favours the notion of spatial memory as a vital 'mental scaffold' for more complex autobiographical memories, thus positioning the retrosplenial cortex at the core of mnemonic processes (Robin, Buchsbaum & Moscovitcht, 2018). Therefore, even if the direct role of the retrosplenial cortex is that of processing spatial information, it may still aid other networks in their specific functions. Perhaps unsurprisingly, retrosplenial dysfunction has been reported in a wide array of neurological conditions such as amnesias (Bowers & Watson, 1988; Buckley &

Mitchell, 2016; Gainotti et al., 1998; Nestor et al., 2003; Osawa et al., 2008; Vann & Albasser, 2009), schizophrenia (Douaud et al., 2007; Nestor et al., 2007), autism spectrum disorder (Cherkassky et al., 2006; Weng et al., 2009), posttraumatic stress disorder (Sartory et al., 2013) and others (Vann, Aggleton & Maguire, 2009). Figure 5.1.2 below graphically summarises some of the retrosplenial contributions to cognition (yellow circle) and associated neurological conditions (red circle).
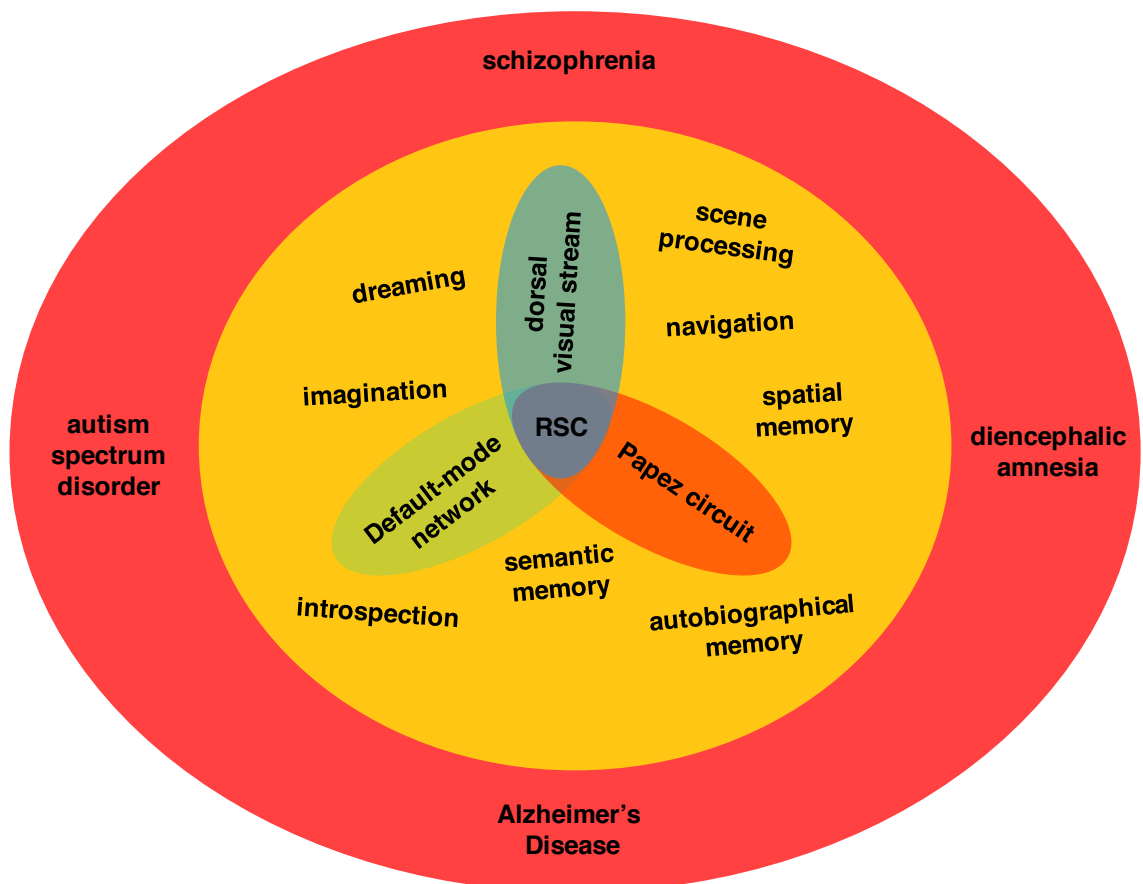
Figure 5.1.2. A diagrammatical summary of the interconnectedness of the retrosplenial cortex and its relation to cognitive function and neurological disorders.

5.1.3 Concluding remarks

Recent years have seen the retrosplenial cortex emerge from nearly total obscurity to the pedestal of memory research and current advances in animal and human experimental techniques are bound to facilitate many more fascinating insights into its role in cognition. The author of this thesis hopes to be a part of this effort.

References

Acosta-Cabronero, J., & Nestor, P. J. (2014). Diffusion tensor imaging in Alzheimer's disease: insights into the limbic-diencephalic network and methodological considerations. *Frontiers in Aging Neuroscience*, *6*(October), 1–21.

Aggleton, J. P., & Brown, M. W. (1999). Episodic memory, amnesia, and the hippocampal – anterior thalamic axis. *Behavioural and Brain Sciences*, *22*, 425–489.

Aggleton, J. P., Pralus, A., Nelson, A. J. D., & Hornberger, M. (2016). Thalamic pathology and memory loss in early Alzheimer's disease: moving the focus from the medial temporal lobe to Papez circuit. *Brain*, *139*(September), 1877–1890.

Aggleton, J. P., Vann, S. D., & Saunders, R. C. (2005). Projections from the hippocampal region to the mammillary bodies in macaque monkeys. *European Journal of Neuroscience*, *22*(July), 2519–2530.

Aguirre, G. K., & Esposito, M. D. (1999). Topographical disorientation: a synthesis and taxonomy. *Brain*, *122*, 1613–1628.

Akpinar, E., Koroglu, M., & Ptak, T. (2007). Diffusion tensor MR imaging in pediatric head trauma. *JCAT*, *31*(5), 657–661.

Alexander, A. S., & Nitz, D. A. (2015). Retrosplenial cortex maps the conjunction of internal and external spaces. *Nature Neuroscience*, (July), 1–12.

Alexander, A. S., & Nitz, D. A. (2017). Spatially periodic activation patterns of retrosplenial cortex encode route sub-spaces and distance traveled. *Current Biology*, *27*(11), 1551–1560.

Allen Institute for Brain Science, . (2017). Allen Brain Atlas. Retrieved from http://mouse.brain-map.org

Andermann, M. L., Kerlin, A. M., Roumis, D. K., Glickfeld, L. L., & Reid, C. (2013). Functional specialization of mouse higher visual cortical areas. *Neuron*, *72*(6), 1–32.

Andrews-Hanna, J. R., Smallwood, J., & Spreng, R. N. (2014). The default network and self-generated thought: component processes, dynamic control, and clinical relevance. *Annals of the New York Academy of Sciences*, *1316*, 29–52.

Auger, S. D., & Maguire, E. A. (2013). Assessing the mechanism of response in the retrosplenial cortex of good and poor navigators. *CORTEX*, *49*(10), 2904–2913.

Auger, S. D., Zeidman, P., & Maguire, E. A. (2015). A central role for the retrosplenial cortex in de novo environmental learning. *eLIFE*, 1–26.

Auger, S. D., Zeidman, P., & Maguire, E. A. (2017). Efficacy of navigation may be influenced by retrosplenial cortex-mediated learning of landmark stability. *Neuropsychologia*, *104*(July), 102–112.

Ay, H., Furie, K. L., Yamada, K., & Koroshetz, W. J. (1998). Diffusion-weighted MRI characterizes the ischemic lesion in transient global amnesia. *Neurology*, *51*, 901–904.

Bai, F., Zhang, Z., Yu, H., Shi, Y., & Yuan, Y. (2008). Default-mode network activity distinguishes amnestic type mild cognitive impairment from healthy aging : A combined structural and resting-state functional MRI study. *Neuroscience Letters*, *438*, 111–115.

Bar, M. (2004). Visual objects in context. *Nature Reviews Neuroscience*, *5*, 617–629.

Bar, M. (2009). The proactive brain : memory for predictions. *Philosophical Transactions of the Royal Society B*, *364*, 1235–1243.

Barry, D. N., Coogan, A. N., & Commins, S. (2016). The time course of systems consolidation of spatial memory from recent to remote retention : A comparison of the Immediate Early Genes Zif268 , c-Fos and Arc. *Neurobiology of Learning and Memory*, *128*, 46–55.

Barth, A. L., Gerkin, R. C., & Dean, K. L. (2004). Alteration of Neuronal Firing Properties after In Vivo Experience in a FosGFP Transgenic Mouse. *The Journal of Neuroscience*, *24*(29), 6466–6475.

Bathellier, B., Ville, D. Van De, Blu, T., Unser, M., & Carleton, A. (2007). Wavelet-based multi-resolution statistics for optical imaging signals : Application to automated detection of odour activated glomeruli in the mouse olfactory bulb. *NeuroImage*, *34*(3), 1020–1035.

Becerra, L., Pendse, G., Chang, P., Bishop, J., & Borsook, D. (2011). Robust reproducible resting state networks in the awake rodent brain. *PlosOne*, *6*(10), 1–10.

Beckmann, C. F., Deluca, M., Devlin, J. T., Smith, S. M., Hospital, J. R., & Ox, O. (2005). Investigations into resting-state connectivity using independent component analysis. *Philosophical Transactions of the Royal Society B*, (May), 1001–1013.

Benedict, R. H. B., Hulst, H. E., Bergsland, N., Schoonheim, M. M., Dwyer, M. G., Weinstock-, B., … Zivadinov, R. (2013). Clinical significance of atrophy and white matter mean diffusivity within the thalamus of multiple sclerosis patients. *Multiple Sclerosis Journal*, *19*, 1478–1484.

Bernstein, H., Krause, S., Krell, D., Dobrowolny, H., Wolter, M., Stauch, R., … Jirikowski, G. F. (2007). Strongly reduced number of parvalbumin-immunoreactive projection neurons in the mammillary bodies in schizophrenia. *Annals of the New York Academy of Sciences*, *1096*, 120–127.

Berretta, S., Parthasarathy, H. B., & Graybiel, A. M. (1997). Local Release of GABAergic Inhibition in the Motor Cortex Induces Immediate-Early Gene Expression in Indirect Pathway Neurons of the Striatum. *The Journal of Neuroscience*, *17*(12), 4752–4763.

Betts, E. S., Krasnova, I. N., Mccoy, M. T., Ladenheim, B., & Cadet, J. L. (2002). Analysis of methamphetamine-induced changes in the expression of integrin family members in the cortex of wild-type and c-fos knockout mice. *Neurotoxicity Research*, *4*, 617–623.

Bicanski, A., & Burgess, N. (2016). Environmental anchoring of head direction in a computational model of retrosplenial cortex. *The Journal of Neuroscience*, *36*(46), 11601–11618.

Bihan, D. Le, Poupon, C., Clark, C. A., Pappata, S., Molko, N., & Chabriat, H. (2001). Diffusion tensor imaging : concepts and applications. *Journal of*

Magnetic Resonance Imaging, *546*, 534–546.

Bliss, T. V. P., & Lomo, T. (1973). Long-lasting potentiation of synaptic transmission in the dentate area of the anaesthetised rabbit following stimulation of the perforant path. *Journal of Physiology*, *232*, 331–356.

Blumenfeld-katzir, T., Pasternak, O., Dagan, M., & Assaf, Y. (2011). Diffusion MRI of structural brain plasticity induced by a learning and memory task, *6*(6).

Bonner, M. F., & Epstein, R. A. (2017). Coding of navigational affordances in the human visual system. *PNAS*, *114*, 1–6.

Bowers, D., & Watson, R. (1988). Retrosplenial amnesia. *Brain*, *110*(January), 1631–1646. https://doi.org/10.1093/brain/110.6.1631

Briski, K., & Gillen, E. (2001). Differential distribution of Fos expression within the male rat preoptic area and hypothalamus in response to physical vs . psychological stress. *Brain Research Bulletin*, *55*(3), 401–408.

Buckner, R. L., Snyder, A. Z., Shannon, B. J., Larossa, G., Sachs, R., Fotenos, A. F., … Mintun, M. A. (2005). Molecular, structural, and functional characterization of Alzheimer's Disease : Evidence for a relationship between default activity, amyloid, and memory. *The Journal of Neuroscience*, *25*(34), 7709–7717.

Budde, M. D., Janes, L., Gold, E., Turtzo, L. C., & Frank, J. A. (2011). The contribution of gliosis to diffusion tensor anisotropy and tractography following traumatic brain injury : validation in the rat using Fourier analysis of stained tissue sections. *BRAIN*, *134*(September), 2248–2260.

Bullitt, E. (1990). Expression of C-fos-Like Protein as a Marker for Neuronal Activity Following Noxious Stimulation in the Rat. *The Journal of Comparative Neurology*, *296*, 517–530.

Bumstead, J. R., Bauer, A. Q., Wright, P. W., & Culver, J. P. (2016). Cerebral functional connectivity and Mayer waves in mice : Phenomena and separability. *Journal of Cerebral Blood Flow and Metabolism*, *0*, 1–14.

Burles, F., Slone, E., & Iaria, G. (2016). Dorso-medial and ventro-lateral functional specialization of the human retrosplenial complex in spatial updating and orienting. *Brain Structure and Function*, *222*, 1481–1493.

Bustos, S. G., Maldonaldo, H., & Molina, V. A. (2009). Disruptive Effect of Midazolam on Fear Memory Reconsolidation : Decisive Influence of Reactivation Time Span and Memory Age Disruptive Effect of Midazolam on Fear Memory Reconsolidation : Decisive Influence of Reactivation Time Span and Memory Age. *Neuropsychopharmacology*, *34*(April), 446–457.

Caulo, M., Hecke, J. Van, Toma, L., Ferretti, A., Tartaro, A., Colosimo, C., … Uncini, A. (2005). Functional MRI study of diencephalic amnesia in Wernick –Korsakoff syndrome. *Brain*, *128*, 1584–1594.

Chard, P. S., Bleakman, D., Christakos, S., Fullmer, C., & Miller, R. (1993). Calcium buffering properties of calbindin D28k and parvalbumin in rat sensory neurones. *Journal of Physiology*, *472*, 341–357.

Chen-Bee, C. H., Kwon, M. C., Masino, S. A., & Frostig, R. D. (1996). Areal extent quantification of functional representations using intrinsic signal optical imaging. *Journal of Neuroscience Methods*, *68*, 27–37.

Chen, L. L., Carol, L.-H. L., Barnes, C. A., & Mcnaughton, B. L. (1994). Head-direction cells in the rat posterior cortex II. Contributions of visual and

ideothetic information to the directional firing. *Experimental Brain Research*, *101*, 24–34.

Chen, L. L., Edward, L. L., Barnes, C. A., & Mcnaughton, B. L. (1994). Head-direction cells in the rat posterior cortex I . anatomical distribution and behavioral modulation. *Experimental Brain Research*, *101*, 8–23.

Cherkassky, V. L., Kana, R. K., Keller, T. A., & Just, M. A. (2006). Functional connectivity in a baseline resting-state network in autism. *NeuroReport*, *17*(16), 7–10.

Chiu, R., Jennifer, J. B., Smeal, T., Hunter, T., & Karint, M. (1988). The c-Fos Protein Interacts with cJun / AP-1 to Stimulate Transcription of AP-1 Responsive Genes. *Cell*, *54*, 541–552.

Cho, J., & Sharp, P. E. (2001a). Head direction, place, and movement correlates for cells in the rat retrosplenial cortex. *Behavioral Neuroscience*, *115*(February 2001).

Cho, J., & Sharp, P. E. (2001b). Head Direction , Place , and Movement Correlates for Cells in the Rat Retrosplenial Cortex. *Behavioural Neuroscience*, *115*(1), 3–25.

Choi, W., & Henderson, J. M. (2015). Neural correlates of active vision: An fMRI comparison of natural reading and scene viewing. *Neuropsychologia*, *75*, 109–118.

Coleman, M. P., & Freeman, M. R. (2010). Wallerian degeneration, Wld, and Nmnat. *Annual Review In Neuroscience*, *33*, 245–269.

Countryman, R. A., Kaban, N. L., & Colombo, P. J. (2007). Hippocampal c-fos is necessary for long-term memory of a socially transmitted food preference. *Neurobiology of Learning and Memory*, *84*(2005), 175–183.

Cowansage, K. K., Shuman, T., Dillingham, B. C., Chang, A., & Golshani, P. (2014). Article Direct Reactivation of a Coherent Neocortical Memory of Context. *Neuron*, *84*(2), 432–441.

Cruce, J. A. (1975). An autoradiographic study of the projections of the mammillothalamic tract in the rat. *Brain Research*, *86*, 211–219.

Czajkowski, R., Jayaprakash, B., Wiltgen, B., Rogerson, T., Guzman-Karlsson, M. C., Barth, A. L., … Silva, A. J. (2014). Encoding and storage of spatial information in the retrosplenial cortex. *PNAS*, *111*(27), 8661–8666.

Dalrymple-Alford, J. C., Harland, B., Loukavenko, E. A., Perry, B., Mercer, S., Collings, D. A., … Wolff, M. (2015). Anterior thalamic nuclei lesions and recovery of function : Relevance to cognitive thalamus. *Neuroscience and Biobehavioral Reviews*, *54*, 145–160.

Del Vechio Koike, X. B., Koike, V., Farias, X. K. S., Billwiller, X. F., Almeida-filho, X. D., Libourel, X. P., … I, C. B. L. (2017). Electrophysiological evidence that the retrosplenial cortex displays a strong and specific activation phased with hippocampal theta during paradoxical (REM) sleep. *The Journal of Neuroscience*, *37*(33), 8003–8013.

Denby, C. E., Vann, S. D., Tsivilis, D., Aggleton, J. P., Roberts, N., & Mayes, A. R. (2009). The frequency and extent of mammillary body atrophy associated with surgical removal of a colloid cyst. *American Journal of Neuroradiology*, *30*, 736–746.

Dillingham, C. M., Frizzati, A., Nelson, A. J. D., & Vann, S. D. (2015). How do mammillary body inputs contribute to anterior thalamic function?

Neuroscience and Biobehavioral Reviews, *54*, 108–119.

Douaud, G., Smith, S., Jenkinson, M., Behrens, T., Johansen-berg, H., Vickers, J., … James, A. (2007). Anatomically related grey and white matter abnormalities in adolescent-onset schizophrenia. *Brain*, *130*(September), 2375–2386.

Downes, J. J., Mayes, A. R., Macdonald, C., & Hunkin, N. M. (2002). Temporal order memory in patients with Korsakoff's syndrome and medial temporal amnesia. *Neuropsychologia*, *40*, 853–861.

Dragunow, M., Abraham, W. C., Goulding, M., & Mason, S. E. (1989). Long-term potentiation and the induction of c-los mRNA and proteins in the dentate gyrus of unanesthetized rats. *Neuroscience Letters*, *101*, 274–280.

Dror, V., Eliash, S., Rehavi, M., Assaf, Y., Biton, I. E., & Fattal-valevski, A. (2009). Neurodegeneration in thiamine deficient rats — A longitudinal MRI study. *Brain Research*, *1308*, 176–184.

Dudai, Y. (2012). The Restless Engram: Consolidations Never End. *Annual Review In Neuroscience*, *35*(March), 227–247.

Dumont, J. R., & Aggleton, J. P. (2013). Dissociation of recognition and recency memory judgments after anterior thalamic nuclei lesions in rats. *Behavioral Neuroscience*, *127*(3), 415–431.

Dumont, J. R., Amin, E., Poirier, G. L., Albasser, M. M., & Aggleton, J. P. (2012). Anterior thalamic nuclei lesions in rats disrupt markers of neural plasticity in distal limbic brain regions. *Neuroscience*, *224*, 81–101.

Dunn, A. K., Devor, A., Dale, A. M., & Boas, D. A. (2005). Spatial extent of oxygen metabolism and hemodynamic changes during functional activation of the rat somatosensory cortex. *NeuroImage*, *27*, 279–290.

Ellard, C. G., & Chapman, D. G. (1991). The effects of posterior cortical lesions on responses to visual threats in the Mongolian gerbil (Meriones unguiculatus). *Behavioural Brain Research*, *44*, 163–167.

Epstein, R. A. (2008). Parahippocampal and retrosplenial contributions to human spatial navigation. *Trends in Cognitive Sciences*, *12*(10), 388–396.

Evans, T., Bicanski, A., Bush, D., & Burgess, N. (2015). How environment and self-motion combine in neural representations of space. *The Journal of Physiology*, *0*(April), 1–12.

Fama, R., Pitel, A.-L., & Sullivan, E. V. (2012). Anterograde episodic memory in Korsakoff Syndrome. *Neuropsychologiy Review*, *22*(2), 93–104.

Fazio, F., Perani, D., Gilardi, M. C., Colombo, F., Cappa, S. F., Vallar, G., … Lenzi, L. (1992). Metabolic Impairment in human amnesia: A PET study of memory networks. *Journal of Cerebral Blood Flow and Metabolism*, *12*, 353–358.

Feldman, H. M., Yeatman, J. D., Lee, E. S., Barde, L. H. F., & Gaman-Bean, S. (2014). Diffusion tensor imaging: a review for pediatric researchers and clinicians. *Journal of Developmental and Behavioural Pediatrics*, *31*(4), 346–356.

Fiebig, F., & Lansner, A. (2014). Memory consolidation from seconds to weeks: a three-stage neural network model with autonomous reinstatement dynamics. *Frontiers in Computational Neuroscience*, *8*(July), 1–17.

Fleischmann, A., Hvalby, O., Jensen, V., Strekalova, T., Zacher, C., Layer, L. E., … Gass, P. (2003). Impaired Long-Term Memory and NR2A-Type NMDA

Receptor-Dependent Synaptic Plasticity in Mice Lacking c-Fos in the CNS, *23*(27), 9116–9122.

Forsberg, A., Engler, H., Almkvist, O., Blomquist, G., Wall, A., Ringheim, A., & Bengt, L. (2008). PET imaging of amyloid deposition in patients with mild cognitive impairment. *Neurobiology of Ageing*, *29*, 1456–1465.

Frizzati, A., Milczarek, M. M., Sengpiel, F., Thomas, K. L., Dillingham, C. M., & Vann, S. D. (2016). Comparable reduction in zif268 levels and cytochrome oxidase activity in the retrosplenial cortex following mammillothalamic tract lesions. *Neuroscience*, *330*, 39–49.

Frostig, R. D., Lieke, E. E., Ts'o, D. Y., & Grinvald, A. (1990). Cortical functional architecture and local coupling between neuronal activity and the microcirculation revealed by in vivo high-resolution optical imaging of intrinsic signals. *PNAS*, *87*(August), 6082–6086.

Gainotti, G., Almonti, S., Maria, A., Betta, D., Caterina, M., Gainotti, G., … Silveri, M. C. (1998). Retrograde amnesia in a patient with retrosplenial tumour. *Neurocase*, *4*(September), 519–526.

García, G., Gerrikagoitia, I., & Martínez-Millán, L. (2001). Plastic response of the retrospleniocollicular connection after removal of retinal inputs in neonatal rats. An anterograde tracing study. *Experimental Brain Research*, *138*, 343–351.

Ghosh, A., Ginty, D. D., Bading, H., & Greenberg, M. E. (1993). Calcium Regulation of Gene Expression in Neuronal Cells. *Developmental Nurobiology*, *25*(3), 294–303.

Glickfeld, L. L., Reid, R. C., & Andermann, M. L. (2014). A mouse model of higher visual cortical function. *Current Opinion in Neurobiology*, *24*, 28–33.

Gökçek-Saraç, Ç., Wesierska, M., & Jakubowska-Dogru, E. (2015). Comparison of spatial learning in the partially baited radial-arm maze task between commonly used rat strains : Wistar , Wistar / Sprague-Dawley. *Learning and Behaviour*, *43*, 83–94.

Gore, F., Schwartz, E. C., Brangers, B. C., Gordon, J. A., Salzman, C. D., Axel, R., … Likhtik, E. (2015). Neural Representations of Unconditioned Stimuli in Basolateral Amygdala Mediate Innate and Learned Article Neural Representations of Unconditioned Stimuli in Basolateral Amygdala Mediate Innate and Learned Responses. *Cell*, *162*(1), 134–145.

Graham, D. J. L., Tseng, S., Hsieh, J., Chen, D. J., & Alexandrakis, G. (2015). Dependence of two-photon eGFP bleaching on femtosecond pulse spectral amplitude and phase. *Journal of Fluorescence*, *25*(6), 1775–1785.

Granziera, C., Hadjikhani, N., Arzy, S., & Seeck, M. (2011). In-vivo magnetic resonance imaging of the structural core of the Papez circuit in humans. *NeuroReport*, *22*, 227–231.

Greene, K. K., Donders, J., & Thoits, T. (2006). Topographical heading disorientation: a case study. *The Journal of Applied Neuropsychology*, *13*, 269–274.

Gregory, A., Gilberto, R., Schwamm, L. H., Huang-helbinger, F. R., Reese, G., Weisskoff, M., … Rosen, R. (1996). Hyperacute stroke : evaluation with combined multisection diffusion-weighted and hemodynamically weighted echo-planar MR imaging. *Radiology*, *199*, 391–401.

Greicius, M. (2008). Resting-state functional connectivity in neuropsychiatric

disorders. *Current Opinion In Neurology*, *21*, 424–430.

Greicius, M. D., Supekar, K., & Menon, V. (2009). Resting-state functional connectivity reflects structural connectivity in the Default Mode Network. *Cerebral Cortex*, *19*(September), 72–78.

Grieve, S. M., Williams, L. M., Paul, R. H., Clark, C. R., & Gordon, E. (2007). Cognitive aging, executive function, and fractional anisotropy: a diffusion tensor MR imaging study. *American Journal of Neuroradiology*, *28*, 226–235.

Grimm, R., Schicknick, H., Riede, I., Gundelfinger, E. D., Herdegen, T., Zuschratter, W., & Tischmeyer, W. (1997). Suppression of c-fos Induction in rat brain impairs retention of a brightness discrimination reaction. *Learning and Memory*, *3*, 402–414.

Grimm, R., & Tischmeyer, W. (1997). Complex patterns of immediate early gene induction in rat brain following brightness discrimination training and pseudotraining. *Behavioural Brain Research*, *84*, 109–116.

Grinvald, A., & Bonhoeffer, T. (n.d.). Optical imaging of electrical activity based on intrinsic signals and on voltage sensitive dyes. Retrieved February 9, 2017, from

Grinvald, A., Frostig, R. D., Siegel, R. M., & Bartfeld, E. (1991). High-resolution optical imaging of functional brain architecture in the awake monkey. *PNAS*, *88*(December), 11559–11563.

Grinvald, A., & Hildesheim, R. (2004). VSDI : A new era in functional imaging of cortical dynamics. *Nature Reviews Neuroscience*, *5*(November), 874–885.

Grinvald, A., Lieke, E., Frostig, R. D., Gilbert, C. D., & Wiesel, T. N. (1986). Functional architecture of cortex revealed by optical imaging of intrinsic signals. *Nature*, *324*, 361–364.

Groen, I. I. A., Silson, E. H., & Baker, C. I. (2017). Contributions of low- and high-level properties to neural processing of visual scenes in the human brain. *Philosophical Transactions of the Royal Society B*, *372*, 1–11.

Gucht, E. Van Der, Hof, P. R., Brussel, L. Van, Burnat, K., & Arckens, L. (2007). Neurofilament protein and neuronal activity markers define regional architectonic parcellation in the mouse visual cortex. *Cerebral Cortex*, *1986*(December), 2805–2819.

Gudden, H. (1896). Klinische und anatomische Beiträge zur Kenntniss der multiplen Alkoholneuritis nebst Bemerkungen über die Regenerationsvorgänge im peripheren Nervensystem. *Archiv Fuer Psychiatrie Und Nervenkrankheiten*, *28*, 634–741.

Guenthner, C. J., Miyamichi, K., Yang, H. H., Heller, C. H., & Luo, L. (2013). Permanent Genetic Access to Transiently Active Neurons via TRAP: Targeted Recombination in Active Populations. *Neuron*, *78*(5), 773–784.

Guzowski, J. F., Setlow, B., Wagner, E. K., & Mcgaugh, J. L. (2001). Experience-Dependent Gene Expression in the Rat Hippocampus after Spatial Learning : A Comparison of the Immediate-Early Genes Arc , c- fos , and zif268. *The Journal of Neuroscience*, *21*(14), 5089–5098.

Han, J.-H., Kushner, S., Yiu, P. A., Cole, C. J., Martynia, A., Brown, R. A., … Josselyn, S. A. (2013). Neuronal competition and selection during memory formation. *Science*, *316*(2007), 457–460.

Hansen, M. B., Jespersen, S. N., Leigland, L. A., Kroenke, C. D., & Sun, P.

(2013). Using diffusion anisotropy to characterize neuronal morphology in gray matter: the orientation distribution of axons and dendrites in the NeuroMorpho.org database. *Frontiers in Integrative Neuroscience*, *7*(May), 1–13.

Harding, A., Halliday, G., Caine, D., & Kril, J. (2000). Degeneration of anterior thalamic nuclei differentiates alcoholics with amnesia. *Brain*, *123*, 141–154.

Harland, B. C., Collings, D. A., Mcnaughton, N., & Abraham, W. C. (2014). Anterior thalamic lesions reduce spine density in both hippocampal CA1 and retrosplenial cortex, but enrichment rescues CA1 spines only. *Hippocampus*, *24*(May), 1232–1247.

Harland, B., Wood, E. R., & Dudchenko, P. A. (2015). The head direction cell system and behavior: the effects of lesions to the lateral mammillary bodies on spatial memory in a novel landmark task and in the water maze. *Behavioral Neuroscience*.

He, J., Yamada, K., Nakajima, A., Kamei, H., & Nabeshima, T. (2002). Learning and memory in two different reward tasks in a radial arm maze in rats. *Behavioural Brain Research*, *134*, 139–148.

Henderson, J. M., Larson, C. L., & Zhu, D. C. (2008). Full Scenes produce more activation than Close-up Scenes and Scene-Diagnostic Objects in parahippocampal and retrosplenial cortex: An fMRI study. *Brain and Cognition*, *66*, 40–49.

Herrera, D. G., & Robertson, Harold, A. (1996). Activation of c-fos in the brain. *Progress in Neurobiology*, *50*, 83–107.

Hess, S., & Galllj, M. (1995). Changes in c-fos mRNA Expression in Rat Brain during Odor Discrimination Learning: Differential Involvement of Hippocampal Subfields CA1 and CA3. *The Journal of Neuroscience*, *15*(July).

Hess, U. S., Lynch, G., & Gall, C. M. (1995). Regional Patterns of c-fos mRNA Expression in Rat Hippocampus Following Exploration of a Novel Environment versus Performance of a Well-Learned Discrimination. *The Journal of Neuroscience*, *15*(December), 7796–7809.

Hindley, E. L., Nelson, A. J. D., Aggleton, J. P., & Vann, S. D. (2014). Dysgranular retrosplenial cortex lesions in rats disrupt cross-modal object recognition. *Learning and Memory*, *21*, 171–179.

Hindley, E. L., Nelson, A. J. D., Aggleton, J. P., & Vann, S. D. (2014). The rat retrosplenial cortex is required when visual cues are used flexibly to determine location. *Behavioural Brain Research*, *263*, 98–107.

Hishida, R., Kudoh, M., & Shibuki, K. (2014). Multimodal cortical sensory pathways revealed by sequential transcranial electrical stimulation in mice. *Neuroscience Research*, *87*, 49–55.

Hoeft, F., Barnea-goraly, N., Haas, B. W., Golarai, G., Ng, D., Mills, D., … Reiss, A. L. (2007). More is not always better: increased fractional anisotropy of superior longitudinal fasciculus associated with poor visuospatial abilities in Williams Syndrome. *The Journal of Neuroscience*, *27*(44), 11960–11965.

Hoelscher, C. (1999). Stress impairs performance in spatial water maze learning tasks. *Behavioural Brain Research*, *100*, 225–235.

Hofstetter, S., & Assaf, Y. (2017). The rapid development of structural plasticity through short water maze training : A DTI study. *NeuroImage*, *155*(April), 202–208.

Hoz, L. De, Gierej, D., Lioudyno, V., Jaworski, J., Blazejczyk, M., Cruces-solís, H., … Kaczmarek, L. (2017). Blocking c-Fos Expression Reveals the Role of Auditory Cortex Plasticity in Sound Frequency Discrimination Learning. *Cerebral Cortex*, 1–11.

Hsu, H., Chen, T.-Y., Chan, M.-H., & Chen, H.-H. (2007). Acute effects of nicotine on restraint stress-induced anxiety-like behavior , c-Fos expression , and corticosterone release in mice. *European Journal of Pharmacology*, *566*, 124–131.

Hunkin, N. M., & Parkin, A. J. (1993). Recency judgements in Wernicke-Korsakoff and post-encephalitic amnesia: influences of proactive interference and retention interval. *Cortex*, *29*(3), 485–499.

Huth, A. G., Nishimoto, S., & Gallant, X. J. L. (2016). Functional Subdomains within scene-selective cortex : parahippocampal place area, retrosplenial complex, and occipital place area. *The Journal of Neuroscience*, *36*(40), 10257–10273.

Insausti, R., Amaral, D. G., & Cowan, W. M. (1987). The entorhinal cortex of the monkey: II. Cortical afferents. *The Journal of Comparative Neurology*, *264*, 356–395.

Jacob, P., Casali, G., Spieser, L., Page, H., Overington, D., & Jeffery, K. (2017). An independent, landmark-dominated head-direction signal in dysgranular retrosplenial cortex. *Nature Neuroscience Brief Communications*, *20*, 173–175.

Jarrard, L. E. (1983). Selective Hippocampal Lesions and Behavior : Effects of Kainic Acid Lesions on Performance of Place and Cue Tasks. *Behavioural Neuroscience*, *97*(6), 873–889.

Jenkins, T. A., Dias, R., Amin, E., Brown, M. W., & Aggleton, J. P. (2002). Fos imaging reveals that lesions of the anterior thalamic nuclei produce widespread limbic hypoactivity in rats. *The Journal of Neuroscience*, *22*(12), 5230–5238.

Ji, D., & Wilson, M. A. (2007). Coordinated memory replay in the visual cortex and hippocampus during sleep. *Nature Neuroscience*, *10*(1), 100–107.

Jones, B. F., Groenewegen, H. J., & Witter, M. P. (2005). Intrinsic connections of the cingulate cortex in the rat suggest the existence of multiple functionally segregated networks. *Neuroscience*, *133*, 193–207.

Kaczmarek, L., & Chaudhuri, A. (1997). Sensory regulation of immediate – early gene expression in mammalian visual cortex : implications for functional mapping and neural plasticity. *Brain Reserach Reviews*, *23*, 237–256.

Kaneyama, K., Nagao, T., & Segami, N. (2007). Opening of shortcut circuits between visual and retrosplenial granular cortices of rats. *NeuroReport*, *18*(13), 1315–1318.

Kapur, N., Thompson, S., Cook, P., Lang, D., & Brice, J. (1996). Anterograde but not retrograde memory loss following combined mammillary body and medial thalamic lesions. *Neuropsychologia*, *34*(1), 1–8.

Katche, C., & Medina, J. H. (2017). Requirement of an Early Activation of BDNF /c-Fos Cascade in the Retrosplenial Cortex for the Persistence of a Long-

Lasting Aversive Memory. *Cerebral Cortex*, (December 2015), 1060–1067.

Kim, D. S., Duong, T. Q., & Kim, S. G. (2000). High-resolution mapping of iso-orientation columns by fMRI. *Nature Neuroscience*, *3*, 164–169.

Kim, Y., Venkataraju, K. U., Pradhan, K., Mende, C., Taranda, J., & Turaga, S. C. (2015). Mapping Social Behavior-Induced Brain Activation at Cellular Resolution in the Mouse. *CellReports*, *10*(2), 292–305.

Kinnavane, L., Amin, E., Horne, M., & Aggleton, J. P. (2014). Mapping parahippocampal systems for recognition and recency memory in the absence of the rat hippocampus. *European Journal of Neuroscience*, *40*(August), 3720–3734.

Kish, S. J., Bergeron, C., Rajput, T., Dozic, S., Mastrogiacomo, F., Chang, L., … Nobrega, N. (1992). Brain cytochrome oxidase in Alzheimer's Disease. *Journal of Neurochemistry*, *59*(1979), 776–779.

Kitamura, T., Ogawa, S. K., Roy, D. S., Okuyama, T., Morrisey, M. D., Smith, L. M., … Tonegawa, S. (2017). Engrams and circuits crucial for systems consolidation of a memory. *Science*, *78*(April), 73–78.

Klingberg, T., Vaidya, C. J., Gabrieli, J. D. E., Moseley, M. E., & Hedehus, M. (1999). Myelination and organization of the frontal white matter in children: a diffusion tensor MRI study. *NeuroReport*, *10*(13), 2817–2821.

Kobayashi, Y., & Amaral, D. G. (2000). Macaque monkey retrosplenial cortex: I. Three-dimensional and cytoarchitectonic organisation. *The Journal of Comparative Neurology*, *426*(December 1998), 339–365.

Kobayashi, Y., & Amaral, D. G. (2003). Macaque monkey retrosplenial cortex: II. cortical afferents. *The Journal of Comparative Neurology*, *79*(March), 48–79.

Kobayashi, Y., & Amaral, D. G. (2007). Macaque monkey retrosplenial cortex: III. Cortical efferents. *The Journal of Comparative Neurology*, *502*(September 2006).

Kocsis, B., & Vertes, R. P. (1994). Characterization of neurons of the supramammillary nucleus and mammillary body that discharge rhythmically with the hippocampal theta rhythm in the rat. *The Journal of Neuroscience*, *14*(November), 7040–7052.

Komlosh, M. E., & Basser, P. J. (2007). Detection of microscopic anisotropy in gray matter and in a novel tissue phantom using double Pulsed Gradient Spin Echo MR. *Journal of Magnetic Resonance*, *189*, 38–45.

Kopelman, M. D. (1995). The Korsakoff Syndrome. *British Journal of Psychiatry*, *166*, 154–173.

Koya, E., Golden, S. A., Harvey, B. K., Guez-barber, D. H., Berkow, A., Simmons, D. E., … Hope, B. T. (2009). Targeted disruption of cocaine-activated nucleus accumbens neurons prevents context-specific sensitization. *Nature Publishing Group*, *12*(8), 1069–1073.

Kravitz, D. J., Saleem, K. S., Baker, C. I., & Mishkin, M. (2011). A new neural framework for visuospatial processing. *Nature Neuroscience Reviews*, *12*(4), 217–230.

Lacar, B., Linker, S. B., Jaeger, B. N., Krishnaswami, S. R., Barron, J. J., Paquola, C. M., … Gage, F. H. (2016). Nuclear RNA-seq of single neurons reveals molecular signatures of activation. *Nature Communications*, *7*, 1–11.

Lamprecht, R., & Dudai, Y. (1996). Transient expression of c-fos in rat amygdala during training is required for encoding conditioned taste aversion memory. *Learning and Memory*, *3*, 31–41.

Leemans, A., Jersuissen, B., Sijbers, J., & Jones, D. K. (2009). ExploreDTI: a graphical toolbox for processing, analyzing, and visualizing diffusion MR data. In *Proceedings of the International Society of Magnetic Resonance In Medicine* (p. 3537).

Leinweber, M., Ward, D. R., Sobczak, J. M., Attinger, A., Keller, G. B., Leinweber, M., … Keller, G. B. (2017). A sensorimotor circuit in mouse cortex for visual flow predictions. *Neuron*, *95*, 1420–1432.

Liska, A., Galbusera, A., Schwarz, A. J., & Gozzi, A. (2015). Functional connectivity hubs of themouse brain. *NeuroImage*, *115*, 281–291.

Liste, I., Rozas, G., & Guerra, M. J. (1995). Cortical stimulation induces Fos expression in striatal neurons via NMDA glutamate and dopamine receptors. *Brain Research*, *700*, 1–12.

Liu, X., Ramirez, S., Pang, P. T., Puryear, C. B., Govindarajan, A., Deisseroth, K., & Tonegawa, S. (2012). Optogenetic stimulation of a hippocampal engram activates fear memory recall. *Nature*, *484*(7394), 381–385.

Liu, X., Suh, J., Pignatelli, M., & Ryan, T. J. (2015). Creating a False Memory in the Hippocampus.

Logothetis, N. K., Guggenberger, H., Peled, S., & Pauls, J. (1999). Functional imaging of the monkey brain. *Nature Neuroscience*, *2*, 555–562.

Lozano, Y. R., Page, H., Jacob, P., Lomi, E., Street, J., & Jeffery, K. (2017). Retrosplenial and postsubicular head direction cells compared during visual landmark discrimination. *Brain and Neuroscience Advances*.

Lu, H., Zou, Q., Gu, H., Raichle, M. E., Stein, E. A., & Yang, Y. (2012). Rat brains also have a default mode network. *PNAS*, *109*(10).

Lux, V., Atucha, E., Kitsukawa, T., & Sauvage, M. M. (2016). Imaging a memory trace over half a life- time in the medial temporal lobe reveals a time-limited role of CA3 neurons in retrieval. *eLife*, 1–19.

Lythgoe, M. F., Busza, A. L., Calamante, F., Sotak, C. H., King, M. D., Bingham, A. C., … Gadian, D. G. (1997). Effects of difision anisotropy on lesion delineation in a rat model of cerebral ischemia. *Cerebral Ischemia in the Rat*, *38*, 662–668.

Ma, Y., Shaik, M. A., Kim, S. H., Kozberg, M. G., Thibodeaux, D. N., Zhao, H. T., … Hillman, E. M. C. (2016). Wide-field optical mapping of neural activity and brain haemodynamics : considerations and novel approaches. *Philosophical Transactions of the Royal Society B*, *371*, 1–17.

Ma, Z., Cao, P., Sun, P., Zhao, L., Li, L., & Tong, S. (2016). Inverted optical intrinsic response accompanied by decreased cerebral blood flow are related to both neuronal inhibition and excitation. *Nature Scientific Reports*, *6*(September 2015), 1–14.

Maddock, R. L. (1999). The retrosplenial cortex and emotion : new insights from functional neuroimaging of the human brain. *Trends in Neurosciences*, *22*, 310–316.

Mainardi, M., Landi, S., Berardi, N., Maffei, L., & Pizzorusso, T. (2009). Reduced Responsiveness to Long-Term Monocular Deprivation of Parvalbumin Neurons Assessed by c-Fos Staining in Rat Visual Cortex.

PloS One, *4*(2), 1–8.

Makino, H., & Komiyama, T. (2015). Learning enhances the relative impact of top-down processing in the visual cortex. *Nature Neuroscience*, (July), 1–10.

Malonek, D., & Grinvald, A. (1996). Interactions between electrical activity and cortical microcirculation revealed by imaging spectroscopy: implications for functional brain mapping. *Science*, *272*(April), 551–553.

Mao, D., Kandler, S., Mcnaughton, B. L., & Bonin, V. (2017). Sparse orthogonal population representation of spatial context in the retrosplenial cortex. *Nature Communications*, *8*, 1–9.

Marr, D. (1971). Simple Memory: A Theory for Archicortex. *Philosophical Transactions of the Royal Society*, *262*, 23–81.

Martin, C., Berwick, J., Martin, C., Martindale, J., Berwick, J., & Mayhew, J. (2006). Investigating neural-hemodynamic coupling and the hemodynamic response function in the awake rat. *NeuroImage*, *32*(September 2017), 33–48.

Masino, S. A., Kwon, M. C., Dory, Y., & Frostig, R. D. (1993). Characterization of functional organization within rat barrel cortex using intrinsic signal optical imaging through a thinned skull. *PNAS*, *90*(November), 9998–10002.

Matsuo, N. (2015). Irreplaceability of Neuronal Ensembles after Memory Report Irreplaceability of Neuronal Ensembles after Memory Allocation. *CellReports*, *11*(3), 351–357.

Matsuo, N., & Mayford, M. (2008). Spine-type Specific Recruitment of Newly Synthesized AMPA Receptors with Learning. *Science*, *319*(5866), 1104–1107.

Maviel, T., Durkin, T. P., Menzaghi, F., & Botempi, B. (2004). Sites of neocortical reorganization critical for remote spatial memory. *Science*, *305*(July), 96–99.

Mazoyer, B., Zago, L., Mellet, E., Bricogne, S., Etard, O., Houde, O., … Petit, L. (2001). Cortical networks for working memory and executive functions sustain the conscious resting state in man. *Brain Research Bulletin*, *54*(3), 287–298.

Mccoy, A. N., Crowley, J. C., Haghighian, G., Dean, H. L., Platt, M. L., & Carolina, N. (2003). Saccade reward signals in posterior cingulate cortex. *Neuron*, *40*, 1031–1040.

Mcgeachie, A. B., Cingolani, L. A., & Goda, Y. (2011). A stabilising influence: Integrins in regulation of synaptic plasticity. *Neuroscience Research*, *70*(1), 24–29.

McLoughlin, N. P., & Blasdel, G. G. (1998). Wavelength-dependent differences between optically determined functional maps from macaque striate cortex. *NeuroImage*, *7*, 326–336.

Mendez-Lopez, M., Arias, J. L., Botempi, B., & Wolff, M. (2003). Reduced cytochrome oxidase activity in the retrosplenial cortex after lesions to the anterior thalamic nuclei. *Behavioural Brain Research*, *250*, 264–273.

Mitchell, A. S., & Dalrymple-Alford, J. C. (2006). Lateral and anterior thalamic lesions impair independent memory systems. *Learning and Memory*, *13*, 388–396.

Moennikes, H.; Schmidt, B. G.; Tache, Y. (1993). Psychological Stress-Induced Accelerated Colonic Transit in Factor. *Gastroenterology*, *104*, 716–723.

Morgan, J. I., Cohen, D. R., Hempstead, J. L., & Curran, T. O. M. (1987). Mapping Patterns of c-fos Expression in the Central Nervous System after Seizure. *Science*, *237*(4811), 192–197.

Morris, E., Pandya, D. N., & Petrides, M. (1999). Fiber system linking the mid-dorsolateral frontal cortex with the retrosplenial/presubicular region in the rhesus monkey. *The Journal of Comparative Neurology*, *407*(November 1998), 183–192.

Morris, R. G. M., Anderson, E., Lynch, G. S., & Baudry, M. (1986). Selective impairment of learning and blockade of long-term potentiation by an N-mythyl-D-aspartate receptor antagonist, AP5. *Nature*, *319*, 774–776.

Morrison, D. J., Rashid, A. J., Yiu, A. P., Yan, C., Frankland, P. W., & Josselyn, S. A. (2016). Parvalbumin interneurons constrain the size of the lateral amygdala engram. *Neurobiology of Learning and Memory*, *135*, 91–99.

Morrow, B. A., Elsworth, J. D., Inglis, F. M., & Roth, R. H. (1999). An antisense oligonucleotide reverses the footshock-induced expression of fos in the rat medial prefrontal cortex and the subsequent expression of conditioned fear-induced immobility. *The Journal of Neuroscience*, *19*(13), 5666–5673.

Mufson, E. J., & Pandya, D. N. (1984). Some observations on the course and composition of the cingulum bundle in the rhesus monkey. *The Journal of Comparative Neurology*, *225*, 31–43.

Murakami, T., Yoshida, T., Matsui, T., & Ohki, K. (2015). Wide-field Ca2+ imaging reveals visually evoked activity in the retrosplenial area. *Frontiers in Molecular Neuroscience*, *8*(June), 1–12.

Murphy, K., Birn, R. M., Handwerker, D. A., Jones, T. B., & Bandettini, P. A. (2009). The impact of global signal regression on resting state correlations : Are anti-correlated networks introduced? *NeuroImage*, *44*(3), 893–905.

Mutisya, E. M., Bowling, A. C., & Beal, M. F. (1994). Cortical cytochrome oxidase activity is reduced in Alzheimer's Disease. *Journal of Neurochemistry*, *63*, 2179–2184.

Nadel, L., & Hardt, O. (2010). Update on memory systems and processes. *Neuropsychopharmacology*, *36*(1), 251–273.

Nahum, L., Suisse, I., Lazeyras, F., Haller, S., & Schnider, A. (2015). Neural correlate of anterograde amnesia in Wernicke-Korsakoff Syndrome. *Brain Topography*, *28*(August), 760–770.

Narayan, S. M., Santori, E. M., & Toga, A. W. (1994). Mapping functional activity in rodent cortex using optical intrinsic signals. *Cerebral Cortex*, *4*, 195–204.

Nasiriavanaki, M., Xia, J., Wan, H., Quentin, A., & Culver, J. P. (2014). High-resolution photoacoustic tomography of resting-state functional connectivity in the mouse brain. *PNAS*, *111*, 21–26.

Nasr, S., & Tootell, R. B. H. (2012). A cardinal orientation bias in scene-selective visual cortex. *The Journal of Neuroscience*, *32*(43), 14921–14926.

Nelson, A. J. D., Powell, A. L., Holmes, J. D., Vann, S. D., & Aggleton, J. P. (2015). What does spatial alternation tell us about retrosplenial cortex function? *Frontiers in Behavioural Neuroscience*, *9*(May), 1–15.

Nelson, A. J. D., & Vann, S. D. (2014). Mammilliothalamic tract lesions disrupt tests of visuo-spatial memory. *Behavioural Neuroscience*, *128*(4), 494–503.

Nelson, A. J. D., & Vann, S. D. (2017). The importance of mammillary body efferents for recency memory: towards a better understanding of diencephalic amnesia. *Brain Structure and Function*, *222*(5), 2143–2156.

Nestor, P. G., Kubicki, M., Kuroki, N., Gurrera, R. J., Niznikiewicz, M., Shenton, M. E., & Mccarley, R. W. (2007). Episodic memory and neuroimaging of hippocampus and fornix in chronic schizophrenia. *Psychiatry Research: Neuroimaging*, *155*, 21–28.

Nestor, P. J., Fryer, T. D., Ikeda, M., & Hodges, J. R. (2003). Retrosplenial cortex (BA 29 / 30) hypometabolism in mild cognitive impairment (prodromal Alzheimer ' s disease). *European Journal of Neuroscience*, *18*(July).

Nguyen, D. Van, Grebenkov, D., Le, D., & Li, J. (2015). Numerical study of a cylinder model of the diffusion MRI signal for neuronal dendrite trees. *Journal of Magnetic Resonance*, *252*, 103–113.

Nishio, Y., Hashimoto, M., Ishii, K., & Mori, E. (2011). Neuroanatomy of a neurobehavioral disturbance in the left anterior thalamic infarction. *Journal of Neurology, Neurosurgery and Psychiatry*, *82*, 1195–1200.

Norman, J. (2002). Two visual systems and two theories of perception: An attempt to reconcile the constructivist and ecological approaches. *Behavioural and Brain Sciences*, *25*, 73–144.

Oh, S. W., Harris, J. A., Ng, L., Winslow, B., Cain, N., Wang, Q., … Zeng, H. (2016). A mesoscale connectome of the mouse brain. *Nature*, *508*(7495), 207–214.

Ohkawa, N., Saitoh, Y., Suzuki, A., Tsujimura, S., Murayama, E., & Kosugi, S. (2015). Artificial Association of Pre-stored Information to Generate a Qualitatively New Memory Article Artificial Association of Pre-stored Information to Generate a Qualitatively New Memory. *CellReports*, *11*(2), 261–269.

Olsen, G. M., Ohara, S., Iijima, T., & Witter, M. P. (2017). Parahippocampal and retrosplenial connections of rat posterior parietal cortex. *Hippocampus*, *27*, 335–358.

Olton, D. S., & Papas, B. C. (1979). Spatial memory and hippocampal function. *Neuropsychologia*, *17*, 669–682.

Osawa, A., Maeshima, S., & Kunishio, K. (2008). Topographic disorientation and amnesia due to cerebral hemorrhage in the left retrosplenial region. *European Journal of Neurology*, *59*, 79–82.

Palm, G. (2013). Neural associative memories and sparse coding. *Neural Networks*, *37*, 165–171.

Papez, J. W. (1937). A proposed mechanism of emotion. *Archives of Neurology and Psychiatry*, *38*, 725–743.

Paredes, R. M., Etzler, J. C., Watts, L. T., Zheng, W., & Lechleiter, J. D. (2008). Chemical calcium indicators. *Methods*, *46*(3), 143–151.

Park, K. W., Seo, J. H., & Yoon, G.-U. (2007). Selective anterograde amnesia with thalamus and hippocampal lesions in neuro-Behcet's disease. *Clinical Neurology and Neurosurgery*, *109*, 470–473.

Parmeggiani, P. L., Azzaroni, A., & Lenzi, P. (1971). On the functional

significance of the circuit of Papez. *Brain Research*, *30*, 357–374.

Parthasarathy, H. B., & Graybiel, A. M. (1997). Cortically Driven Immediate-Early Gene Expression Reflects Modular Influence of Sensorimotor Cortex on Identified Striatal Neurons in the Squirrel Monkey, *17*(7), 2477–2491.

Patai, E. Z., Javadi, A.-H., Ozubko, J. D., Callaghan, O., Ji, S., Robin, J., … Spiers, H. J. (2017). Long- - term consolidation switches goal proximity coding from hippocampus to retrosplenial cortex.

Pawela, C. P., Biswal, B. B., Cho, Y. R., Kao, D. S., Li, R., Jones, S. R., … Hyde, J. S. (2008). Resting-state functional connectivity of the rat brain. *Magnetic Resonance in Medicine*, *59*, 1021–1029.

Paylor, R., Johnson, R. S., Papaioannou, V., Spiegelman, B. M., & Wehner, J. M. (1994). Behavioural assessment of c-fos mutant mice. *Brain Research*, *651*, 275–282.

Penfield, W. Rasmussen, T. (1950). No Title. In *The cerebral cortex of man: a clinical study of localisation and function*. New York.

Pengas, G., Williams, G. B., Acosta-Cabronero, J., Ash, T. W. J., Hong, Y. T., Izquiredo-Garcia, D., … Nestor, P. J. (2012). The relationship of topographical memory performance to regional neurodegeneration in Alzheimer's disease. *Frontiers in Aging Neuroscience*, *4*(July), 1–10.

Pisauro, A. M., Benucci, A., & Carandini, M. (2016). Local and global contributions to hemodynamic activity in mouse cortex. *Journal of Neurophysiology*, *115*, 2931–2936.

Poirier, G. L., & Aggleton, J. P. (2009). Post-surgical interval and lesion location within the limbic thalamus determine extent of retrosplenial cortex immediate-early gene hypoactivity. *Neuroscience*, *160*, 452–469.

Poirier, G. L., Amin, E., & Aggleton, J. P. (2008). Qualitatively different hippocampal subfield engagement emerges with mastery of a spatial memory task by rats. *The Journal of Neuroscience*, *28*(5), 1034–1045.

Poirier, G. L., Shires, K. L., Sugden, D., Amin, E., Thomas, K. L., Carter, D. A., & Aggleton, J. P. (2008). Anterior thalamic lesions produce chronic and profuse transcriptional deregulation in retrosplenial cortex: a model of retrosplenial hypoactivity and covert pathology. *Thalamus and Related Systems*, *4*, 59–77.

Poirier, W., Huang, G. L., R, T. J., Difranza, K., & King, J. A. (2017). Awake whole-brain functional connectivity alterations in the adolescent spontaneously hypertensive rat feature visual streams and striatal networks. *Brain Structure and Function*, *222*, 1673–1683.

Pollmann, S., Jana, E., Sommer, S., Chelazzi, L., & Zinke, W. (2016). Neural structures involved in visual search guidance by reward-enhanced contextual cueing of the target location. *NeuroImage*, *124*, 887–897.

Pothuizen, H. H. J., Davies, M., Albasser, M. M., Aggleton, J. P., & Vann, S. D. (2009). Granular and dysgranular retrosplenial cortices provide qualitatively different contributions to spatial working memory : evidence from immediate-early gene imaging in rats. *European Journal of Neuroscience*, *30*(June), 877–888.

Pothuzien, H. H. J., Zhang, W., Jongen-Relo, A. L., Feldon, J., & Yee, B. K. (2004). Dissociation of function between the dorsal and the ventral hippocampus in spatial learning abilities of the rat : a within-subject ,

within-task comparison of reference and working spatial memory. *European Journal of Neuroscience*, *19*(August 2017), 705–712.

Powell, A. L., Kinnavane, L., Davies, M., Amin, E., Vann, S. D., Olarte-Sanchez, C. M., … Nelson, A. J. D. (2017). The retrosplenial cortex and object recency memory in the rat. *EJN*, *45*, 1451–1464.

Rakhade, S. N., Shah, A. K., Agarwal, R., Yao, B., Asano, E., & Loeb, J. A. (2007). Activity-dependent Gene Expression Correlates with Interictal Spiking in Human Neocortical Epilepsy. *Epilepsia*, *48*, 86–95.

Ramirez, S., Liu, X., MacDonald, C. J., Moffa, A., Zhou, J., Redondo, R. L., & Tonegawa, S. (2015). Activating positive memory engrams suppresses depression-like behaviour. *Nature*, *522*(7556), 335–339.

Redondo, R. L., Kim, J., Arons, A. L., Ramirez, S., Liu, X., & Tonegawa, S. (2014). Bidirectional switch of the valence associated with a hippocampal contextual memory engram. *Nature*, *513*(7518), 426–430.

Reed, L. J., Lasserson, D., Marsden, P., Stanhope, N., Stevens, T., Bello, F., … Kopelman, M. D. (2003). FDG-PET findings in the Wernicke-Korsakoff syndrome. *Cortex*, *39*, 1027–1045.

Reijmers, L. G., Perkins, B. L., Matsuo, N., & Mayford, M. (2007). Localization of a Stable Neural Correlate of Associative Memory, *317*(1230), Science.

Rogers, J. H., & Reisiboi, A. R. (1992). Calretinin and calbindin-D28k in rat brain: patterns of partial co-localization. *Neuroscience*, *51*(4).

Roth, M. M., Helmchen, F., & Kampa, M. (2012). Distinct functional properties of primary and posteromedial visual area of mouse neocortex. *The Journal of Neuroscience*, *32*(28), 9716–9726.

Roy, D. S., Arons, A., Mitchell, T. I., Pignatelli, M., Tonegawa, S., Fig, E. D., … Fig, E. D. (2016). Memory retrieval by activating engram cells in mouse models of early Alzheimer's disease. *Nature*, *531*, 508–512.

Ryan, T. J., Roy, D. S., Pignatelli, M., Arons, a., & Tonegawa, S. (2015). Engram cells retain memory under retrograde amnesia. *Science*, *348*(6238), 1007–1013.

Sagi, Y., Tavor, I., Hofstetter, S., Tzur-moryosef, S., Blumenfeld-katzir, T., & Assaf, Y. (2012). Learning in the fast lane: new insights into neuroplasticity. *Neuron*, *73*(6), 1195–1203.

Saito, K., Kimura, K., Minematsu, K., Shiraishi, A., & Nakajima, M. (2003). Transient global amnesia associated with an acute infarction in the retrosplenium of the corpus callosum. *Journal of the Neurological Sciences*, *210*, 95–97.

Salinas, K. J., Velez, D. X. F., Zeitoun, J. H., Kim, H., & Gandhi, S. P. (2017). Contralateral bias of high spatial frequency tuning and cardinal direction selectivity in mouse visual cortex. *The Journal of Neuroscience*, 1484–1517.

Santoro, A., & Frankland, P. W. (2014). Chasing the Trace. *Neuron*, *84*(2), 243–246.

Savage, L. M., Chang, Q., & Gold, P. E. (2003). Diencephalic damage decreases hippocampal acetylcholine release during spontaneous alternation testing. *Learning and Memory*, *10*, 242–246.

Schiessl, I., Wang, W., & Mcloughlin, N. (2008). Independent components of the haemodynamic response in intrinsic optical imaging. *NeuroImage*, *39*,

634–646.

Schindelin, J., Arganda-carreras, I., Frise, E., Kaynig, V., Longair, M., Pietzsch, T., ... Cardona, A. (2012). Fiji : an open-source platform for biological-image analysis. *Nature*, *9*(7), 676–682.

Schreiber, S. S., Maren, S., Tocco, G., & Shors, T. J. (1991). A negative correlation between the induction of long-term potentiation and activation of immediate early genes. *Molecular Brain Research*, *11*, 89–91.

Schummers, J., Yu, H., & Sur, M. (2014). Tuned responses of astrocytes and their influence on hemodynamic signals in the visual cortex. *Science*, *1638*(2008), 1638–1643.

Schuz, A., & Palm, G. (1989). Density of neurons and synapses in the cerebral cortex of the mouse. *The Journal of Comparative Neurology*, *286*, 442–455.

Scoville, W. B., & Milner, B. (1957). Loss of recent memory after bilateral hippocampal lesions. *Journal of Neurosurgery and Psychiatry, 20*, 11-21.

Seki, M., & Zyo, K. (1984). Anterior thalamic afferents from the mamillary body and the limbic cortex in the rat. *The Journal of Comparative Neurology*, *229*, 242–256.

Semon, R. W. (1921). The Mneme. In *The Mneme*. London: Allen and Uniwin Ltd.

Sforazzini, F., Schwarz, A. J., Galbusera, A., Bifone, A., & Gozzi, A. (2014). Distributed BOLD and CBV-weighted resting-state networks in the mouse brain. *NeuroImage*, *87*, 403–415.

Shah, A., Jhawar, S. S., & Goel, A. (2012). Analysis of the anatomy of the Papez circuit and adjoining limbic system by fiber dissection techniques. *Journal of Clinical Neuroscience*, *19*(2), 289–298.

Shah, D., Blockx, I., Guns, P., Paul, P., Deyn, D., Dam, D. Van, ... Linden, A. Van Der. (2015). Acute modulation of the cholinergic system in the mouse brain detected by pharmacological resting-state functional MRI. *NeuroImage*, *109*, 151–159.

Shakhawat, X. A., Gheidi, X. A., Hou, Q., Dhillon, S. K., Marrone, D. F., Harley, X. C. W., & Yuan, Q. (2014). Visualizing the engram : Learning stabilizes odor representations in the olfactory network. *The Journal of Neuroscience*, *34*(46), 15394–15401.

Shear, P. K., Sullivan, E. V, Lane, B., & Pfefferbaurn, A. (1996). Mammillary body and cerebellar shrinkage in chronic alcoholics with and without amnesia. *Alcoholism: Clinical and Experimental Research*, *20*, 1489–1495.

Sheline, Y. I., Morris, J. C., Snyder, A. Z., Price, J. L., Yan, Z., Angelo, G. D., ... Mintun, M. A. (2010). APOE4 allele disrupts resting state fMRI connectivity in the absence of amyloid plaques or decreased CSF Ab42. *The Journal of Neuroscience*, *30*(50), 17035–17040.

Sherstnev, V. V, Gruden, M. A., Storozheva, Z. I., Golubeva, O. N., & Proshin, A. T. (2013). Different populations of neurons in relevant brain structures are selectively engaged in the functioning of long term spatial memory. *Neurochemical Journal*, *7*(4), 278–283.

Shibata, H. (1993a). Direct projections from the anterior thalamic nuclei to the retrohippocampal region in the rat. *Journal of Comparative Neurology*, *337*, 431–445.

Shibata, H. (1993b). Efferent projections from the anterior thalamic nuclei to the cingulate cortex in the rat. *Journal of Comparative Neurology*, *330*, 533–542.

Shibata, H. (1994). Terminal distribution of projections from the retrosplenial area to the retro- hippocampal region in the rat, as studied by anterograde transport of biotinylated dextran amine. *Neuroscience Research*, *20*, 331–336.

Shibata, H., Honda, Y., & Sasaki, H. (2009). Organization of intrinsic connections of the retrosplenial cortex in the rat. *Anatomical Science International*, 280–292.

Shimamura, P., Jernigan, L., Squire, R., & Findings, C. T. (1988). Korsakoff's Syndrome : Radiological (CT) findings and neuropsychological correlates. *The Journal of Neuroscience*, *8*(November), 4400–4410.

Shin, N., Hong, J., & Choi, J. Y. (2017). Retrosplenial cortical thinning as a possible major contributor for cognitive impairment in HIV patients. *European Radiology*.

Shine, J. P., Valde, P., Hegarty, M., & Wolbers, T. (2016). The human retrosplenial cortex and thalamus code head direction in a global reference frame. *The Journal of Neuroscience*, *36*(24), 6371–6381.

Shires, K. L., & Aggleton, J. P. (2008). Mapping immediate-early gene activity in the rat after place learning in a water-maze : the importance of matched control conditions. *European Journal of Neuroscience*, *28*, 982–996.

Shtoyerman, E., Arieli, A., Slovin, H., Vanzetta, I., & Grinvald, A. (2000). Long-term optical imaging and spectroscopy reveal mechanisms underlying the intrinsic signal and stability of cortical maps in V1 of behaving monkeys. *The Journal of Neuroscience*, *20*(21), 8111–8121.

Smith, D. M., Barredo, J., & Mizumori, S. J. Y. (2011). Complimentary Roles of the Hippocampus and Retrosplenial Cortex in Behavioral Context Discrimination. *Hippocampus*, *0*, 1–13. https://doi.org/10.1002/hipo.20958

Smith, S. M., Miller, K. L., Moeller, S., Xu, J., Auerbach, E. J., & Woolrich, M. W. (2012). Temporally-independent functional modes of spontaneous brain activity. *PNAS*, *109*, 3131–3136.

Sonia, R., & Pich, E. M. (1996). The Reinforcing Properties of Nicotine are Associated - a Specific Patterning of c-fos Expression in the Rat with Brain. *European Journal of Neuroscience*, *8*(February).

Sorzano, C. Ó. S., Thévenaz, P., & Unser, M. (2005). Elastic registration of biological images using vector-spline regularization. *IEEE Transactions on Biomedical Engineering*, *52*(4), 652–663.

Spreng, R. N., Mar, R. A., & Kim, A. S. N. (2008). The common neural basis of autobiographical memory, prospection navigation, theory of mind, and the Default Mode : A quantitative meta-analysis. *Journal of Cognitive Neuroscience*, *21*, 489–510.

Squire, L. (1981). Two forms of human amnesia: an analysis of forgetting. *The Journal of Neuroscience*, *1*, 635–640.

Squire, L. R., Amaral, D. G., & Press, G. A. (1990). Magnetic resonance imaging of the hippocampal formation and mammillary nuclei distinguish medial temporal lobe and diencephalic amnesia. *The Journal of Neuroscience*, *10*(September), 3106–3117.

Squire, L. R., Amaral, D. G., Zola-Morgan, S., Kritchevsky, M., & Press, G. (1989). Description of brain injury in the amnesic patient N.A. based on magnetic resonance imaging. *Experimental Neurology*, *105*, 23–35.

Stafford, J. M., Jarrett, B. R., Miranda-Dominguez, O., Mills, B. D., Cain, N., & Mihalas, S. (2014). Large-scale topology and the default mode network in the mouse connectome. *PNAS*, *111*(52), 18745–18750.

Staiger, J. F., Masanneck, C., Bisler, S., Schleicher, A., Zuschratter, W., & Zilles, K. (2002). Excitatory and inhibitory neurons express c-fos in barrel-related columns after exploration of a novel environment. *Neuroscience*, *109*(4), 687–699.

Starck, T., Nikkinen, J., Rahko, J., Remes, J., Hurtig, T., Haapsamo, H., & Lynch, C. J. (2013). Resting state fMRI reveals a default mode dissociation between retrosplenial and medial prefrontal subnetworks in ASD despite motion scrubbing. *Frontiers in Human Neuroscience*, *7*(November), 1–10.

Stark, J. A., Davies, K. E., Williams, S. R., & Luckman, S. M. (2006). Functional magnetic resonance imaging and c-Fos mapping in rats following an anorectic dose of m -chlorophenylpiperazine. *NuroImage*, *31*, 1228–1237.

Strekalova, T., Zoerner, B., Zacher, C., Sadovska, G., Herdegen, T., & Gass, P. (2003). Memory retrieval after contextual fear conditioning induces c-Fos and JunB expression in CA1 hippocampus. *Genes, Brain and Behaviour*, *2*, 3–10.

Svarnik, O. E., Bulava, A. I., Alexandrov, Y. I., & Robinson, S. (2013). Expression of c-Fos in the rat retrosplenial cortex during instrumental re-learning of appetitive bar-pressing depends on the number of stages of previous training. *Frontiers in Behavioural Neuroscience*, *7*(July), 1–7.

Swank, M. W. (2000). Conditioned c-Fos in mouse NTS during expression of a learned taste aversion depends on contextual cues. *Brain Research*, *862*, 138–144.

Takahashi, N., Kawamura, M., Shiota, J., Kasahata, N., & Hirayama, K. (1997). Pure topographic disorientation due to right retrosplenial lesion. *Neurology*, *49*, 464–469.

Takayama, K., Suzuki, T., & Miura, M. (1994). The comparison of effects of various anaesthetics on expression of Fos protein in the rat brain. *Neuroscience Letters*, *176*, 59–62.

Takeuchi, Y., Allen, G. V, & Hopkins, D. A. (1985). Transnuclear transport and axon collateral projections of the mamillary nuclei in the rat. *Brain Research Bulletin*, *14*, 453–468.

Tanaka, K. Z., Pevzner, A., Hamidi, A. B., Nakazawa, Y., & Graham, J. (2014). Cortical Representations Are Reinstated by the Hippocampus during Memory Retrieval. *Neuron*, *84*(2), 347–354.

Tanaka, Y., Miyazawa, Y., Akaoka, F., & Yamada, T. (1997). Amnesia following damage to the mammillary bodies. *Neurology*, *48*(September 1994), 160–165.

Tanji, K., Suzuki, K., Fujii, T., Higano, S., & Yamadori, A. (2003). A case of frontal network amnesia. *Journal of Neural Neurosurgery and Psychiatry*, *74*, 106–109.

Taube, J. S. (1995). Head direction cells recorded in the anterior thalamic nuclei of freely moving rats. *The Journal of Neuroscience*, *15*, 70–86.

Taube, J. S. (2007). The head direction signal: Origins and sensory-motor integration. *Annual Review In Neuroscience*, *30*, 181–207.

Taube, S., Muller, U., & Ranck, B. (1990). Head-direction cells recorded from the postsubiculum in freely moving rats. I. Description and quantitative analysis. *The Journal of Neuroscience*, *10*(February), 420–435.

Tavor, I., Hofstetter, S., & Assaf, Y. (2013). Micro-structural assessment of short term plasticity dynamics. *NeuroImage*, *81*, 1–7.

Tayler, K. K., Tanaka, K. Z., Reijmers, L. G., & Wiltgen, B. J. (2013). Reactivation of neural ensembles during the retrieval of recent and remote memory. *Current Biology*, *23*(2), 99–106.

Teipel, S. J., Wegrzyn, M., Meindl, T., Frisoni, G., Bokde, A. L. W., Fellgiebel, A., … Ewers, M. (2012). Anatomical MRI and DTI in the diagnosis of Alzheimer's Disease: A European multicentre study. *Journal of Alzheimer's Disease*, *31*, s33–s47.

Thevenaz, P., Ruttimann, U. E., & Unser, M. (1998). A Pyramid Approach to Subpixel Registration Based on Intensity. *IEEE Transactions on Image Processing*, *7*(1), 27–41.

Thomas, A. G., Koumellis, P., & Dineen, R. A. (2011). The fornix in health and disease: An imaging review. *RadioGraphics*, *31*, 1107–1121.

Todd, T. P., Mehlman, M. L., Keene, C. S., DeAngeli, N. E., & Bucci, D. J. (2016). Retrosplenial cortex is required for the retrieval of remote memory for auditory cues. *Learning and Memory*, *23*, 278–288.

Tohmi, M., Kitaura, H., Komagata, S., Kudoh, M., & Shibuki, K. (2006). Enduring critical period plasticity visualized by transcranial flavoprotein imaging in mouse primary visual cortex. *The Journal of Neuroscience*, *26*(45), 11775–11785.

Tonegawa, S., Pignatelli, M., Roy, D. S., & Ryan, J. (2015). Memory engram storage and retrieval. *Current Opinion in Neurobiology*, *35*, 101–109.

Tseng, Q., Wang, I., Duchemin-Pelletier, E., Azioune, A., Carpi, N., Gao, J., … Balland, M. (2011). A new micropatterning method of soft substrates reveals that different tumorigenic signals can promote or reduce cell contraction levels. *Lab Chip*, *11*, 2231–2240.

Valla, J., Berndt, J. D., & Gonzalez-Lima, F. (2001). Energy hypometabolism in posterior cingulate cortex of alzheimer ' s patients: superficial laminar cytochrome oxidase associated with disease duration. *The Journal of Neuroscience*, *21*(13), 4923–4930.

van Groen, T., & Wyss, J. M. (1990a). Connections of the retrosplenial granular a cortex in the rat. *Journal of Comparative Neurology*, *300*, 593–606.

van Groen, T., & Wyss, J. M. (1990b). The postsubicular cortex in the rat: characterization of the fourth region of the subicular cortex and its connections. *Brain Research*, *529*, 165–177.

van Groen, T., & Wyss, J. M. (1992). Connections of the retrosplenial dysgranular cortex in the rat. *Journal of Comparative Neurology*, *315*, 200–216.

van Groen, T., & Wyss, J. M. (2003). Connections of the retrosplenial granular b cortex in the rat. *The Journal of Comparative Neurology*, *263*(March), 249–263.

Vanhoutte, P., Barnier, J., Guibert, B., Page, C., Besson, M., Hipskind, R. A., …

Fessard, I. A. (1999). Glutamate Induces Phosphorylation of Elk-1 and CREB , Along with c -fos Activation , via an Extracellular Signal-Regulated Kinase-Dependent Pathway in Brain Slices, *19*(1), 136–146.

Vann, S. D. (2005). Transient spatial deficit associated with bilateral lesions of the lateral mammillary nuclei. *European Journal of Neuroscience*, *21*, 820–824.

Vann, S. D. (2013). Dismantling the Papez circuit for memory in rats. *eLIFE*, 1–21.

Vann, S. D., & Aggleton, J. P. (2002). Extensive Cytotoxic Lesions of the Rat Retrosplenial Cortex Reveal Consistent Deficits on Tasks That Tax Allocentric Spatial Memory. *Behavioural Neuroscience*, *116*(1), 85–94.

Vann, S. D., & Aggleton, J. P. (2003). Evidence of a Spatial Encoding Deficit in Rats with Lesions of the Mammillary Bodies or Mammillothalamic Tract, *23*(8), 3506–3514.

Vann, S. D., & Aggleton, J. P. (2004). The mammillary bodies : two memory systems in one? *Nature Neuroscience Reviews*, *5*, 35–44.

Vann, S. D., & Aggleton, J. P. (2005). Selective dysgranular retrosplenial cortex lesions in rats disrupt allocentric performance of the radial-arm maze task. *Behavioral Neuroscience*, *119*(6), 1682–1686.

Vann, S. D., Aggleton, J. P., & Maguire, E. A. (2009). What does the retrosplenial cortex do ? What does the retrosplenial cortex do ? *Nature Reviews Neuroscience*, *10*(11), 792–802.

Vann, S. D., & Albasser, M. M. (2009). Hippocampal, retrosplenial, and prefrontal hypoactivity in a model of diencephalic amnesia: evidence towards an interdependent subcortical-cortical memory network. *Hippocampus*, *0*(September 2017), 1–13.

Vann, S. D., Brown, M. W., & Aggleton, J. P. (2000). Fos expression in the rostral thalamic nuclei and associated cortical regions in response to different spatial memory tests. *Neuroscience*, *101*(4), 983–991.

Vann, S. D., Brown, M. W., Erichsen, J. T., & Aggleton, J. P. (2000). Fos Imaging Reveals Differential Patterns of Hippocampal and Parahippocampal Subfield Activation in Rats in Response to Different Spatial Memory Tests. *The Journal of Neuroscience*, *20*(7), 2711–2718.

Vann, S. D., Brown, M. W., Erichsen, J. T., & Aggleton, J. P. (2000). Using fos imaging in the rat to reveal the anatomical extent of the disruptive effects of fornix lesions. *The Journal of Neuroscience*, *20*, 8144–8152.

Vann, S. D., Saunders, R. C., & Aggleton, J. P. (2017). Distinct, parallel pathways link the medial mammillary bodies to the anterior thalamus in macaque monkeys, (September).

Vann, S. D., Wilton, L. A. K., Muir, J. L., & Aggleton, J. P. (2003). Testing the importance of the caudal retrosplenial cortex for spatial memory in rats. *Behavioural Brain Research*, *140*, 107–118.

Vanzetta, I., & Grinvald, A. (1999). Increased cortical oxidative metabolism due to sensory stimulation: implications for functional brain imaging. *Science*, *286*, 1555–1558.

Vedder, L. C., Miller, A. M. P., Harrison, M. B., & Smith, D. M. (2016). Retrosplenial cortical neurons encode navigational cues, trajectories and reward locations during goal directed navigation. *Cerebral Cortex*, 1–11.

Velez-Fort, M., Rousseau, C. V, Niedworok, C. J., Wickersham, I. R., Rancz, E. A., Brown, A. P. Y., … Margrie, T. W. (2014). The stimulus selectivity and connectivity of layer six principal cells reveals cortical microcircuits underlying visual processing. *Neuron*, *83*, 1431–1443.

Vertes, R. P., Albo, Z., & Di Prisco, V. G. (2001). Theta-rhythmically firing neurons in the anterior thalamus: implications for mnemonic functions of Papez's circuit. *Neuroscience*, *104*(3), 619–625.

Vogt, B. A. (1985). Association and Auditory Cortices Vol. 4. In A. Peters & E. Jones (Eds.), *Cerebral Cortex* (pp. 89–149). New York: Plenum.

Vogt, B. A., & Miller, M. W. (1983). Cortical connections between rat cingulate cortex and vsual, motor, and postsubicular cortices. *The Journal of Comparative Neurology*, *210*, 192–210.

Vogt, B. A., Nimchinsky, E. A., Vogt, L. J., & Hof, P. R. (1995). Human Cingulate Cortex : Surface Features , Flat Maps , and Cytoarchitecture, *506*, 490–506.

Vogt, B. A., & Paxinos, G. (2014). Cytoarchitecture of mouse and rat cingulate cortex with human homologies. *Brain Structure and Function*, *219*(1909), 185–192.

Vuilleumier, P., Armony, J. L., Driver, J., & Dolan, R. J. (2003). Distinct spatial frequency sensitivities for processing faces and emotional expressions. *Nature Neuroscience*, *6*(6), 624–631.

Wang, D., Li, Y., Fu, J., & Wang, H. (2016). Diffusion kurtosis imaging study on temporal lobe after nasopharyngeal carcinoma radiotherapy. *Brain Research*, *1648*, 387–393.

Wang, K., Liang, M., Wang, L., Tian, L., Zhang, X., Li, K., & Jiang, T. (2007). Altered functional connectivity in early Alzheimer's Disease : A resting-state fMRI study. *Human Brain Mapping*, *978*(June 2006), 967–978.

Wang, L., Zang, Y., He, Y., Liang, M., Zhang, X., Tian, L., … Li, K. (2006). Changes in hippocampal connectivity in the early stages of Alzheimer's disease : Evidence from resting state fMRI. *NeuroImage*, *31*, 496–504.

Wang, Q., & Burkhalter, A. (2007). Area map of mouse visual cortex. *The Journal of Comparative Neurology*, *357*(July 2006), 339–357. https://doi.org/10.1002/cne

Wang, Q., Gao, E., & Burkhalter, A. (2007). In vivo transcranial imaging of connections in mouse visual cortex. *Journal of Neuroscience Methods*, *159*, 268–276.

Wang, Q., Gao, E., & Burkhalter, A. (2011). Gateways of ventral and dorsal streams in mouse visual cortex. *The Journal of Neuroscience*, *31*(5), 1905–1918.

Wang, Q., Sporns, O., & Burkhalter, A. (2012). Network analysis of corticocortical connections reveals ventral and dorsal processing streams in mouse visual cortex. *The Journal of Neuroscience*, *32*(13), 4386–4399.

Watson, D. M., Andrews, T. J., & Hartley, T. (2017). A data driven approach to understanding the organization of high-level visual cortex. *Nature Scientific Reports*, *7*(January), 1–14.

Watson, D. M., Hymers, M., Hartley, T., & Andrews, T. J. (2016). Patterns of neural response in scene-selective regions of the human brain are affected by low-level manipulations of spatial frequency. *NeuroImage*, *124*, 107–

117.

Weng, S., Lee, J., Peltier, S. J., Carrasco, M., Risi, S., Lord, C., & Monk, C. S. (2009). Alterations of resting state functional connectivity in the default network in adolescents with autism spectrum disorders. *Brain Research*, *1313*(May), 202–214.

Wheeler, A. L., Teixeira, C. M., Wang, A. H., Xiong, X., Kovacevic, N., Lerch, J. P., … Frankland, P. W. (2013). Identification of a Functional Connectome for Long-Term Fear Memory in Mice. *PLOS Computational Biology*, *9*(1), 1–18.

Whishaw, I. Q., Maaswinkel, H., Gonzalez, C. L. R., & Kolb, B. (2001). Deficits in allothetic and idiothetic spatial behavior in rats with posterior cingulate cortex lesions. *Behavioural Brain Research*, *118*, 67–76.

Wik, G., Fischer, C. A. H., Brage, B., Kristianson, M., & Fredrikson, M. (2003). Retrosplenial cortical activation in the fibromyalgia syndrome. *NeuroReport*, *14*(4), 619–621.

Wilber, A. A., Clark, B. J., Demecha, A. J., Mesina, L., Vos, J. M., & Mcnaughton, B. L. (2015). Cortical connectivity maps reveal anatomically distinct areas in the parietal cortex of the rat. *Frontiers in Neural Circuits*, *8*(January), 1–15.

Winter, S. S., Wagner, S. J., Mcmillin, J. L., & Wallace, D. G. (2011). Mammillothalamic tract lesions disrupt dead reckoning in the rat, *33*(October 2010), 371–381.

Wolbers, T., & Buechel, C. (2005). Dissociable retrosplenial and hippocampal contributions to successful formation of survey representations. *The Journal of Neuroscience*, *25*(13), 3333–3340.

Wong-Riley, M. T. (1989). Cytochrome oxidase: an endogenous metabolic marker for neuronal activity. *Trends in Neurosciences*, *12*, 94–101.

Wyss, J. M., & van Groen, T. (1992). Connections between the retrosplenial cortex and the hippocampal formation in the rat : A review. *Hippocampus*, *2*(1), 1–11.

Xie, H., Liu, Y., Zhu, Y., Ding, X., Yang, Y., & Guan, J. (2014). In vivo imaging of immediate early gene expression reveals layer-specific memory traces in the mammalian brain, *111*(7).

Xu, W., Huang, X., Takagaki, K., & Jian-young, W. (2007). Compression and reflection of visually evoked cortical waves. *Neuron*, *55*(1), 119–129.

Yasoshima, Y., Sako, N., Senba, E., & Yamamoto, T. (2006). Acute suppression , but not chronic genetic deficiency , of c-fos gene expression impairs long-term memory in aversive taste learning. *PNAS*, *103*, 7106–7111.

Yin, C., Zhou, F., Wang, Y., Luo, W., Luo, Q., & Li, P. (2013). NeuroImage Simultaneous detection of hemodynamics , mitochondrial metabolism and light scattering changes during cortical spreading depression in rats based on multi-spectral optical imaging. *NeuroImage*, *76*, 70–80.

Yokoo, T., Knight, B. W., & Sirovich, L. (2001). An optimization approach to signal extraction from noisy multivariate data. *NeuroImage*, *14*, 1309–1326.

Yoneoka, Y., Takeda, N., Inoue, A., Ibuchi, Y., Kumagai, T., & Sugai, T. (2004). Acute Korsakoff Syndrome following mammillothalamic tract infarction. *American Journal of Neuroradiology*, *25*(July), 964–968.

Yoshii, T., Hosokawa, H., & Matsuo, N. (2016). Pharmacogenetic reactivation of the original engram evokes an extinguished fear memory. *Neuropharmacology*, *113*, 1–9.

Yoshimura, H., Sugai, T., Honjo, M., Segami, N., & Onoda, N. (2005). NMDA receptor-dependent oscillatory signal outputs from the retrosplenial cortex triggered by a non-NMDA receptor-dependent signal input from the visual cortex. *Brain Research*, *1045*, 12–21.

Yu, H., Chaplin, T. A., Davies, A. J., Verma, R., & Rosa, M. G. P. (2012). Specialized area in limbic cortex for fast analysis of peripheral vision. *Current Biology*, *22*, 1351–1357. https://doi.org/10.1016/j.cub.2012.05.029

Zepeda, A., Arias, C., & Sengpiel, F. (2004). Optical imaging of intrinsic signals : recent developments in the methodology and its applications. *Journal of Neuroscience Methods*, *136*, 1–21.

Zhang, N., Rane, P., Huang, W., Liang, Z., Kennedy, D., Frazier, J. A., & King, J. (2010). Mapping resting-state brain networks in conscious animals. *Journal of Neuroscience Methods Journal*, *189*, 186–196.

Zhou, Y., Liang, M., Tian, L., Wang, K., Hao, Y., & Liu, H. (2007). Functional disintegration in paranoid schizophrenia using resting-state fMRI. *Schizophrenia Research*, *97*, 194–205.

Zingg, B., Hintiryan, H., Gou, L., Song, M. Y., Bay, M., Bienkowski, M. S., … Dong, H. (2014). Neural networks of the mouse neocortex. *Cell*, *156*(5), 1096–1111.